Integrated MEMS Cavity Optomechanical Oscillators for Wireless and Optical Communications

Turker Beyazoglu

Electrical Engineering and Computer Sciences
University of California at Berkeley

August 12, 2016

Integrated MEMS Cavity Optomechanical Oscillators for Wireless and Optical Communications

by

Turker Beyazoglu

A dissertation submitted in partial satisfaction of the

requirements for the degree of

Doctor of Philosophy

in

Engineering - Electrical Engineering and Computer Sciences

in the

Graduate Division

of the

University of California, Berkeley

Committee in charge:

Professor Clark T.-C. Nguyen, Chair
Professor Ming C. Wu
Professor Liwei Lin

Summer 2016

The dissertation of Turker Beyazoglu, titled Integrated MEMS Cavity Optomechanical Oscillators for Wireless and Optical Communications, is approved:

Chair _____ Date _____

_____ Date _____

_____ Date _____

University of California, Berkeley

Integrated MEMS Cavity Optomechanical Oscillators for Wireless and Optical Communications

Abstract

Integrated MEMS Cavity Optomechanical Oscillators for Wireless and Optical Communications

by

Turker Beyazoglu

Doctor of Philosophy in Engineering - Electrical Engineering and Computer Sciences

University of California, Berkeley

Professor Clark T.-C. Nguyen, Chair

Recent advancements in micro-optical and micro-mechanical resonator technologies have allowed researchers to exploit coupling between the optical field and mechanical motion in an optical cavity to affect cooling or amplification of mechanical motion. Cooling the mechanical motion of microscale objects has been of high scientific interest, since it facilitates observation and exploration of certain quantum phenomena, e.g., the standard quantum limit of detection. On the other hand, amplification of the mechanical motion allows realization of microscale devices for practical applications, such as light driven low phase noise signal generation by radiation pressure driven Opto-Mechanical Oscillators (OMO's).

The ability to achieve self-sustained oscillation with no need for feedback electronics makes an OMO compelling for on-chip applications where directed light energy, e.g., from a laser, is available to fuel the oscillation, such as Chip Scale Atomic Clocks (CSAC's). Indeed, an OMO can substantially reduce power consumption of a CSAC by replacing its power-hungry conventional quartz-based microwave synthesizer but this requires that the OMO output is sufficiently stable, as gauged over short time spans by its phase noise.

Pursuant to identify phase noise mechanisms, this thesis presents a new phase noise model for OMO's by deriving an OMO oscillator model with intuitive engineering understanding of its operation consistent with the established OMO theory. Phase noise theory suggests that attaining high mechanical-Q (Q_m) is crucial to lower the phase noise while high enough optical-Q (Q_o) is required for reasonably low-power operation. This motivates a focus on achieving a high-Q_m OMO to have low phase noise while maintaining a high enough Q_o for low power operation–a challenge in previous OMO's that had to trade-off Q_m and Q_o mainly because they use a single material that sets both.

The work in this thesis demonstrates integrated MEMS-cavity optomechanical oscillators that combine the best properties of optical and MEMS resonators in single composite multi-material OMO structures to simultaneously optimize mechanical and optical Q's. The multi-material coplanar ring OMO structure using a high-Q_o silicon nitride optical ring and a high-Q_m polysilicon ring simultaneously achieves high $Q_m > 22,000$, which is more than 2× higher

than that of previous-best silicon nitride OMO, and high $Q_o > 280,000$ on par with single silicon nitride ring demonstrations. With its high Q_m, the coplanar ring OMO exhibits a best-to-date phase noise of -114 dBc/Hz at 1 kHz offset and -142 dBc/Hz at 1 MHz offset from its 52-MHz carrier–a 12 dB improvement from the previous best by an OMO constructed of silicon nitride alone. The doped polysilicon structure and electrodes additionally allow tuning of the OMO's oscillation frequency via voltage control and harmonic locking to an external source, enabling future deployment of the multi-material OMO as a locked oscillator in a target low-power CSAC application. A second integrated OMO structure, dubbed stacked-ring OMO, is also demonstrated using similar silicon nitride and polysilicon ring resonators but this time coupled in a vertical fashion, allowing easy integration with sidewall sacrificial layer defined gap MEMS process technology to achieve high electromechanical coupling in the composite OMO.

Enabled by the MEMS integration that allows electrically coupled intput-outputs, a new optical communications application based on an OMO is introduced. A super-regenerative optical receiver detecting on-off key (OOK) modulated light inputs has been demonstrated that harnesses the radiation-pressure gain of the electrically-sustained integrated OMO to render its oscillation amplitude as a function of the intensity of light coupled into the oscillator. Unlike previous electronic super-regenerative receivers, this rendition removes the need to periodically quench the oscillation signal, which then simplifies the receiver architecture and increases the attainable receive bit rate. A fully functional receiver with a compact ~ 90 μm OMO comprised only of silicon-compatible materials demonstrates successful recovery of a 2 kbps bit stream from an OOK modulated 1550 nm laser input. By removing the need for the expensive III-V compound semiconductor materials often used in conventional optical receivers, this OMO-based receiver offers a lower cost alternative for sensor network applications.

Dedicated to my dear wife Nihan

Contents

List of Figures

List of Tables

Acknowledgments

I am deeply thankful to have so many people in my life that deserve an acknowledgement for where I am today and what I accomplished in my journey of education. An acknowledgement page is unfortunately too short to mention all of them, but nevertheless I would like to thank each and every one of my family members, teachers, and friends who put their trust in me and have always encouraged me to follow my dreams.

First, I would like to start with awesome people I met in Berkeley. A very big thanks goes to my research advisor Professor Clark Nguyen who have always been with me during my PhD with his guidance and support. It is absolutely a privilege to work with a world-expert who is always inspiring with his discussions. His "nothing is impossible" attitude have helped me push my boundaries and gain self-confidence for the work I do. I am also grateful for the flexibility and freedom he has provided in my research. I would like to thank another world-expert, Professor Ming Wu, who has been the co-PI of the research project I have been working on. I have learned so much by working with his group and I was very lucky to work in his laboratory. He is also very kind and has always been patient with my requests. I would also like to thank Professor Liwei Lin and Professor Tsu-Jae King Liu for serving on my qualifying exam committee, their feedback, and reviewing my dissertation.

I had the privilege of working with great colleagues and friends at Berkeley, and I am indebted to them for their help, teamwork, and friendship in all these years. Postdoctoral scholar Tristan Rocheleau was always there when I was puzzled and he was a true mentor. I am thankful to all Nguyen research group members: Mehmet Akgul, Thura Lin Naing, Jalal Naghsh Nilchi, Ruonan Liu, Yang Lin, Wei-Chang Li, Alper Ozgurluk, Robert Schneider, Lingqi Wu, Henry Barrow, Brian Pepin, Zeying Ren, Divya Kashyap, Tommi Riekkinen, and Li-Wen Hung who endured all the difficulties of PhD with me. I am also grateful to Wu research group members who were rest of the project team and worked with me on various aspects of the work presented in this thesis. Alejandro Grine was instrumental in building optical measurement setups, Karen Grutter has been the optical cavity microprocessing expert, and Niels Quack has provided guidance and help whenever in need. Our collaboration has always been very fruitful and I have learned a lot from them.

I appreciate the help from the Marvell Nanofabrication Laboratory staff, especially Richelieu Hemphill, Jay Morford, Kim Chan, Jeffrey Clarkson, and Ryan Rivers who do their best to maintain a good lab and help users with their process needs.

Berkeley Sensor & Actuator Center (BSAC) has been our larger family in research, which I have been proud to be a member of. BSAC Industrial Advisory Board (IAB) meetings have allowed me put our research into perspective and motivated me to continue what I have been doing. I am thankful to Richard Lossing, Kim Ly, John Huggins, and rest of BSAC staff for all their efforts to keep the center as the best MEMS research center in the World. I would also like to thank BSAC directors who provided valuable feedback during IAB meetings, and many friends that are too many to name here.

Outside of the busy life in Cory Hall, I had many fascinating friends who deserve big thanks for their support. Friends from so many different backgrounds and disciplines helped

me grow in all directions, and made my time in Berkeley enjoyable. I thank my friends from Turkish Student Association, University Village, and International House just to name a few.

My journey to Berkeley wouldn't have started if it weren't for my family. They always stood by my decisions, showed their trust and encouragement whenever I needed. I cannot thank you enough for your constant, unconditional love and support.

Last but not least, my biggest thanks goes to my dear wife Nihan who bore with me through many difficulties in all these years, and kept me going through it all. I dedicate this thesis to you.

Chapter 1

Introduction and Overview

1.1 Harnessing Optical Energy for Micro-Mechanical Systems

Micro-mechanical devices offer countless functionalities in various applications partly because they can couple with many different energy sources through different actuation mechanisms, such as electrostatic, piezoelectric, thermal, gravitational, and magnetic forces. Recently, advances in micro-optical and micro-mechanical resonator technologies also allowed harnessing optical energy to excite mechanical vibration in these systems via radiation pressure of light [5].

Radiation pressure stems from the photon scattering from a reflective surface. Photons, just like any other particle, carry momentum. When a photon reflects from a surface, momentum conservation requires that some momentum is transferred to the reflecting body with an associated radiation pressure force. Of course the amount of force exerted by a single photon is very small. However, when light is confined in a high quality factor optical cavity, photons bounce off the cavity wall multiple times before escaping so the radiation pressure becomes considerably large. In a cavity optomechanical system, the mechanical resonator is embodied within the same optical cavity, i.e. the structure acts both as a mechanical and an optical resonator. The two are coupled through the dimensional changes in the structure. A moving cavity boundary modifies the optical path length, and consequently, the optical resonance frequency that then alters the cavity photon number and radiation pressure. This coupling yielded rich phenomena including optical bistability [6], transparency [7], squeezing [8], cooling the mechanical motion [9],[10], and parametric instability [5],[11], which is also known as phonon lasing or self-sustained oscillation. This thesis investigates the latter where the interplay between the radiation pressure and the moving cavity sustains regenerative mechanical oscillations in on-chip micro-resonators to allow synthesis of RF and microwaves by harnessing light power.

1.2   Motivation
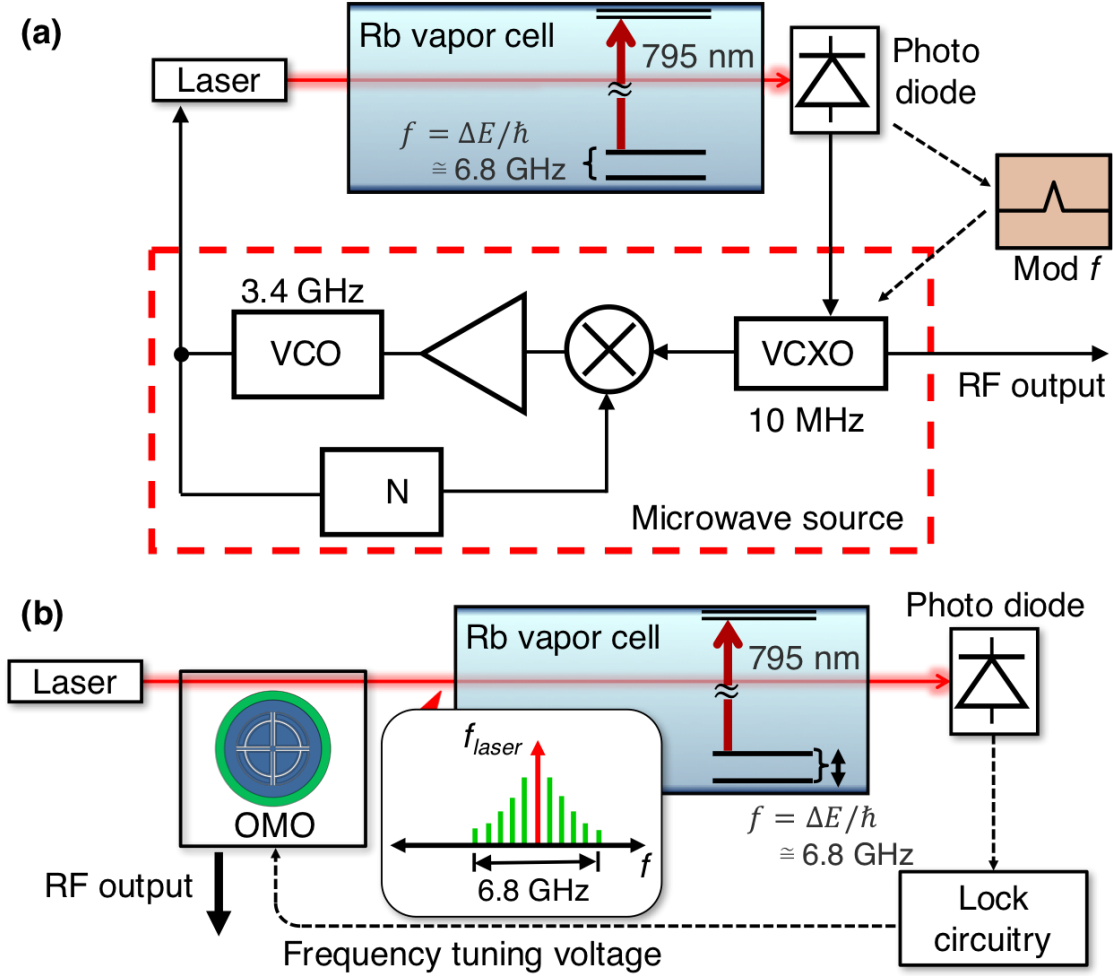
Figure 1.1: Targeted CSAC application. (a) Conventional CSAC: When the laser modulation generates two sidebands 6.834682610 GHz apart, the Rb vapor cell becomes transparent to 795 nm laser (a technique referred to as coherent population trapping (CPT), creating an error signal for correcting the frequency of the VCXO that then exhibits excellent stability. However, the PLL required for locking swamps the clock's power consumption. (b) Proposed low-power CSAC: OMO's higher-harmonics generate required sidebands for locking, obviating the need for a PLL while the fundamental frequency still provides the necessary clock output. Voltage controlled tunability of the OMO provides a simple feedback mechanism for locking where the tuning voltage emanates from locking circuitry.

Radiation Pressure-driven Opto-Mechanical Oscillators (RP-OMO's or OMO's in short) allow harnessing weak optical forces to supply energy for oscillatory mechanical motion in

a microscopic device, adding another energy source at the dispense of micro-mechanical oscillator designers. This is especially compelling for on-chip applications where a laser source is already present to fuel the oscillation. An example of such a system is a Chip Scale Atomic Clock (CSAC), where interrogating the atomic reference requires a laser.

Atomic clocks are world's one of the most stable frequency standards. Today's atomic clocks built by NIST [12] achieve frequency uncertainty of about 1×10^{-15}, meaning that they would not lose (or gain) a second in more than 100 million years. If such good timing instruments were portable, there would be enormous benefits for many applications, such as faster GPS systems, secure communications, networks with longer autonomy to name a few.

In 2002, DARPA initiated the CSAC program to build miniature versions of these clocks with much smaller power consumption (< 30 mW) to bring them into portable applications. Both the NIST atomic clocks and CSAC derive their stability from the transition between the hyperfine states of an alkali metal atom, which is a constant of nature, and thereby, much more stable than a mechanical reference like quartz whose frequency is subject to long-term changes in mechanical dimensions and stress. Figure 1.1(a) presents the schematic of a CSAC using Rubidium atoms for the frequency reference. Here, a cell containing Rb atoms in vapor state is interrogated by a 795 nm laser that corresponds to the wavelength for ^{87}Rb D1 transition, so the light is normally absorbed by the vapor cell. When the laser is modulated to generate sidebands apart by the 6.834682610 GHz hyperfine splitting frequency, it excites the atoms into a coherent dark state, where they become transparent to the interrogating laser light (no longer absorb it). A photodiode at the end of the vapor cell monitors the intensity of the laser light coming through the cell, which gets maximized when the modulation frequency matches the hyperfine splitting frequency. A feedback circuit then locks the quartz based microwave oscillator to the hyperfine splitting frequency by controlling the frequency of the microwave oscillator so that the photodetector output current is maximized at the hyperfine peak.

At the end of the CSAC program, there was tremendous progress towards the program goals and a miniaturized version [13] became available. However, of the program specs, the power consumption was not achieved particularly because the microwave synthesizer exceeds the power budget whereas the other atomic clock parts, such as the micro-oven needed to keep the Rb in vapor state, have successfully been implemented with low power. The microwave source consumes much power because it synthesizes the required ~3.4 GHz (half of the 6.834682610 GHz) signal from a 10 MHz voltage controlled crystal oscillator (VCXO) by using power hungry frequency division. Here, replacing the microwave source by a low power 3.4 GHz oscillator does not solve the problem since the actual clock output frequency near 10 MHz is desired, so some form of power-hungry frequency division would still be required.

An OMO could substantially reduce the CSAC power consumption by replacing its power-hungry microwave synthesizer. Figure 1.1(b) presents the targeted CSAC implementation using RP-OMO. Here, the RP-OMO modulates the pump laser at the mechanical resonance frequency, and via non-linear mechanical and optical interaction, at higher harmonics as well. This efficient built-in harmonic generation would allow exciting the hyperfine transition of

the Rb cell with an OMO harmonic at 3.4 GHz, while the OMO provides a much lower standard frequency clock output without the need for power-hungry frequency division.

Other than the above mentioned low-power CSAC target application, OMO's have also been proposed in other diverse applications such as microwave frequency generation [5], communications [14], and sensing [15]. To be useful in such applications, the output of an OMO must be sufficiently stable, as gauged over short time spans by its phase noise. Next section gives a brief review of the previous work with the emphasis on phase noise performance and required optical threshold power (P_{th}) to obtain oscillation. It is also important to note the values of the mechanical-Q (Q_m) and the optical-Q (Q_o) since they ultimately govern these performances to a great extent, as will be explained in more detail later.

1.3 Previous Work

Table 1.1: Summary of several RP-OMO devices and their performance.

Reference	Material	Q_m	Q_o	P_{th}	Phase noise at 1 kHz offset
[16]	Silica	2000	5.5×10^6	250 µW	-60 dBc/Hz
[4]	Silica (PSG)	7200	2.8×10^6	N/A	-87 dBc/Hz
[17]	SiN	2000	5.2×10^5	2 mW	-85 dBc/Hz
[4]	SiN	10400	74000	N/A	-102 dBc/Hz
[18]	Si	3300	3.5×10^5	3.56 µW	N/A
[19]	Si	6000	N/A	7.94 mW	-55.4 dBc/Hz
[20]	Si	376	42000	~100 µW	~-40 dBc/Hz

Early OMO demonstrations used silica microtoroid resonators [5],[16] with ultra-high Q_o's in the order of 10^7, which led to remarkably low ($\sim$20 µW) optical threshold power. Although they exhibit low P_{th}, the phase noise in such oscillators has typically been poor, with best-to-date published phase noise value from a phospho-silicate glass (PSG) microring resonator of -87 dBc/Hz at a 1 kHz offset from a 18.6 MHz carrier [4]. An important aspect to note regarding silica OMO fabrication is that the microtoroid resonators require one-by-one laser annealing and PSG devices require high temperature ($>1000\,^\circ$C) reflow to achieve such high Q_o's.

More recently, silicon nitride microring resonators have shown the potential of RP-OMO's to be immune to flicker noise [17] and achieved promising low phase noise marks [4] for communications applications. Among single material OMO's, the work of [4] was able to achieve the lowest phase noise of -102 dBc/Hz at 1 kHz from its 74 MHz carrier by enhancing its Q_m over 10,400–a result of recognizing that mechanical Q_m has the strongest impact on phase noise, much more than the optical Q_o. Indeed, the silicon nitride OMO has posted a much lower Q_o of 74,000 (consequently, much higher P_{th}) than its silica counterparts.

Silicon OMO's also offer some promise especially in low power and high frequency applications. A microdisk OMO has achieved oscillation frequency beyond GHz with a low threshold at a dropped power below 4 μW [18]. However, the phase noise performance of this OMO is not reported so a measure of its frequency stability may be inferred from its Q_m=3,300. Although it is not driven by radiation pressure, an electrostatically actuated opto-acoustic oscillator comprised of silicon microring resonators in positive feedback with external electronic amplifiers has posted -80 dBc/Hz phase noise at 10 kHz offset from a 2.05 GHz carrier [21]. More recently, same resonator structure also realized a true RP-OMO [19] but with a rather high phase noise value of -55.4 dBc/Hz at 1 kHz from its 175.3 MHz carrier despite operating at 80 °K to attain Q_m=6,000. Other than the Whispering Gallery Mode (WGM) devices, slot-type photonic crystal optomechanical cavities constructed in silicon have also shown parametric oscillations [20]. These devices offer high optomechanical coupling since the coupling is exponentially proportional to slot gaps between the beams which can be set to be on the order of wavelength of light (albeit, this needs electron beam lithography) whereas the optomechanical coupling scales with the radius of the cavity for WGM devices. Large optomechanical coupling provides an advantage to achieve low P_{th} and the work of [20] demonstrated an RP-OMO with Pth slightly above 100 μW. The measured Q_m=376 is however very low and the posted phase noise is in the order of -40 dBc/Hz at a 1 kHz offset from a 65 MHz carrier.

Table 1.1 summarizes notable examples of the previous OMO's. Note that there are many more optomechanical resonators using similar structures but they operate in the subthreshold regime (i.e. without oscillating) so they have not reported phase noise performance or threshold power.

1.4 Thesis Organization

The thesis begins with a review of optical and electro-mechanical microresonators in Chapter 2, which have been enablers of the OMO technology as well as many applications in optical and wireless communications. Chapter 2 explains the basic operation of Whispering Gallery Mode optical resonators and capacitively-transduced MEMS resonators, which are the building blocks of the OMO devices introduced later in Chapters 4 and 5.

Chapter 3 introduces the OMO technology and operation principles from an established theory perspective first, and continues with a more intuitive model presented for the first time in this thesis. The OMO model draws many parallels with engineer's understanding of oscillators and enables an intuitive understanding of the noise processes that contribute to the OMO phase noise. Finally, the chapter presents a new phase noise model based on the engineering OMO modeling, highlighting the roadmap for a low phase noise and low power OMO implementation.

In Chapter 4, the requirements for a high performance (low phase noise, low power) OMO derived in Chapter 3 are pursued using an integrated MEMS-OMO approach. With careful mechanical circuit design, composite multi-material devices combine the best prop-

erties of optical and MEMS resonators in a single OMO body, simultaneously optimizing mechanical and optical Q's. The chapter explains the design principles and operation of the multi-material OMO's, and presents experimental results that show best-to-date performance in its class. Furthermore, additional capabilities required for a CSAC implementation, such as voltage controlled frequency tuning and harmonic locking to an external source, are demonstrated with the composite structure.

Chapter 5 presents a new application enabled by the integrated OMO of Chapter 4, namely a super-regenerative optical receiver that receives and converts optical information into electrical signals. The receiver is a promising low-cost alternative for low bit rate communications, e.g. massive autonomous sensor networks, for which cost is paramount. Experimental results are presented with a fully functional receiver architecture, confirming successful operation of the OMO-based receiver.

Chapter 2

Micro Optical and Mechanical Resonators

This chapter introduces optical and mechanical micro-resonator technologies relevant to optomechanical oscillators, which have been fundamental building blocks of many optical and radio-frequency on-chip applications. Each of these technologies will be discussed separately in their own domain to explain fundamental operating and design principles, and a new class of technology named opto-mechanical resonator that essentially combines their functions in a single device will be introduced in the next chapter.

2.1 Micro-Optical Resonators

Optical resonators come in a variety forms such as Fabry-Perot resonators formed by two parallel mirrors, disk or ring-shaped dielectrics, multi-layer Distributed Bragg Reflectors (DBR's) and photonic crystals to name a few. In the microscale they have demonstrated great promise as fundamental building blocks in applications spanning from lasers, amplifiers, and sensors to optical channel dropping filters, add/drop multiplexers, and switches. Of these resonator geometries, disk/ring resonators particularly stand out with simple microfabrication process requirements. Unlike DBR's that use multiple layers of thin films or photonic crystals requiring precise dimensions with challenging lithography (often requiring E-beam lithography) steps, micro-disk/ring resonators only require a single layer film and single mask lithography with low-resolution that is easily achievable with a traditional stepper tool.

   This section introduces micro-disk and micro-ring based optical resonator technology that played the key role on emergence of optomechanical oscillators as well as developments in other timing applications in microwave and optical domains.

2.1.1   Micro-Optical Whispering Gallery Mode Ring Resonators ("Cavities")
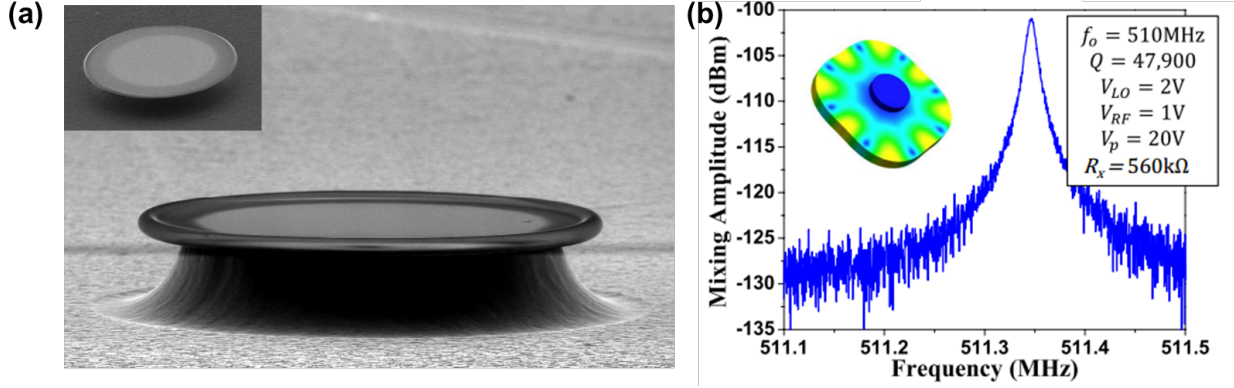
Figure 2.1: Whispering Gallery Mode (WGM) resonators in optical and acoustic domain. (a) SEM image of a WGM optical cavity from [1]. (b) Inset: FEA simulation of a WGM acoustic resonator presented in [2]. Measured spectrum reveals a remarkable Q_m of 47,900 at 510 MHz.

Microresonators with disk or ring geometry essentially channel light in a closed loop, and the loop in general can take form of another closed shape such as ellipse. Here, for brevity we use the term micro-ring but the concepts are valid for disk-shaped resonator geometry as well. Also, to avoid confusion with the mechanical resonator especially in the later chapters, we use the term "cavity" instead of resonator, although the latter term would be more appropriate.

Microring cavity is simply a curved waveguide closed onto itself to guide the wave in the cavity plane in a circular fashion by supporting both longitudinal and transverse modes. An interesting feature of the microring cavity is that it does not require an inner dielectric boundary to confine and guide the light–a critical feature exploited in the coplanar double-ring optomechanical oscillator design in Chapter 4.

Whispering Gallery Modes (WGM's) are such modes where the light is guided along the outer ring boundary in a repeated fashion without "seeing" the inner boundary. WGM's were first discovered in the acoustic domain by Lord Rayleigh as the word "whispering" suggests its relation to sound waves. The term has since been also used for other family of modes formed in optical and mechanical micro-resonators with electromagnetic and ultrasound waves. Figure 2.1 shows examples of both, where (a) is an optical WGM resonator from [1], and (b) depicts the mode shape of mechanical WGM disk demonstrated in [2] with a remarkable Q_m of 47,900 at 510 MHz.

As illustrated with the guided field profile in Figure 2.2, WGM's consist of azimuthally propagating fields confined to the inside surface of a dielectric boundary which guides the wave with repeated Total Internal Reflection (TIR). This cylindrical coordinate geometry
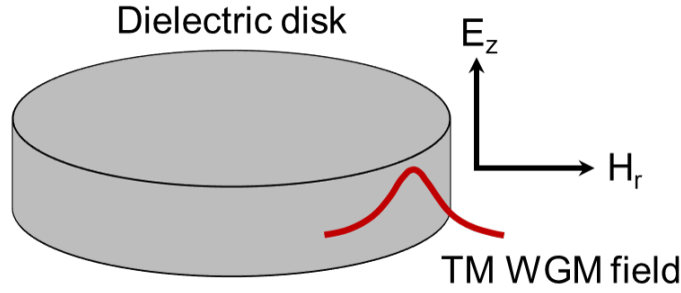
Figure 2.2: WGM Transverse Magnetic (TM) optical mode profile in a dielectric disk cavity. The mode propagates in the azimuthal direction by total internal reflection. In the TM mode, the dominant z-field is E_z while the transverse fields are H_r and H_ϕ.

of Figure 2.2 will facilitate the analytical description of WGM's by solving the Helmholtz equation in the next section.

Transverse Magnetic (TM) and Transverse Electric (TE) Mode Solutions of WGM's

WGM solutions of the Helmholtz equation approximately fall into two category: Transverse Magnetic (TM) and Transverse Electric (TE), which are dominated by E_z (z-directed electric field) and H_z (z-directed magnetic field), respectively. Note that this nomenclature follows the conventions of waveguides where the wave propagation is in the z direction, as it would be the case for an infinitely long cylinder. The analyses for TM and TE are identical, except with a change in the transverse and longitudinal fields. For this reason, the analysis will only derive the field expressions for TM mode and add TE mode solutions at the end.

For the TM mode, the Helmholtz equation

$$(\nabla^2 + k^2)E_z = 0 \tag{2.1}$$

can be written in cylindrical coordinates as

$$\left(\frac{\partial^2}{\partial r^2} + \frac{1}{r}\frac{\partial}{\partial r} + \frac{1}{r}\frac{\partial^2}{\partial \phi^2} + k^2\right)E_z(r,\phi) = 0 \tag{2.2}$$

Equation (2.2) can be solved by separation of variables such that $E_z(r,\phi) = E_z(r)E_z(\phi)$. This yields two equations for the azimuthal and radial components

$$\left(\frac{\partial^2}{\partial \phi^2} + m^2\right)E_z(\phi) = 0 \tag{2.3}$$

and

$$\left(\frac{\partial^2}{\partial r^2} + \frac{1}{r}\frac{\partial}{\partial r} + k^2 - \frac{m^2}{r^2}\right)E_z(r) = 0 \tag{2.4}$$

respectively. Here, m is the azimuthal mode number indicating the number of cycles the field undergoes when orbiting the ring. Solutions of Equation (2.3) are

$$E_z(\phi) = e^{\pm im\phi} \tag{2.5}$$

And solutions of Equation (2.4) have the form

$$E_z(r) = \begin{cases} J_m(k_o n_{eff} r) & r \le R_o \\ H_m^{(2)}(k_o r) & r > R_o \end{cases} \tag{2.6}$$

where the parameter R_o is the outer radius of the ring, k_o is the wavenumber in free space, n_{eff} is the effective refractive index, J_m is the Bessel function of the first kind, and $H_m^{(2)}$ is the Henkel function of the second kind. Combining Equations (2.5) and (2.6) yields

$$E_z(r) = \begin{cases} A_z J_m(k_o n_{eff} r) e^{\pm im\phi} & r \le R_o \\ B_z H_m^{(2)}(k_o r) e^{\pm im\phi} & r > R_o \end{cases} \tag{2.7}$$

where A_z and B_z are the field amplitudes that dependent on the excitation. The rest of the electric and magnetic fields can be derived easily from E_z using

$$H(r) = \frac{-i}{\mu_o \omega} \frac{1}{r} \frac{\partial E_z}{\partial \phi} \tag{2.8a}$$

$$H(\phi) = \frac{i}{\mu_o \omega} \frac{\partial E_z}{\partial r} \tag{2.8b}$$

$$H(z) = E_r = E_\phi = 0 \tag{2.8c}$$

In the most general case, there are three mode numbers (k, l, m) associated with each mode for each coordinate. In the case of a micro-ring resonator, thin dielectric film with a thickness of less than the resonant wavelength supports only one mode in the z direction so $l = 1$ is always assumed. In this case, the resonant wavelength λ_{km} has two mode numbers that depends on n_{eff} associated with each mode. λ_{km} and n_{eff} can be found by invoking the boundary condition at the dielectric-air interface $(r=R_o)$ that forces tangential magnetic field to be continuous, yielding

$$\frac{H_m^{(2)\prime}\left(\frac{2\pi R_o}{\lambda_{km}}\right)}{H_m^{(2)}\left(\frac{2\pi R_o}{\lambda_{km}}\right)} = n_{eff} \frac{J_m'\left(\frac{2\pi R_o n_{eff}}{\lambda_{km}}\right)}{J_m\left(\frac{2\pi R_o n_{eff}}{\lambda_{km}}\right)} \tag{2.9}$$

Equation (2.9) can be solved numerically for a λ_{km}-n_{eff} pair with an iterative approach. However, the higher-order radial modes $(k > 1)$ are usually not to our interest since the most confined radial mode is the fundamental mode $(k = 1)$. For the fundamental radial mode, the resonant condition is simply the periodic boundary condition in the azimuthal direction derived from Equation (2.5)

$$e^{i n_{eff} k_o 2\pi R_o} = 1 \tag{2.10}$$

which yields

$$k_o = \frac{m}{n_{eff} R_o} \tag{2.11}$$

or in terms of the wavelength

$$\lambda_o = \frac{2\pi R_o n_{eff}}{m} \tag{2.12}$$

which emphasizes that an integer number of effective wavelengths fit around the ring circumference.

The solutions of the TE modes simply have the same form as Equations (2.7) and (2.8) with the $E_z \rightarrow H_z$ substitution, yielding

$$H_z(r) = \begin{cases} C_z J_m(k_o n_{eff} r) e^{\pm im\phi} & r \leq R_o \\ D_z H_m^{(2)}(k_o r) e^{\pm im\phi} & r > R_o \end{cases} \tag{2.13}$$

and

$$E(r) = \frac{i\mu_o \omega}{k_o^2 n^2} \frac{1}{r} \frac{\partial H_z}{\partial \phi} \tag{2.14a}$$

$$E(\phi) = \frac{-i\mu_o \omega}{k_o^2 n^2} \frac{\partial H_z}{\partial r} \tag{2.14b}$$

$$E(z) = H_r = H_\phi = 0 \tag{2.14c}$$

for the complete set of fields of TE modes.

2.1.2 Optical Quality Factor

In an ideal optical cavity, light stored in the resonant mode would stay there forever. In reality, of course, light has a finite lifetime in the cavity and would eventually be lost due to various loss mechanisms. Cavity photon lifetime, τ, is inversely proportional to the resonant frequency, so the ability of an optical cavity to store its light field should rather be quantified with a dimensionless parameter that takes the resonant frequency also into account. Quality factor, abbreviated as Q, is a widely used such parameter that can be defined in terms of the cavity photon lifetime as

$$Q = \omega_o \tau = \frac{\omega_o}{\kappa} \tag{2.15}$$

The term κ in the second relation in Equation (2.15) is the cavity photon decay rate and is equal to the Full-Width Half-Maximum (FWHM) of the cavity resonance spectrum. By expressing the decay rate of the cavity stored energy U in terms of the photon decay rate, it is also possible to define the Q in terms of the stored energy

$$Q = 2\pi \frac{E_{stored}}{E_{loss/cycle}} \tag{2.16}$$

Various loss mechanisms such as absorption, scattering, and radiation contribute to the total photon decay rate in the cavity, adding together to shorten the photon lifetime

$$\kappa = \kappa_{abs} + \kappa_{scat} + \kappa_{rad} \tag{2.17}$$

In addition to the these intrinsic losses, external waveguide coupling also introduces an additional loss, which will be denoted as κ_{ex}. The total loss including the external one is then

$$\kappa = \kappa_{abs} + \kappa_{scat} + \kappa_{rad} + \kappa_{ex} = \kappa_i + \kappa_{ex} \tag{2.18}$$

where κ_i denotes the total intrinsic loss in the cavity.

The optical Q is maximized in WGM cavities by using low optical loss materials such as silicon dioxide, Phosphosilicate Glass (PSG), silicon nitride and single crystal silicon as demonstrated in Chapter 1, as well as minimizing the scattering and radiation losses by appropriately sizing the cavity and achieving smooth side-walls on the outer cavity wall.

2.1.3 Evanescent Optical Coupling
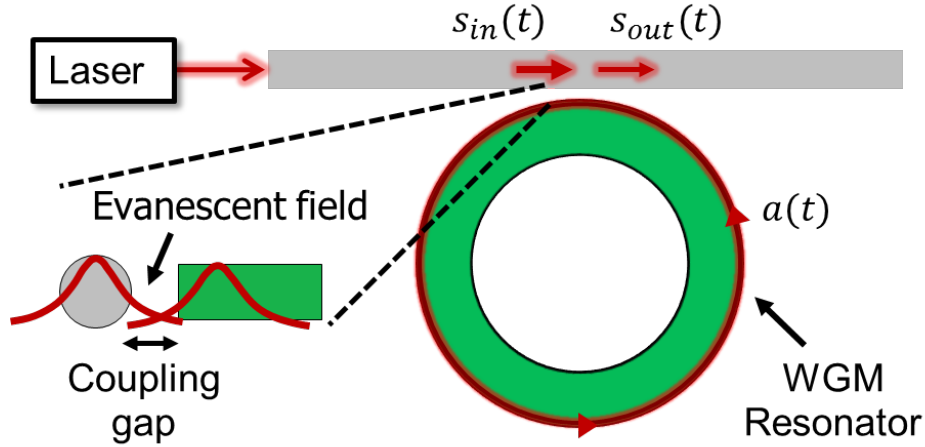
Figure 2.3: The optical field is coupled in and out of the WGM resonator by its evanescent portion that resides beyond the physical waveguide or resonator boundary. Waveguide and resonator dimensions are similar for enough overlap of the evanescent field as shown in the zoom-in panel. The field variables $a(t)$, $s_{in}(t)$, and $s_{out}(t)$ are the amplitudes of the cavity field, input field at the coupling junction, and the total field at the output of the cavity, respectively.

Equation (2.7) describes two distinct field components of the WGM where the optical field inside the ring edge is a guided wave and just outside from it is an evanescent wave. Using the E and H fields of the evanescent portion it can be shown that the evanescent

wave does not carry any power. However, they can be launched into propagating modes by introducing a second interface when evanescent field regions of both geometries intersect. The reverse is also true, where a waveguide with an evanescent optical field overlapping the cavity can couple the light in the waveguide to the cavity. The amount of coupling between the resonator and the waveguide can be controlled by the coupling gap and the waveguide dimensions.

With reference to Figure 2.3, an input optical field from a waveguide and the field built up in the resonator obey [22]

$$\dot{a}(t) = \left(-i\Delta - \frac{\kappa}{2}\right) a(t) + s_{in}(t)\sqrt{\kappa_{ex}} \tag{2.19a}$$

$$s_{out}(t) = s_{in}(t) - a(t)\sqrt{\kappa_{ex}} \tag{2.19b}$$

$$\Delta = \omega_{laser} - \omega_o \tag{2.19c}$$

where $a(t)$ is the complex mode amplitude with temporal variations other than the $e^{-i\omega_o t}$ dependence, Δ is the detuning of the field in the waveguide (i.e. laser field) from the cavity resonance frequency, $s_{in}(t)$ and $s_{out}(t)$ are the complex amplitude of the input and output field at the coupling junction, respectively.

In Equation (2.19), the amount of coupling between the cavity and waveguide is governed by the external coupling loss parameter κ_{ex}. As one can expect, larger coupling takes more energy out of the cavity into the waveguide. The amount of coupling depends on the overlap between the cavity and waveguide fields (which is a function of distance between the two), waveguide dimensions that yield larger evanescent field when sufficiently small, and phase matching between the two fields that requires $n_{eff/cavity} \approx n_{eff/waveguide}$.

2.1.4 Cavity Transmission

The transmission spectrum s_{out}/s_{in} of the cavity can be derived from the steady state solutions of Equation (2.19) for an external drive $s_{in} = s_{in}$ constant in time. After the transients die, the field amplitudes read

$$a = s_{in}\frac{\sqrt{\kappa_{ex}}}{-i\Delta + \kappa/2} \tag{2.20a}$$

$$s_{out} = s_{in} - a\sqrt{\kappa_{ex}} = s_{in}\left(1 - \frac{\kappa_{ex}}{i\Delta + \kappa/2}\right) \tag{2.20b}$$

The actual measured spectrum in experiments is usually the ratio of the output power to the input power swept across a certain frequency range. Using the results of Equation (2.20), power transmission of the cavity is equal to

$$\frac{P_{out}}{P_{in}} = \frac{s_{out}^2}{s_{in}^2} = \frac{\Delta^2 + (\kappa/2 - \kappa_{ex})^2}{\Delta^2 + (\kappa/2)^2} \tag{2.21}$$
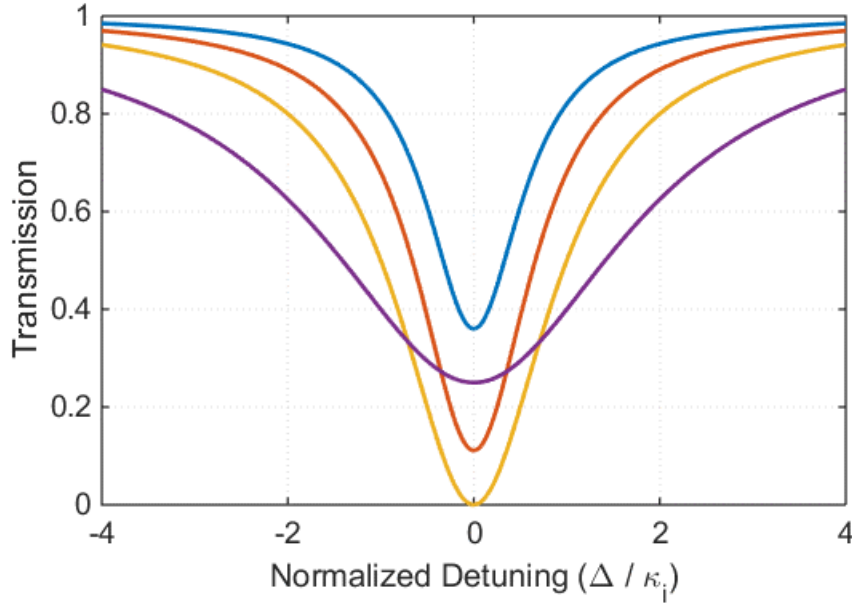
Figure 2.4: Cavity transmission spectrum as described by Equation (2.21) with respect detuning normalized to intrinsic loss rate κ_i. Curves represent the spectrum with varying κ_{ex}, which is a parameter that can be controlled experimentally. For $\kappa_{ex} < \kappa_i$ (blue, red), the transmission drops by increasing the κ_{ex}. When κ_{ex} reaches κ_i, the condition known as critical coupling, transmission (yellow) at the resonance frequency ($\Delta = 0$) drops to zero. Increasing κ_{ex} beyond κ_i results in broadened spectrum.

which is a Lorentzian that shows a minima at $\Delta = 0$ (i.e. at resonance) with a magnitude being a function of κ_{ex}. Figure 2.4 sketches the transmission spectrum for different values of κ_{ex}. The minimum transmission (at $\Delta = 0$) can theoretically be as low as 0 (-∞ dB) with the condition $\kappa_{ex} = \kappa_i = \kappa/2$, known as critical coupling. In practice, transmission in the order of -20 dB is achievable but it never reaches zero due to noise and non-ideal matching conditions.

Lastly, the linear model above does not consider any power dependency in the transmission spectrum. With a high drive power, thermal nonlinearity creates a transmission spectrum that is not anymore a Lorentzian function. Figure 2.5 demonstrates this effect with measured spectrum of a silicon nitride ring resonator under low (a) and high (b) input power. Here, the low power excitation yields a Lorentzian dip as expected. In the high power case the change in the cavity temperature due to absorption shifts the resonance to higher wavelengths during the laser frequency sweep, yielding a spectrum with a shark-fin shape.
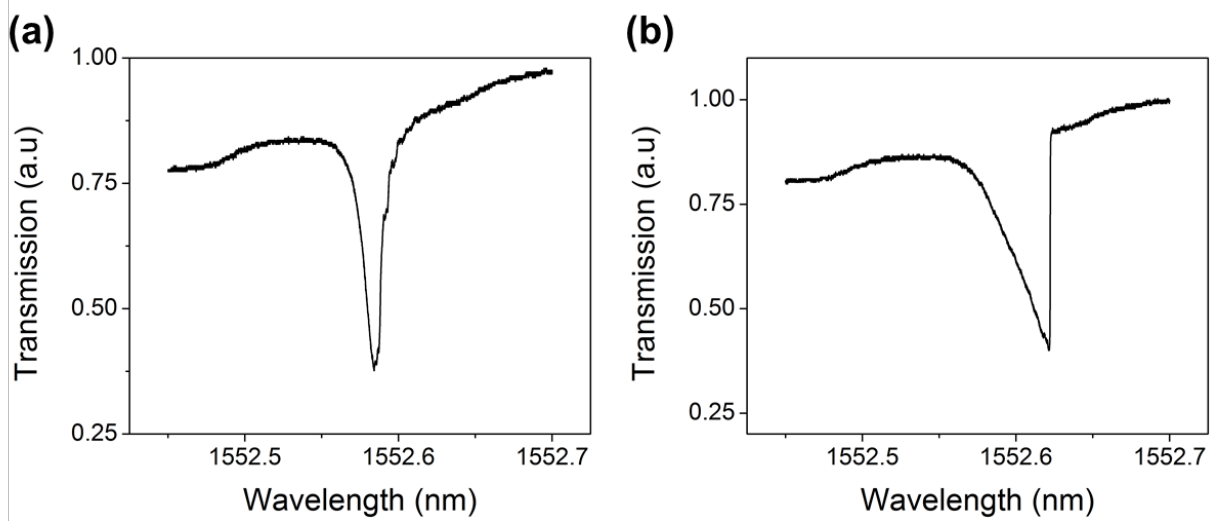
Figure 2.5: Measured transmission spectra of a silicon nitride WGM ring cavity with (a) small power, and (b) high power scans. When the input power is high, thermal nonlinearity pushes the resonance wavelength to higher values with the laser scan, creating a more gradual decrease in transmission. Once the laser wavelength is detuned from the resonance, the cavity temperature and the resonance wavelength shift backwards, resulting in a sharp jump in the spectrum.

2.2   Micro-Mechanical Resonators

Frequency synthesis and filtering applications have long been utilizing mechanical frequency references such as quartz, ceramic, and Surface Acoustic Wave (SAW) resonators, especially in the portable/wireless space (e.g. cell phones). The choice of mechanical resonators is largely due to two reasons: size and Q. The latter is important to achieve low insertion loss and sharp roll-off filters in the RF front-ends, and low phase noise in oscillators as will be discussed in detail in Chapter 3. Q values achieved by these mechanical resonators are mostly in the order of 1,000 to 10,000 (or even higher for quartz), which is orders of magnitude better than L-C (inductor-capacitor) electrical resonators. On the other hand, mechanical resonators are much smaller compared to high-Q microwave resonators due to a fundamental reason: acoustic velocities are orders of magnitude lower than the speed of light, hence wavelength of an acoustic wave is much smaller than an electromagnetic wave for the same frequency. As a result, a microwave resonator needs to have much larger dimensions to provide the same resonance frequency condition compared to a mechanical resonator, which convert electrical signals into mechanical vibrations (for filtering with its high-Q) where the signal travels as an acoustic wave at the speed of sound.

MEMS resonator technology is the next node that can allow continued size reduction by realizing complex mechanical signal processing functions on a single chip as well as integra-

tion of mechanical resonators and integrated circuits on the chip or system/package level. On the filtering side, Bulk Acoustic Wave (BAW) resonators such as Film Bulk Acoustic Resonator (FBAR) and Solidly Mounted Resonator BAW (SMR-BAW) have already been the technology of choice in the cell phone market especially for the high frequency bands where the mature SAW resonator technology falls short on Q. In the oscillators market, MEMS has also started replacing quartz in some applications such as consumer electronics and digital computing. MEMS silicon resonators offer cost and size reduction with simple manufacturing as well as significantly superior stability against vibration and shock. It also holds the promise of integration with IC and can eventually penetrate more into higher-end application areas.

The following sections will explain basic operation and modeling of MEMS resonators including lumped mechanical model, electromechanical transduction and electromechanical equivalent circuit model for the general resonator class, and design of a ring resonator architecture in particular to set the stage for the discussion of ring resonator based optomechanical resonator design in Chapter 4.

2.2.1 Lumped Mechanical Modeling of MEMS Resonators
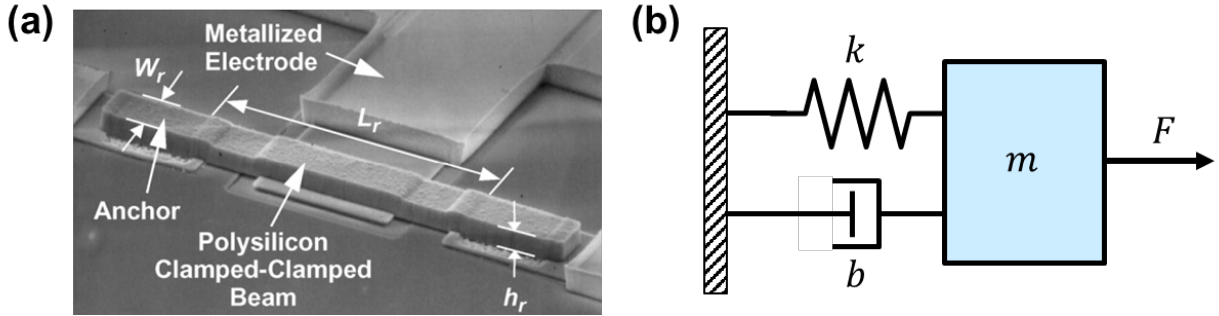
Figure 2.6: (a) A micromechanical clamped-clamped beam resonator that operates like a miniaturized version of a guitar string, vibrating at a single tone but with a much higher frequency (8.5 MHz) due to scaling of the size. (b) Lumped mechanical model of a resonator, where m is the mass, b is the damping, and k is the stiffness at a location where the force F is applied.

Mechanical vibration of a solid body is a manifestation of stress field generated in the structure, which is typically complex to deal with since it is a superposition of three dimensional traveling waves. However, each resonant vibrational mode of the structure has a unique displacement profile, named "mode shape", that allows modeling as a single degree of freedom mass-spring-damper system. For example, a guitar string vibrating at 440 Hz (the note A) or its miniaturized version depicted in Figure 2.6(a), a silicon micromechanical beam clamped at its both end to an underneath substrate vibrating at 8.5 MHz, can both

be modeled with a lumped equivalent mass, spring and damper at their resonant frequency, as in Figure 2.6(b).

Lumped parameter equivalent circuit modeling is based on the knowledge of stored energy (relative to an arbitrary excitation) and displacement profile of the resonator. For a given mode shape, which is usually known a priori from observed deformation of the structure and otherwise can be figured out via Finite Element Analysis (FEA) or using acoustic microscopy, determining the stored energy requires an integration over the geometry of the structure. Since the sum of the kinetic and potential energy is constant, and the kinetic energy is equal to zero at the maximum potential energy and vice versa, the maximum potential and kinetic energies are equal. Therefore, it is convenient to use the maximum kinetic energy for the calculation of total stored energy, which is found by summing up the kinetic energy of differential elements in the body

$$KE_{max} = \frac{1}{2} \iiint_V \rho \, V(r)^2 \, dx \, dy \, dz \tag{2.22}$$

where $r(x, y, z)$ is the position in the three dimensional space R^3, ρ is the material density, and $V(r)$ is the velocity of differential element at position r.

Since the velocity/displacement at a point on the structure depends on the external excitation, the mode shape is usually a normalized function with respect to the maximum displacement such that

$$\max U(r) = 1 \tag{2.23}$$

where $U(r)$ is the mode shape function describing the displacement amplitude at point r. This definition allows specification of the mode shape independent of the excitation amplitude.

Modal displacement has a sinusoidal time dependence whose frequency is equal to the resonance frequency of the mode. Velocity profile then simply follows from the displacement

$$U(r, t) = U(r) \sin(\omega_m t) \tag{2.24a}$$

$$V(r, t) = \dot{U}(r, t) = \omega_m U(r) \cos(\omega_m t) \tag{2.24b}$$

which indicates that velocity is simply equal to displacement times the (angular) resonance frequency, hence it is known at every point once the mode shape is known.

Effective Mass

Lumped element model of Figure 2.6(b) is a single degree of freedom system where the displacement is a unique single value unlike the actual resonator. This implies that the lumped element model is specific to location on the resonator, which has a specific displacement given by the mode shape. Locations on the resonator with different displacements have different lumped masses so that in all cases the kinetic energy is equal to the kinetic energy of the

actual resonator. The definition of this location-specific lumped mass, referred as effective mass, follows from the maximum kinetic energy

$$m_{eff} = \frac{2KE_{max}}{V(r_o)^2} = \frac{2 \times \frac{1}{2} \iiint_V \rho \; \omega_m^2 U(r)^2 \; dx \; dy \; dz}{\omega_m^2 U(r_o)^2} \tag{2.25}$$

where r_o is the location at which the effective mass is calculated. Arranging the terms yields

$$m_{eff} = \frac{1}{U(r_o)^2} \iiint_V \rho \; U(r)^2 \; dx \; dy \; dz \tag{2.26}$$

It is evident from Equation (2.26) that effective mass is minimum at the largest displacement location and it is larger at locations with smaller displacement. At the anchor location where the displacement is zero, effective mass is infinitely large so a finite force cannot generate any displacement, as expected.

Effective Stiffness

The equation of motion governing the mass-stiffness-damper system of Figure 2.6(b) is

$$F = m\ddot{x} + b\dot{x} + kx \tag{2.27}$$

For a periodic excitation[1] $F = Fe^{i\omega t}$, displacement of the resonator is

$$X(\omega) = \frac{F}{-\omega^2 m + k + i\omega b} \tag{2.28}$$

Equation (2.28) describes a Lorentzian response for the resonator where the displacement is maximized at the resonance frequency

$$\omega_m = \sqrt{\frac{k}{m}} \tag{2.29}$$

such that

$$X(\omega_m) = \frac{F}{i\omega_m b} \tag{2.30}$$

As evident from Equation (2.29), lumped mass and stiffness of the resonator are tied together through the resonance frequency. As such, once the resonance frequency and mode shape is known, effective mass follows from Equation (2.26) and stiffness follows from Equation (2.29)

$$k_{eff} = \omega_m^2 m_{eff} \tag{2.31}$$

---

[1]We will use the phasor notation $x \cos \omega t = X e^{i\omega t}$

Note that in some structures such as folded-beam resonators [23], it may be straight-forward to calculate the effective stiffness since only some simple parts (such as beams) contribute to the stiffness. In this case, the resonance frequency can be calculated directly from Equation (2.29).

Effective Damping

Modeling the damping of a resonator is not trivial since it requires calculating mechanical losses due to all loss mechanisms such as dissipation through the anchors to the substrate, thermo-elastic damping, air-damping, material losses, and phonon-phonon interactions. Although there are models of different loss mechanisms, attempts to predict total loss for a given resonator generally fall short on providing an absolute quantity, rather the models can be useful to figure out the dominant loss mechanism(s) in each resonator case. As such, total damping represented by parameter b in Figure 2.6(b) is not known a priori. In most cases, b is predicted from previous observations of similar resonators or extracted from the measurements after fabrication.

One of the easiest methods to quantify resonator losses (and accordingly parameter b) is to measure the quality factor from the resonance spectrum. The quality factor, also referred to as Q, relates the energy loss to the stored energy in the resonator such that the loss is quantified relatively rather than absolutely. The definition of Q from this fundamental perspective is

$$Q = 2\pi \frac{E_{stored}}{E_{loss/cycle}} = 2\pi \frac{E_{stored}}{P_{loss} \times T} = \omega_m \frac{E_{stored}}{P_{loss}} \tag{2.32}$$

where E_{stored} is the time-averaged stored energy in the resonator, $E_{loss/cycle}$ is the energy lost during one oscillation period, P_{loss} is the power loss, T is the period, and ω_m is the angular resonance frequency. This definition of Q can further be extended for a definition in terms of the equivalent lumped element values. Since the time-averaged stored energy is equal to the peak kinetic energy

$$E_{stored} = \frac{1}{2} m_{eff} v_{max}^2 \tag{2.33}$$

and power flow associated with a damper for a sinusoidal motion is

$$P_{loss} = \langle Fv \rangle = b_{eff}\langle v^2 \rangle = \frac{1}{2} b v_{max}^2 \tag{2.34}$$

the ratio of the two yields

$$Q = \omega_m \frac{m_{eff}}{b_{eff}} \tag{2.35}$$

A quick and easy way to measure Q of a resonator is to use a sweep frequency technique[2] to look at the resonator response. The response governed by Equation (2.28) is a Lorentzian with a 3-dB bandwidth of

$$\Delta\omega_{3dB} = \frac{b_{eff}}{m_{eff}} = \Gamma_m \tag{2.36}$$

where Γ_m is known as mechanical damping rate. Substituting the expression for b in Equation (1.13) yields

$$Q = \omega_m \frac{m_{eff}}{m_{eff}\Gamma_m} = \frac{\omega_m}{\Gamma_m} = \frac{f_m}{\Delta f_{3dB}} \tag{2.37}$$

Once the Q of the resonator is determined from the measured Lorentzian spectrum, the value of damping

$$b_{eff} = \frac{\omega_m m_{eff}}{Q} \tag{2.38}$$

and thus the lumped equivalent model is completely known.

2.2.2 Capacitive-Gap MEMS Resonator Equivalent Electromechanical Model
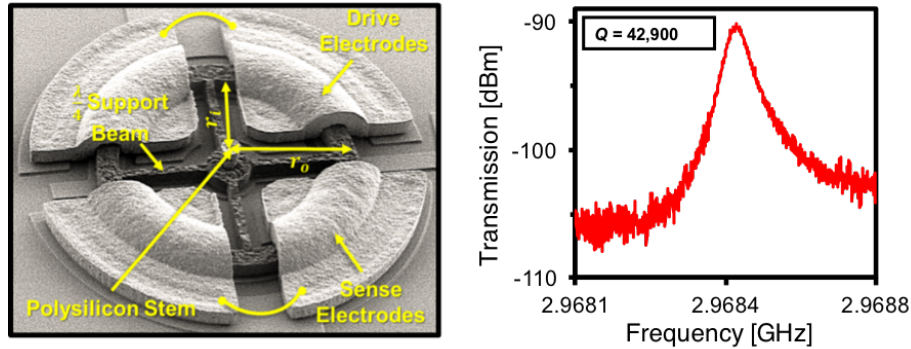
Figure 2.7: A high-Q_m MEMS resonator with a diamond ring structure presented in [3]. The measured Q_m of 42,900 is impressive at a high resonance frequency of 2.97 GHz.

MEMS resonators process electrical signals in mechanical domain with its high Q by first converting the input electrical signals into mechanical vibrations, and mechanical vibrations back into electrical signals at its output upon processing. The component facilitating

---

[2]There are several techniques of measuring Q of a MEMS resonator and the choice usually depends on the needed frequency resolution based on the Q value. For ultra high-Q's in the order of 10^6 or higher and especially low frequency resonances, ring-down measurement [1] can provide a quicker measurement.

this conversion between the mechanical and electrical domains is called transducer, which can be formed using different transduction mechanisms such as widely used piezoelectric and capacitive transduction in MEMS resonators. Piezoelectric transduction requires using piezoelectric films as the bulk resonator material and can achieve high electromechanical coupling coefficients of 6% or even more [24] compared to capacitive transduction with coupling lower by an order of magnitude, especially at high frequencies in the GHz range. However, Q values of piezoelectric MEMS resonators are typically lower than capacitively-transduced ones, in the range of 10^3 to 10^4 compared to 10^4 to 10^5 easily achieved by capacitive ones. Figure 2.7 shows an example capacitively-transduced ring resonator [3] with impressive Q_m of 42,900 at 2.97 GHz. This is a typical Q_m value also routienly achieved by polysilicon resonators, but usually at a lower resonance frequency. From the optomechanical oscillator point of view, Q is the key parameter for MEMS integration and we will limit our discussion to capacitive transduction as it is the technology used in the work presented in this thesis.

Capacitive-Gap Transducer Model
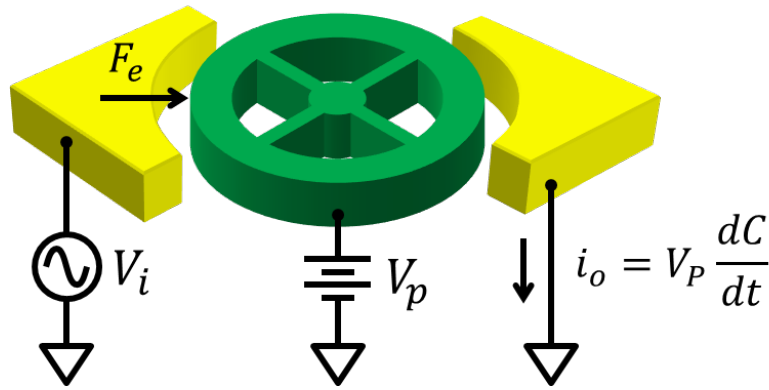
Figure 2.8: Schematic description of a capacitively-transduced MEMS ring resonator operation. The resonator structure (green) is held at a constant voltage V_P that charges the capacitance across the electrode-to-resonator gap. An input AC voltage with an amplitude V_i generates an electrostatic force F_e at the capacitor plates, which then pushes the resonator into vibration. The induced motion then modulates the charged output capacitance, creating an output electrical current on the second electrode.

Before diving into modeling of the transducer, it is useful to examine the physics of capacitive transduction mechanism. The force generated by the transducer is an electrostatic force that pulls the resonator towards the (stationary) electrode when there is a voltage difference between the electrode and the resonator. Note that this requires that both the electrode and resonator be electrically conductive to be at a defined (externally applied) voltage potential. Figure 2.8 illustrates this operation where the input electrode of a capacitively-transduced

ring resonator is tied to an AC voltage with amplitude v_i and the resonator itself is kept at a DC potential $V_P \gg v_i$. Two conductive structures with the airgap in between forms a movable capacitor, which stores an electrical energy equal to $\frac{1}{2}CV^2$. The electric field across the capacitor plates generates an electrostatic force that is equal to change in energy with respect to displacement

$$F_e = \frac{1}{2}\frac{\partial C}{\partial x}(V_P - v_i)^2 = \frac{1}{2}\frac{\partial C}{\partial x}\left(V_P^2 - 2V_P v_i + v_i^2\right) \tag{2.39}$$

For a resonant drive $v_i \cos \omega_m t$ Equation (2.39) expands into

$$F_e = \frac{1}{2}\frac{\partial C}{\partial x}\left(V_P^2 - 2V_P v_i \cos \omega_m t + \frac{v_i^2}{2}(1 + \cos 2\omega_m)\right) \tag{2.40}$$

where the first term is a DC component and the third term yields a very small DC and 2nd harmonic components. The DC force is usually balanced by an equal force generated at the output electrode. The relevant resonant electrostatic force that drives the resonator is then

$$F_e = -V_P \frac{\partial C}{\partial x} v_i \tag{2.41}$$

Note that the above derivation does not consider any frequency dependence in the partial derivative term $\frac{\partial C}{\partial x}$, which is a good approximation especially for small resonator displacements with respect to the electrode-to-resonator gap spacing. However, in reality the partial derivative term is non-linear for electrode configuration of Figure 2.8, and includes first and higher-order displacement terms, which generate additional resonant force components 90° phase shifted from the main driving force of Equation (2.41). We will exploit this feature of capacitive transduction for tuning the oscillation frequency of the optomechanical oscillators of Chapter 4 and omit its modeling here for brevity. The reader can refer to [25] for the discussion of complete modeling.

Table 2.1: Lumped element parameter conversions between electrical and mechanical domains using velocity and current as the flow variables.

Mechanical Domain		Electrical Domain	
Force	F	Voltage	v, V
Velocity	$\dot{x}$	Current	i, I
Displacement	x	Charge	q
Mass	m	Inductance	l, L
Stiffness	k	1/Capacitance	$1/c, 1/C$
Damping	b	Resistance	r, R

In the meantime, the resonator motion modulates the air-gap capacitance which results in a current flow from the AC voltage source to the capacitive transducer given by
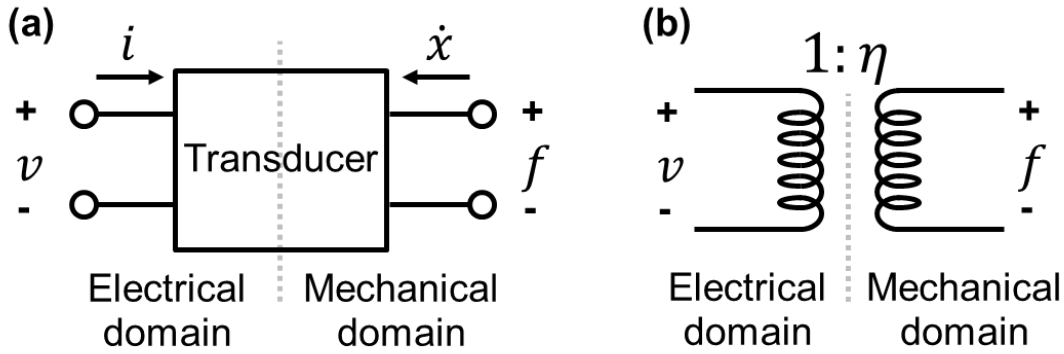
Figure 2.9: (a) A general transducer model that converts electrical domain variables v, i into mechanical domain variables f, and $\dot{x}$. (b) Transformer model for the capacitive-gap electromechanical transducer used in MEMS resonators.

$$i = V_P \frac{\partial C}{\partial t} = V_P \frac{\partial C}{\partial x} \frac{\partial x}{\partial t} \tag{2.42}$$

Figure 2.9(a) depicts a general electro-mechanical transducer where the effort and flow variables are voltage and current on the electrical side, and force and velocity on the mechanical side. In general, there is a one-to-one analogy between the electrical and mechanical domains since both systems are governed by analogous second-order differential equations

$$F = m\ddot{x} + b\dot{x} + kx \tag{2.43a}$$

$$V = l\frac{di}{dt} + ri + c\int i\,dt = l\ddot{q} + r\dot{q} + cq \tag{2.43b}$$

where q is the electrical charge. It is straightforward to see the analogy between the force and voltage as well as velocity and current directly from above equations and Table 2.1 presents a more complete picture with different parameters in both domains.

As the above analogy suggests, the transducer needs to transform voltage and current on one side to force and current on the other side, respectively. Equations (2.41) and (2.42) facilitate this relation

$$F_e = \eta v_i \tag{2.44a}$$

$$i = -\eta\dot{x} \tag{2.44b}$$

where the coupling coefficient η is defined as

$$\eta = \left| V_P \frac{\partial C}{\partial x} \right| \tag{2.45}$$

This linear relation between the effort and flow variables on each side of the transducer can most conveniently modeled by an electrical transformer with an equivalent turns ratio equal to the coupling coefficient as illustrated in Figure 2.9(b).

Complete Equivalent Electromechanical Model
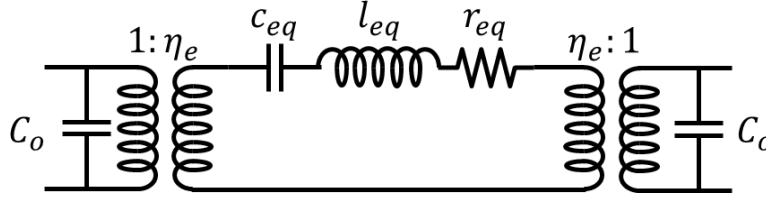
Figure 2.10: Complete equivalent electromechanical model of a capacitively-transduced MEMS resonator. r-l-c branch inside the transducers allow measuring mechanical variable values, where the voltage generated across the input transducer (on the r-l-c side) is equal to force and current flowing through the branch is equal to velocity.

Once the mechanical resonator and electromechanical transducers are modeled, it is straightforward to combine them in a complete electromechanical model that allows simulating the resonator behavior using circuit simulation tools such as SPICE. As presented in Table 2.1, the lumped mechanical model directly correspond to electrical circuit elements

$$m_{eff} = l_{eq} \tag{2.46a}$$

$$k_{eff} = \frac{1}{c_{eq}} \tag{2.46b}$$

$$b_eff = r_{eq} \tag{2.46c}$$

The mechanical resonator represented with a series l-r-c branch couples to electrical signals using a transformer for each electrode placement around the resonator. In the case of one input and one output electrode, two transformers with turns ratio

$$\eta_{in} = \left| V_P \frac{\partial C_{in}}{\partial x} \right|, \eta_{out} = \left| V_P \frac{\partial C_{out}}{\partial x} \right| \tag{2.47}$$

connect to the l-r-c branch as shown in Figure 2.10, where the input and output capacitances are assumed identical such that $\eta_{in} = \eta_{out} = \eta_e$. Additional capacitors C_o across the transformers model the electrical path formed by the overlap capacitance between an electrode and the resonator. This electrical path conducts AC current from an input voltage source to ground that is not generated by the motion of the device. If this current reaches the output via any parasitic path, it may compete with the desired motional current. This is an important consideration especially for MEMS filter and oscillator applications where

high ratio of the motional capacitance to C_o is desired. Circuit presented in Figure 2.10 is the basic complete equivalent model of a MEMS resonator. The model is powerful in that it allows using electrical circuit simulators to extract values of the mechanical variables (force and velocity) for a given electrical excitation as well as the resonator electrical response at the output.

2.3 Conclusion

Basic operation principles of optical and MEMS resonators summarized in this chapter are also fundamental to the operation and design of integrated OMO's presented in the following chapters. Especially, high-Q_o WGM optical cavity design considerations and mechanically coupled device modeling are instrumental and will be further investigated with the integrated OMO designs.

Chapter 3

OMO Operation and Modeling

3.1 Radiation Pressure

Pressure effects due to electromagnetic radiation is not a new idea. Kepler hypothesized in the 17th century that comet tails always point away from the sun because of the force exerted by the sunlight. Maxwell's theory has also predicted such effects due to electromagnetic radiation but experimental evidence did not become available until the 20th century. With the invention of lasers, it became possible to use optical forces to manipulate mechanical objects, such as freezing out the random motion of atoms and ions with a technique termed laser cooling.
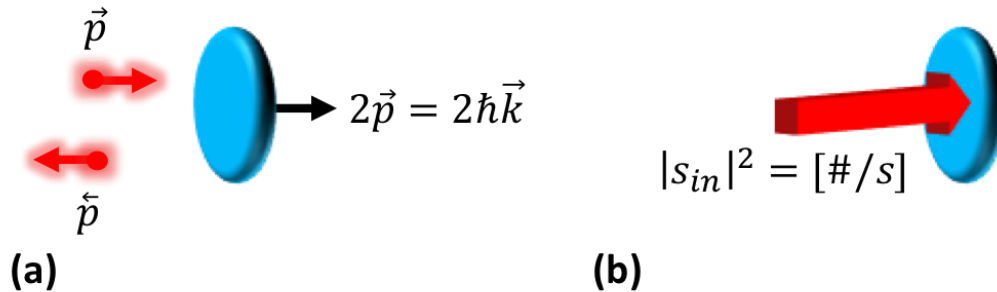
Figure 3.1: (a) Picture of momentum transfer onto a mirror upon reflection of a photon. Conservation of momentum dictates the sum of momentum vectors after the reflection must be equal to the momentum of the incoming photon. (b) A coherent light beam with "#" photons hitting the mirror per second has a normalized field amplitude s_{in} such that $|s_{in}|^2$ equals the photon arrival rate $\#/second$.

Theoretical framework for radiation pressure effects on massive mechanical resonators has been developed in the context of LIGO [26], where kilogram-scale suspended mirrors constitute kilometer-scale interferometers to detect tiny displacements induced by gravitational

waves. The theory has provided a comprehensive understanding of the optomechanical interactions in a suspended cavity, where the radiation pressure was predicted to change the dynamics of the mechanical system by effectively adding an optically induced stiffness and damping.

The physical origin of the radiation pressure is the momentum transfer resulting from reflection of a photon. DeBroglie's theorem states that a particle's momentum and wavelength are related by

$$\lambda = \frac{h}{p} \tag{3.1}$$

where λ is the wavelength, p is the momentum and h is the Planck's constant. According to this relation, even massless light waves carry a certain momentum and have particle nature. In terms of the wavenumber $k = 2\pi/\lambda$, the momentum of each photon is

$$p = \hbar k \tag{3.2}$$

where the reduced Planck's constant $\hbar = h/2\pi$ is used. With reference to Figure 3.1(b), radiation pressure force on a mirror being subject to a coherent light beam with a photon arrival rate $|s_{in}|^2$ is

$$F_{rp} = \frac{dp}{dt} = \frac{2\hbar k N_{ph}}{dt} = 2\hbar k |s_{in}|^2 \tag{3.3}$$

The factor of two is a natural result of momentum conservation that dictates the sum of the momentum vectors before and after the collision should be equal, as illustrated in Figure 3.1(a). Assuming the coherent light beam is from a laser with an output power P_{laser} and radial frequency ω_o, using the relation $P_{laser} = \hbar\omega_o N_{ph}$, radiation pressure force in terms of the laser power becomes

$$F_{rp} = \frac{2k}{\omega_o} P_{in} = \frac{2P_{in}}{c} \tag{3.4}$$

This is of course a very small force that makes it difficult to observe in daily life. Even with a large laser power of 1 W, the radiation pressure force is only 6.7 nN. However, the force becomes profound when photons are recycled, such as when traveling in an optical cavity.

3.2   Optomechanical Interactions in a Cavity

In an optical cavity, the number of round trips a photon makes before leaking out or being absorbed is approximately equal to the cavity Finesse, F. Therefore, in a high Finesse cavity the built-up optical power is much larger than the input optical power, so the radiation pressure is also amplified. In order to find an expression for the radiation pressure force exerted to a WGM ring by the circulating cavity field, it would be useful to look at the simplistic ray optics picture depicted in Figure 3.2. A photon confined in a cavity with n sidewalls makes n collisions at an angle of π/n in each round trip, with a corresponding
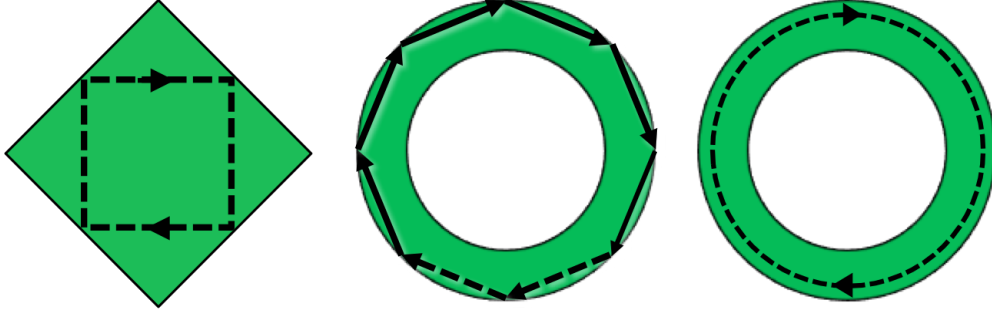
Figure 3.2: Simplified ray picture of light circulating in a cavity. A photon makes n collisions at an angle of π/n with cavity walls in each cycle where n is the number of sidewalls of the cavity. For a circular geometry, $n \to \infty$ and the collision becomes tangential.

radial momentum transfer of $2\hbar kn sin(\pi/n)$. In the limit $n \to \infty$ for a circular WGM cavity, the radial momentum transfer per photon per round trip becomes:

$$2\hbar k \lim_{n\to\infty} n sin(\pi/n) = 2\pi\hbar k \tag{3.5}$$

The associated radial force per photon is then found by dividing this momentum transfer by the cavity round trip time $\tau_{rt} = 2\pi R n_{eff}/c$

$$F_{rp/ph} = \frac{2\pi\hbar k}{\tau_{rt}} = \frac{\hbar k_o c}{R} = \frac{\hbar\omega_o}{R} \tag{3.6}$$

Total force acting on the cavity wall is then simply the product of single-photon induced force and the number of photons stored in the cavity.

$$F_{rp/ph} = \hbar\frac{\omega_o}{R}N_{ph} \tag{3.7}$$

3.3   Optomechanical Coupling

There are several mechanisms that can couple optical and mechanical degrees of freedom in a cavity, such as photothermal [27] and photoelastic [28] effects, but in the context of optomechanics the coupling mechanism is a moving cavity boundary that shifts the optical resonance with mechanical displacement.

An on-chip WGM cavity such as micro-disk, toroid, or ring is free to move once it is (partially) released from its substrate, just like the MEMS resonators of Chapter 2. In this case, the structure embodies two resonators, i.e., it acts as a mechanical as well as an optical resonator. The resonance condition $2\pi n_{eff}R = m\lambda$ for a WGM cavity indicates that the resonance wavelength (or frequency) depends on the cavity radius R. This indicates that any (small) cavity displacement that changes the radius would also change the cavity resonance

frequency. The optomechanical coupling strength gauges the frequency shift in the optical resonance upon a mechanical displacement x[1]

$$g_{om} = -\frac{d\omega_o}{dx} \tag{3.8}$$

assuming that the cavity displacement is described by the one-dimensional variable x that shifts the optical resonance frequency in a linear fashion. In this case, the optical resonance frequency with a moving cavity boundary is expressed as

$$\omega_o' = \omega_o + g_{om}x \tag{3.9}$$

where ω_o' and ω_o are the modified and unperturbed cavity resonance frequencies, respectively.

Since the displacement profile of the cavity radius depends on the mechanical resonance mode, g_{om} is not uniquely defined for a given structure. A general expression for g_{om} can be derived from the stored electromagnetic energy in the cavity. Total stored electromagnetic energy U is equal to

$$U = \hbar\omega_o N_{ph} \tag{3.10}$$

and the change in the stored energy upon displacement must be due to the change in the optical resonance frequency, so $\Delta U = \hbar\Delta\omega_o N_{ph}$. This allows using perturbation of the stored energy to calculate optical resonance shift due to arbitrary displacement $\vec{\mathcal{R}}(\vec{r})$ [29]

$$\frac{\Delta U}{U} = \frac{\Delta\omega_o}{\omega_o} = \frac{1}{2}\frac{\int |\vec{E}(\vec{r})|^2 \cdot (\epsilon(\vec{r}+\vec{u}(\vec{r})) - \epsilon(\vec{r}))d^3r}{\int |\vec{E}(\vec{r})|^2 \cdot \epsilon(\vec{r})d^3r} \tag{3.11}$$

where ϵ is the permittivity of the cavity material. When applied to the case of a moving dielectric boundary, this perturbation theory provides an expression for the frequency shift to an arbitrary mechanical deformation of the confining dielectric cavity [30]

$$g_{om} = -\frac{\omega_o}{2}\frac{\int (\vec{\mathcal{R}}\cdot\vec{n})(\Delta\epsilon|\vec{E}_\parallel|^2 - \Delta\epsilon^{-1}|\vec{D}_\perp|^2)dS}{\int(\vec{E}\cdot\vec{D})dV} \tag{3.12}$$

where displacement $\vec{\mathcal{R}}$ is normalized such that $\max|\vec{\mathcal{R}}| = 1$ and n is the outward facing normal vector, $\vec{E}$ is the electric field, $\vec{D}$ is the electric displacement field with subscripts $\parallel$ and $\perp$ indicating the field components parallel and perpendicular to the surface, respectively. $\Delta\epsilon = \epsilon_{cavity} - \epsilon_{air}$ is the difference between the refractive index of the cavity material and surrounding medium and $\Delta\epsilon^{-1}$ is defined as $\epsilon_{cavity}^{-1} - \epsilon_{air}^{-1}$. This comprehensive expression for the coupling can be used to determine the optomechanical coupling strength of different mechanical mode shapes of the structure. As an example, four different mechanical modes of a disk geometry investigated in [28] including first and second radial contour modes have

---

[1]It is also common to use vacuum optomechanical coupling rate that is normalized to the zero-point fluctuations $x_{zpf} = \sqrt{\frac{\hbar}{2m_{eff}\omega_m}}$ such that $g_o = g_{om}x_{zpf}$.

significantly different optomechanical coupling strengths, with the largest of -1080 GHz/nm for the first radial contour mode, being much stronger than the second contour mode, "pinching" mode and "bowl" mode with -82 GHz/nm, -412 GHz/nm, and -0.11 GHz/nm coupling strengths, respectively. Since the first radial contour mode has the largest coupling, it is the mode that oscillates when the laser power is large enough to sustain the oscillations. In fact, all oscillators presented in this thesis oscillate in the first radial contour mode (although in a bit distorted fashion due to the support beams) as well as almost all other reported WGM oscillator examples in the literature. Purely radial mechanical displacement with the maximum amplitude at the cavity periphery yields a simple expression for the g_{om}

$$g_{om} = -\frac{d\omega_o}{dx} = -\frac{d\omega_o}{dR}\frac{dR}{dx} = -\frac{d\omega_o}{dR} = -\frac{\omega_o}{R} \tag{3.13}$$

which will be used throughout this thesis.

3.4 Coupled Mode Theory

The previous section established the basis of how the mechanical vibrations couple to the optical resonator. Specifically, in terms of the parameters of Equation (2.19), displacement of the cavity modifying the optical resonance frequency changes the tuning according to

$$\Delta(x) = \Delta - g_{om}x(t) \tag{3.14}$$

Meanwhile, the radiation pressure force given by equation (3.7) can now be re-written in terms of the derived coupling constant $g_{om} = -\omega_o/R$. In addition, since the cavity photon number depends on the optical intensity built up in the cavity, it is convenient to normalize the field such that $|a|^2 = N_{ph}$ (with this normalization, it follows that $|s_{in}|^2$ is the input photon flux, i.e., the number of photons arriving in the fiber-cavity coupling region per second). Doing so yields

$$F_{rp} = -\hbar g_{om}|a|^2 \tag{3.15}$$

This radiation pressure force couples the optical field back to the mechanical resonator by acting on it as an external force.

Displacement dependent detuning and radiation pressure force in equations (3.14) and (3.15) modify Equations (2.19) and (2.27) such that

$$\dot{a} = \left[i(\Delta - g_{om}x) - \frac{\kappa}{2}\right]a + s_{in}\sqrt{\kappa_{ex}} \tag{3.16}$$

$$m_{eff}\ddot{x} + m_{eff}\Gamma_m\dot{x} + kx = -\hbar g_{om}|a|^2 \tag{3.17}$$

Since the radiation pressure force acts on the outer resonator boundary, the values of lumped elements m_{eff}, Γ_m and k are calculated at $r = R_o$ as explained in Chapter 2. Equations (3.16) and (3.17) are the coupled equations describing the optomechanical system [14]. This

coupling between the optical cavity and the mechanical resonator originates a rich set of phenomena including the self-sustained mechanical oscillations as will be explained in detailed in the following sections. We first start by looking at the static solutions of the coupled equations.

3.4.1 Static Solutions

The radiation pressure force acting on the resonator boundary will alter its position just like any other force acting on a spring-mass system. For a given cavity position $x = \bar{x}$ and constant drive amplitude s_{in}, after the transients vanish in the steady state, cavity field amplitude obeys

$$\bar{a} = \frac{s_{in}\sqrt{\kappa_{ex}}}{\frac{\kappa}{2} - i(\Delta - g_{om}\bar{x})}$$ (3.18)

The static force then follows as

$$\bar{F}_{rp} = -\hbar g_{om}\frac{4|s_{in}|^2\kappa_{ex}}{\kappa^2 + 4(\Delta - g_{om}\bar{x})^2}$$ (3.19)

where the terms with bar represent the static values.
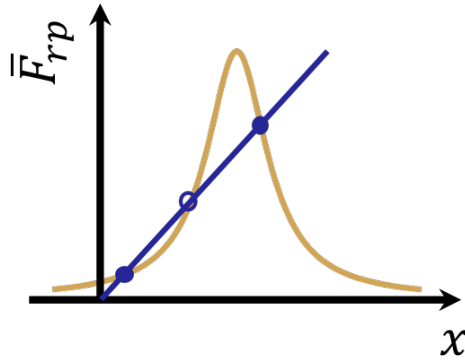
Figure 3.3: Graphical solutions of $\bar{F}_{rp} = k\bar{x}$ with three possible solutions. Solid dots are the stable solution points where the restoring force counteracts the change in the radiation pressure force with displacement. Hallow circle indicates the unstable solution.

On the other hand the balancing static force from the mechanical resonator is simply

$$\bar{F} = k\bar{x}$$ (3.20)

Solutions of $\bar{F}_{rp} = k\bar{x}$ yield the static displacement of the cavity, which can be obtained graphically as illustrated in Figure 3.3. There is always at least one solution, and in the case of red detuning $\Delta < 0$ there can be two additional ones depending on the resonator parameters (such as power, stiffness, cavity bandwidth etc.) such that there are two stable

solutions. This is known as optomechanical static bistability [6] where the two possible stable states correspond to, for example, high and low cavity power, resulting in hysteresis in the transmission behavior.

3.4.2 Dynamic Effects

The dynamical effects emanate from the retarded nature of the radiation pressure force. Due to the finite cavity storage time, photon number does not change instantaneously upon mechanical displacement, so the radiation pressure force lags the mechanical position with a finite time delay. We show this dependence explicitly in Equation 3.17

$$m_{eff}\ddot{x}(t) + m_{eff}\Gamma_m\dot{x}(t) + kx(t) = F_{rp}(x(t-\tau)) = -\hbar g_{om}|a(t)|^2 \qquad (3.21)$$

where $\tau \approx 1/\kappa$ is the cavity delay time. Now with this dynamic contribution we turn our attention from static solutions to time-varying oscillatory mechanical displacements. For $x = x_o \sin\omega_m t$, the equation for optical field amplitude (3.16) has an oscillatory term that would modulate it accordingly. To show this modulation explicitly, we can switch to a phasor domain that does not rotate at the laser frequency so that the input field is $s_{in}e^{-i\omega_L t}$ from a laser with $\omega = \omega_L$. The equation for optical field then reads

$$\dot{a}(t) = \left[i(\omega_o - g_{om}(x_o \sin\omega_m t)) - \frac{\kappa}{2}\right]a(t) + s_{in}e^{-i\omega_L t}\sqrt{\kappa_{ex}} \qquad (3.22)$$

which has the solution [31]

$$a(t) = s_{in}\sqrt{\kappa_{ex}} \sum_{n,m=-\infty}^{+\infty} \frac{i^{n-m}J_n(\beta)J_m(\beta)}{-i(\Delta + n\omega_m) + \kappa/2}e^{-i[\omega_L + (n-m)\omega_m]t} \qquad (3.23)$$

where $\beta \triangleq -g_{om}x_o/\omega_m$ is the modulation index. Equation (3.23) reveals that the mechanical displacement modulates the optical field, generating sidebands at $\omega_L \pm \omega_m$, and for large displacement amplitudes (or β) the sidebands extend even further in the frequency domain, occurring at the harmonic frequencies $n\omega_m$. This frequency comb generation is an important property of optomechanical oscillators and particularly useful for lowering the power consumption in the targeted CSAC application. Chapter 4 will present OMO harmonic generation and locking using a coplanar double-ring structure.

It is possible to solve the coupled equations (3.16) and (3.17) simultaneously to study the dynamics of the optomechanical system but this requires using a numerical solver to see the system behavior for every possible design and operating conditions. Alternatively, an analytical solution, which is possible with the small signal approximation, is valuable to understand how the dynamics modify the system, and how self-sustained oscillations start in the case of large positive feedback. For small values of x and a, equations (3.16) and (3.17)

can be linearized around static values

$$\bar{x} = \frac{-\hbar g_{om}|\bar{a}|^2}{k}$$

$$\bar{a} = \frac{s_{in}\sqrt{\kappa_{ex}}}{\frac{\kappa}{2} - i(\Delta - g_{om}\bar{x})}$$

(3.24)

such that

$$a(t) = \bar{a} + \delta a(t)$$

$$x(t) = \bar{x} + \delta x(t)$$

(3.25)

and $\delta a(t) << \bar{a}$ and $\delta x(t) << \bar{x}$. Here, the input field amplitude s_{in} is assumed to be constant so $\delta s_{in}(t) \approx 0$. Substituting (3.25) into (3.16) and (3.17) yields

$$\delta\dot{a}(t) = \left[i(\bar{\Delta} - g_{om}\delta x(t)) - \frac{\kappa}{2}\right](\bar{a} + \delta a(t)) + s_{in}\sqrt{\kappa_{ex}}$$

$$m_{eff}\left(\delta\ddot{x}(t) + \Gamma_m\delta\dot{x}(t) + \omega_m^2(\bar{x} + \delta x(t))\right) =$$

$$-\hbar g_{om}\left(|\bar{a}|^2 + \bar{a}^*\delta a(t) + \bar{a}\delta a^*(t) + |\delta a(t)|^2\right)$$

(3.26)

where $\bar{\Delta} \equiv \Delta - g_{om}\bar{x}$ is the effective detuning including the static cavity displacement. Eliminating the static terms with the aid of (3.24) gives the time-varying small signal amplitudes $\delta a(t)$ and $\delta x(t)$

$$\delta\dot{a}(t) = \left[i\bar{\Delta} - \frac{\kappa}{2}\right]\delta a(t) - i\bar{a}g_{om}\delta x(t)$$

$$m_{eff}\left(\delta\ddot{x}(t) + \Gamma_m\delta\dot{x}(t) + \omega_m^2\delta x(t)\right) = -\hbar g_{om}\left(\delta a(t) + \delta a^*(t)\right)$$

(3.27)

assuming that the second-order small signal products are negligibly small and $\bar{a} = \bar{a}^*$, which is always possible by adjusting the (physically irrelevant) phase of the input field.

Linearized coupled equations in (3.27) are perhaps easiest to solve in frequency domain. Applying Fourier transform, we get

$$-i\omega\delta a(\omega) = \left(i\bar{\Delta} - \frac{\kappa}{2}\right)\delta a(\omega) - i\bar{a}g_{om}\delta x(\omega)$$

$$m_{eff}\left(\omega_m^2 - \omega^2 - i\omega\Gamma_m\right)\delta x(\omega) = -\hbar g_{om}\bar{a}\left(\delta a(\omega) + \delta a^*(-\omega)\right)$$

(3.28)

The small signal optical field $\delta a(\omega)$ and its conjugate are then

$$\delta a(\omega) = \frac{-i\bar{a}g_{om}}{\kappa/2 - i(\bar{\Delta} + \omega)}\delta x(\omega)$$

$$\delta a^*(-\omega) = \frac{i\bar{a}g_{om}}{\kappa/2 + i(\bar{\Delta} - \omega)}\delta x(\omega)$$

(3.29)

where the relation $\delta x^*(-\omega) = \delta x(\omega)$ is used since $\delta x(\omega)$ is symmetric and real. Equation (3.29) shows that the intracavity optical field gets modulated with displacement which in
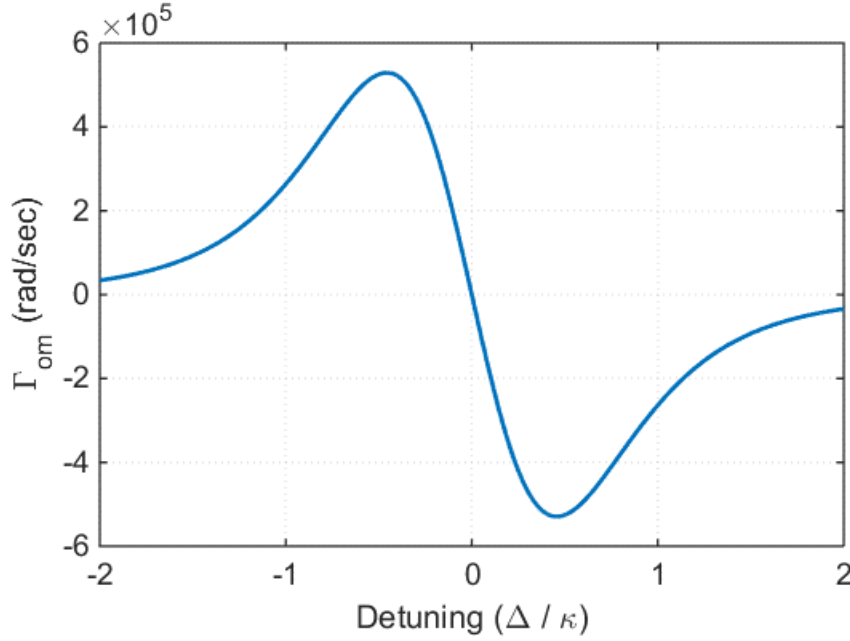
Figure 3.4: A plot of Γ_{om} with respect to detuning frequency, normalized to cavity loss rate κ. A resonant drive ($\Delta = 0$) yields $\Gamma_{om} = 0$ and only produces a static effect. Blue detuning ($\Delta > 0$) results in negative Γ_{om} which then reduces the total damping. Largest value of Γ_{om} is achieved around $\Delta \approx 0.3\kappa$.

turn gives rise to an oscillating force equal to

$$
\begin{aligned}
\delta F_{rp}(\omega) &= -\hbar g_{om}\bar{a}\left(\delta a(\omega) + \delta a^*(-\omega)\right) \\
&= -\hbar g_{om}^2|\bar{a}|^2 \left(\frac{-i\delta x(\omega)}{\kappa/2 - i(\bar{\Delta}+\omega)} + \frac{i\delta x(\omega)}{\kappa/2 + i(\bar{\Delta}-\omega)}\right) \\
&= -\hbar g_{om}^2|\bar{a}|^2 \left(\frac{\bar{\Delta}+\omega - i\kappa/2}{\kappa^2/4 + (\bar{\Delta}+\omega)^2} + \frac{\bar{\Delta}-\omega + i\kappa/2}{\kappa^2/4 + (\bar{\Delta}-\omega)^2}\right)\delta x(\omega)
\end{aligned}
\tag{3.30}
$$

Grouping the terms in the bottom equation of (3.28) as the internal forces, the response of the resonator to an externally applied force changes according to

$$
\begin{aligned}
F_{ex} &= m_{eff}\left(\omega_m^2 - \omega^2 - i\omega\Gamma_m\right)\delta x(\omega) \\
&\quad + \hbar g_{om}^2|\bar{a}|^2 \left(\frac{\bar{\Delta}+\omega - i\kappa/2}{\kappa^2/4 + (\bar{\Delta}+\omega)^2} + \frac{\bar{\Delta}-\omega + i\kappa/2}{\kappa^2/4 + (\bar{\Delta}-\omega)^2}\right)\delta x(\omega) \\
&= m_{eff}\left[-\omega^2 - i\omega(\Gamma_m + \Gamma_{om}) + \left(\omega_m^2 + \frac{k_{om}}{m_{eff}}\right)\right]\delta x(\omega)
\end{aligned}
\tag{3.31}
$$

where the newly introduced terms

$$
\begin{aligned}
k_{om} &= \hbar g_{om}^2 |\bar{a}|^2 \left(\frac{\bar{\Delta} + \omega}{(\kappa/2)^2 + (\bar{\Delta} + \omega)^2} + \frac{\bar{\Delta} - \omega}{(\kappa/2)^2 + (\bar{\Delta} - \omega)^2} \right) \\
\Gamma_{om} &= \frac{\hbar g_{om}^2 |\bar{a}|^2}{m_{eff} \omega} \left(\frac{\kappa/2}{(\kappa/2)^2 + (\bar{\Delta} + \omega)^2} - \frac{\kappa/2}{(\kappa/2)^2 + (\bar{\Delta} - \omega)^2} \right)
\end{aligned}
\tag{3.32}
$$

modifies the dynamics of the mechanical resonator by changing its effective stiffness (or equivalently, mechanical resonance frequency) and damping.

There are several parameters that determines the magnitude and the sign of Γ_{om} and k_{om} including the device parameters such as m_{eff} and κ as well as the external operating conditions such as the input power (which governs $|\bar{a}|^2$) and detuning. Operating conditions allow controlling the device behavior in a wide range. Obviously, higher input power intensifies the optomechanical effects and increases the magnitude of Γ_{om} and k_{om}. On the other hand, detuning governs both magnitude and sign of Γ_{om} and k_{om} such that the optomechanical effects can be reversed or nulled by changing the detuning. Figure 3.4 presents a plot of Γ_{om} with respect to detuning for a fixed input power. It is evident that $\Gamma_{om} = 0$ for exact resonant excitation ($\Delta = 0$) and red detuning ($\Delta < 0$) yields a positive Γ_{om} that increases the total damping. This corresponds to the case where the thermal noise driven mechanical motion is further damped with a positive Γ_{om} that effectively reduces the noise temperature (so-called optomechanical cooling). On the other hand, the opposite is true for blue detuning ($\Delta > 0$). Negative Γ_{om} reduces the total damping that then results in a larger mechanical displacement at the mechanical resonance frequency. Effectively, the mechanical resonator exhibits a larger Q_m in the blue detuning case. If Γ_{om} approaches (or exceeds) $-\Gamma_m$, then $Q_m \to \infty$, which means that the oscillations will be sustained in the system. In this case, vibrational energy lost in the mechanical resonator in each cycle is supplied by the optical field and the device continues to oscillate as long as the loop is preserved. The effect of blue and red detuning on k_{om} is opposite of Γ_{om}, where blue (red) detuning increases (decreases) the total stiffness which then increases (decreases) the oscillation frequency.

3.5 Optomechanical Oscillators

As explained in Section 3.4.2, a blue detuned laser input reduces the effective damping of the optomechanical resonator and if optomechanically induced damping Γ_{om} completely cancels out the intrinsic Γ_m the system becomes unstable. This is explained in the context of control theory with the pole-zero diagram in Figure 3.5 where the poles cross the imaginary axis when $\Gamma_{om} + \Gamma_m = 0$, at which point the system exhibits sustained oscillations.

It is then straightforward to derive the conditions for onset of self-sustained oscillations by using the relation

$$
\Gamma_{om} = \frac{\hbar g_{om}^2 |\bar{a}|^2}{m_{eff} \omega} \left(\frac{\kappa/2}{(\kappa/2)^2 + (\bar{\Delta} + \omega)^2} - \frac{\kappa/2}{(\kappa/2)^2 + (\bar{\Delta} - \omega)^2} \right) = -\Gamma_m
\tag{3.33}
$$
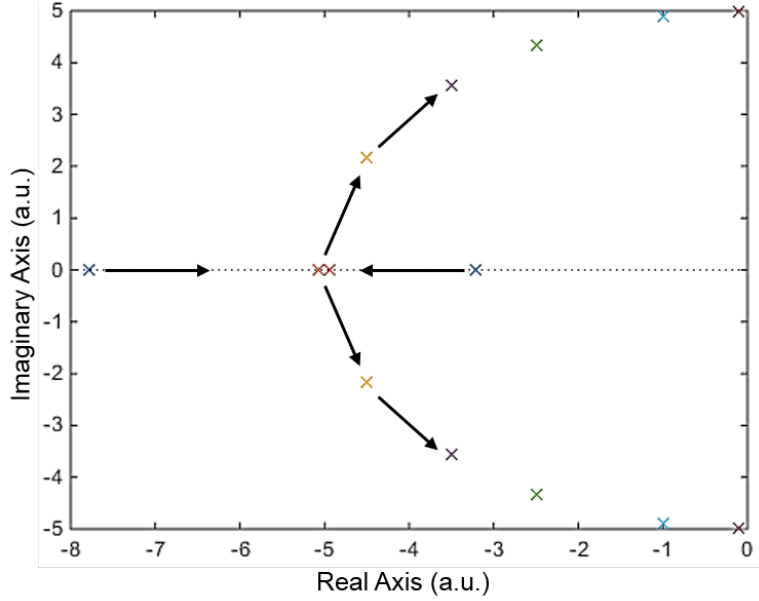
Figure 3.5: Pole-zero diagram of an oscillatory system with two poles moving in the direction of the arrows with increasing Q (reduced damping). When the system's Q is increased beyond the critical damping point, the poles have non-zero imaginary values and approach further closer to the imaginary axis as the Q keeps increasing. If the damping is completely removed, poles become purely imaginary and oscillations are self-sustained in the system.

Plugging in Equation (3.18) and replacing the photon flux with the input laser power $P_{in} = \hbar \omega_o |s_{in}|^2$, Equation (3.33) becomes

$$\frac{g_{om}^2 P_{in}}{\omega_o m_{eff} \omega} \left(\frac{\kappa_{ex}}{(\kappa/2)^2 + \bar{\Delta}^2} \right) \left(\frac{\kappa/2}{(\kappa/2)^2 + (\bar{\Delta} + \omega)^2} - \frac{\kappa/2}{(\kappa/2)^2 + (\bar{\Delta} - \omega)^2} \right) = -\Gamma_m \qquad (3.34)$$

Note that Γ_{om} has a frequency dependence (more so for ultra-high-Q_o cavity case) and while determining the oscillation condition it needs to be calculated at the oscillation frequency, which is modified due to optical stiffening

$$\omega_{osc} = \omega_m + \sqrt{k_{om}/m_{eff}} \qquad (3.35)$$

Equation (3.34) outlines the necessary condition for oscillation. It describes a threshold behavior where the externally supplied input power needs to be large enough to ensure $\Gamma_{om} = -\Gamma_m$. Isolating the input power and emphasizing the threshold behavior by denoting $P_{in} = P_{th}$ when $\Gamma_{om} = -\Gamma_m$ yields

$$P_{th} = \frac{-\Gamma_m \omega_o m_{eff} \omega_{osc}}{g_{om}^2} \times$$
$$\left(\frac{(\kappa/2)^2 + \bar{\Delta}^2}{\kappa_{ex}} \right) \left(\frac{\kappa/2}{(\kappa/2)^2 + (\bar{\Delta} + \omega_{osc})^2} - \frac{\kappa/2}{(\kappa/2)^2 + (\bar{\Delta} - \omega_{osc})^2} \right)^{-1} \qquad (3.36)$$
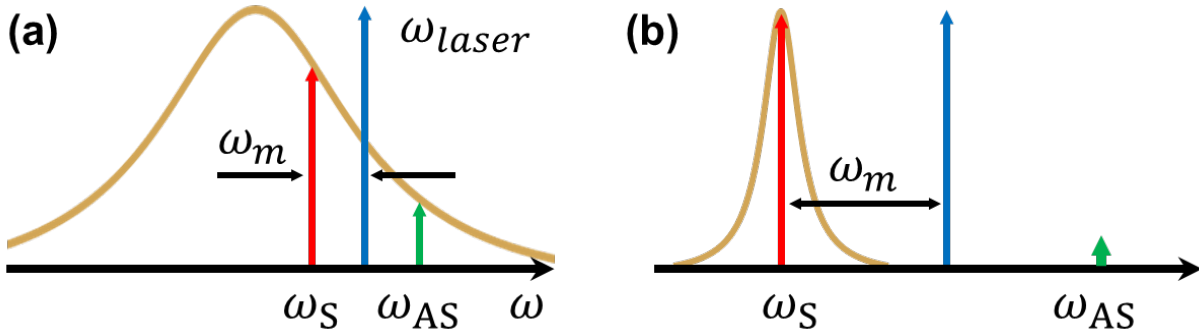
Figure 3.6: OMO operation in the case of (a) unresolved sideband and (b) resolved sideband regimes. In the unresolved sideband regime, laser frequency is set at the higher frequency tail of the optical resonance, creating two asymmetric sidebands (separated by ω_m) that reside in and weighted by the cavity Lorentzian. The amplitude difference between the (larger) Stoke sideband amplitude and the (lower) anti-Stoke sidebands due to blue detuning results in a net energy transfer from the optical field to the mechanical, increasing the phonon number in the mechanical mode. In the resolved side band regime ($\kappa << \omega_m$), laser needs to park outside of the cavity resonance to create enough asymmetry between the sidebands. Maximum asymmetry occurs when the detuning is equal to the frequency of the mechanical mode.

Evidently, the threshold power depends on many parameters and Equation (3.36) is a complete expression that predicts P_{th} for all cases. However, there are two distinct regimes where the threshold power dependence is significantly different and an approximate expression for P_{th} would allow more intuitive understanding for low-threshold design and operation. First is the unresolved sideband regime (USR) where the oscillation frequency is much smaller than the optical linewidth ($\kappa >> \omega_m$) so that the sidebands produced by the mechanical modulation fall within the optical cavity Lorentzian. Figure 3.6(a) depicts this case where the lower (Stokes) sideband is larger than the upper (anti-Stokes) sideband for a blue detuned laser, which also explains the mechanical gain produced in the blue detuned excitation case. The asymmetry between the sidebands results in energy imbalance between the higher energy photons $\hbar(\omega_o + \omega_m)$ and lower energy photons $\hbar(\omega_o - \omega_m)$, which leads to larger number of phonons. Red detuning produces the opposite effect, where the energy imbalance (larger anti-Stokes, smaller Stokes sidebands) requires phonon energy to be taken away from the system. In the USR regime, both detuning and optical linewidth are much larger than the oscillation frequency ($\kappa, \bar{\Delta} >> \omega_m$). This allows the following approximation for the 3$^{\text{rd}}$ fraction in Equation (3.36)

$$\left(\frac{\kappa/2}{(\kappa/2)^2 + (\bar{\Delta} + \omega_{osc})^2} - \frac{\kappa/2}{(\kappa/2)^2 + (\bar{\Delta} - \omega_{osc})^2} \right) \approx -\frac{32\kappa\omega_{osc}\bar{\Delta}}{(\kappa^2 + 4\bar{\Delta}^2)^2} \qquad (3.37)$$

Substituting the approximate expression back in (3.36) yields an approximate formula for

the threshold power in USR

$$P_{th}^{USR} \approx \frac{\Gamma_m \omega_o m_{eff}}{g_{om}^2} \frac{(\kappa^2 + 4\bar{\Delta}^2)^3}{128 \kappa \kappa_{ex} \bar{\Delta}} \tag{3.38}$$

The second case is the resolved sideband regime (RSR) where the oscillation frequency is much larger than the optical linewidth ($\kappa << \omega_m$) so that the sidebands produced by the mechanical modulation lie outside of the optical cavity Lorentzian. In this regime, the pump laser is detuned far from the cavity resonance, as presented in Figure 3.6(b), to create asymmetry between the stokes and anti-stokes sidebands, where the oscillation frequency and detuning are much larger than the optical linewidth ($\kappa << \bar{\Delta}, \omega_m$). Further assuming that the detuning is exactly adjusted for maximum asymmetry $\bar{\Delta} = \omega_m$, the approximate P_{th} in the RSR becomes

$$P_{th}^{RSR} \approx \frac{\omega_o m_{eff} \omega_{osc}^4}{2 g_{om}^2 Q_m} \tag{3.39}$$

with the assumption of $\kappa = \kappa_{ex}$.

The threshold power in the USR case will be further investigated in the following sections together with the oscillator model. Here, it is appropriate to make a few observations for the RSR operation of OMO before proceeding to the oscillator model. First, it is independent of the optical-Q, which is quite different than the USR case where the order of κ (or $1/Q_o$) is three. Second, it scales with $1/Q_m$ and $1/g_{om}^2$, which motivate achieving higher Q_m and larger coupling that might be possible with smaller device design. OMO's operating in this regime have achieved ultra-low threshold powers [14] in the order of $100\,\mu\text{W}$.

3.5.1 Conventional Oscillator Theory

Physics community is very familiar with forced and parametric resonance, but usually not with self-oscillation [32], which is very well known by electrical engineers for its use in a variety of circuits as well as its undesired presence in systems intended to be stable, such as amplifiers. Engineers have developed their understanding of oscillators with the feedback systems theory that we will cover here briefly. The basic feedback oscillator has two elements: a gain and a feedback component with transfer functions $A(i\omega)$ and $\beta(i\omega)$, respectively, as represented by the boxes in Figure 3.7 that form what is called a feedback loop. Here, the summing point takes a portion of the output (amount of which is determined by $\beta(i\omega)$) and feeds it back to the amplifier together with the input. This is a general picture that describes any feedback system, such as op-amp circuits employing feedback to improve the amplifier bandwidth. In this case the feedback signal is subtracted (or added with an opposite phase) from the input signal so this type of feedback is called negative feedback. In the oscillator case, the feedback is positive, meaning that the feedback signal is added in phase at the summing point. Note that the input signal at this point is not an externally applied signal for an oscillator, rather it is an undesired noise component such as thermal noise entering

the amplifier. With reference to Figure 3.7, the input-output relation (transfer function) of
the feedback loop is
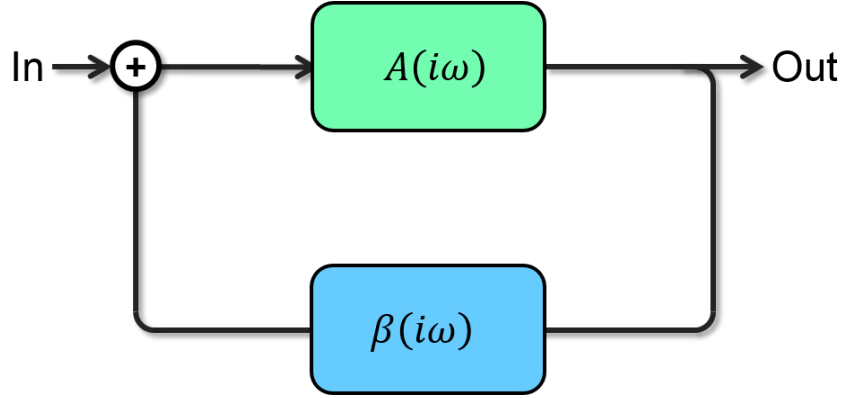
Figure 3.7: Generic feedback loop. In a feedback oscillator, green block with transfer function
$A(i\omega)$ represents the amplifier and blue block with transfer function $\beta(i\omega)$ represents the
resonator. Resonator is the feedback element that sets the frequency of the self-sustained
oscillation in the loop.

$$H(i\omega) = \frac{A(i\omega)}{1 - A\beta(i\omega)} \qquad (3.40)$$

In a self-sustained oscillator, the output of the system is a sinusoidal signal with virtually
no input. This happens when the system allows input noise to grow exponentially until
a mechanism (usually some sort of non-linearity) causes the gain to drop at a large signal
amplitude, limiting the amplitude after the transient exponential growth (self-limiting) in
the limit-cycle. This happens when the denominator of Equation (3.40) becomes zero, or
equivalently

$$A\beta(i\omega_{osc}) = 1 \qquad (3.41)$$

which is known as the Barkhausen condition. It states that the gain $A(i\omega)$ of the sustaining
amplifier needs to compensate for the resonator $\beta(i\omega)$ loss at the oscillation frequency $\omega = \omega_{osc}$ and the signal needs to be added in phase in each cycle, i.e., it has to repeat itself after
going around the loop. This means that the loop phase $\angle A\beta(i\omega)$ needs to be zero or multiple
of 2π at $\omega = \omega_{osc}$. In terms of magnitude and phase

$$\begin{aligned}|A\beta(i\omega_{osc})| &= 1 \\ \angle A\beta(i\omega_{osc}) &= 0\end{aligned} \qquad (3.42)$$

is the condition for self-oscillation (at ω_{osc}).

   In practice, oscillations start from noise or a transient event such as closing a switch, and
the loop gain is set to a value larger than one ($|A\beta(i\omega_{osc})| > 1$) for oscillations to grow at
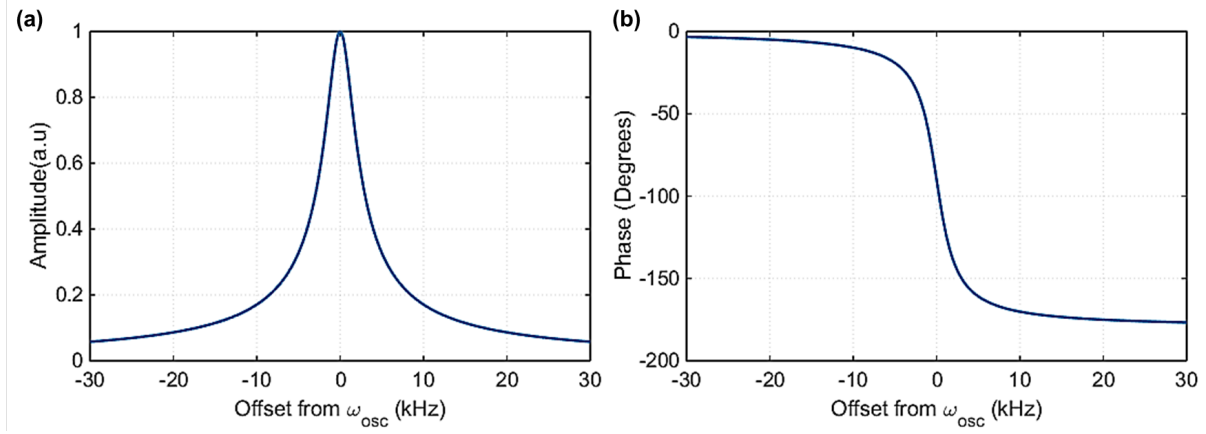
Figure 3.8: Magnitude (a) and phase (b) plots of a feedback resonator $\beta(i\omega)$ with a bandpass biquad (Lorentzian) response.

the startup. In most cases, the resonator frequency response $|\beta(i\omega)|$ is a sharp Lorentzian centered at $\omega = \omega_m \approx \omega_{osc}$ (c.f., Figure 3.8) and amplifier gain is independent of frequency. Additional phase shift in the loop (due to amplifier, transmission lines etc.) can add up to the resonator phase and provide a total phase of 2π necessary for oscillation, though the frequency at which the phase shift is 2π might be slightly shifted from the resonator center frequency ω_m. If the loop doesn't have enough phase shift at the desired oscillation frequency, phase shifters can be added to the loop. After the oscillations start and grow from noise level to a large oscillation amplitude, the loop gain drops to unity and the system reaches a stationary condition.
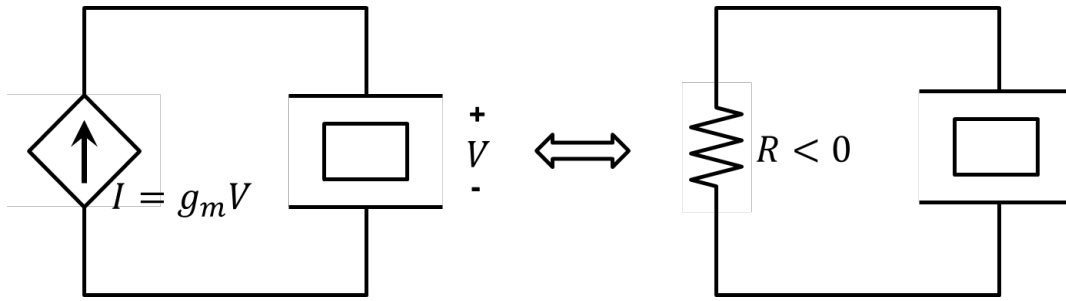
Figure 3.9: (a) Pictorial presentation of a negative resistance oscillator referenced to a quartz resonator. The active element modeled as a voltage controlled current source produces a current proportional to the voltage across the quartz resonator where the direction of the current indicates a power flow from the current source to the resonator. (b) The active element can be modeled with a negative resistance since it produces power (as opposed to a power-absorbing resistor) while the current on it linearly depends on the voltage. Oscillations instigate if negative R cancels out the quartz impedance such that $R_{tot} \le 0$.

A physical example for the abstract picture of Figure 3.7 is the well-know quartz oscillator, where the feedback element (resonator) is the quartz crystal with a complex impedance $Z(i\omega) = V(i\omega)/I(i\omega)$ that takes a real value at resonance, and a transconductance amplifier takes the voltage of the resonator and delivers a current $I = G_m V$, as illustrated in Figure 3.9 (a). Here, the amplifier supplies power (in contrast to a resistor which absorbs power) as indicated by the direction of the current, meaning that the transconductance G_m is negative. In this case the amplifier is modeled by a mere resistor with a negative value, and the configuration of Figure 3.9 (b) is called negative resistance oscillator. It is now our goal to represent the OMO system with a similar feedback loop to develop an understanding of its phase noise and allow oscillator designers to have a more intuitive model to design high performance OMOs.

3.5.2 Engineering Modeling of Optomechanical Oscillators

We would like to now use Equations (3.16) and (3.17) to describe the system as a feedback loop and derive conditions for oscillator start-up and steady state using the feedback theory. First, it is straightforward to identify the feedback element β, which is formed by the mechanical resonator just like in the electronic quartz oscillator case. We choose the input-output variables as force F and velocity $\dot{X}$ since it allows a representation that is completely analogous to an $L - C - R$ electrical network with voltage input - current output.

$$\beta(i\omega) = \frac{\dot{X}}{F} = \frac{1}{i\omega m_{eff} + m_{eff}\Gamma_m + \frac{k}{i\omega}} \tag{3.43}$$

similar to derived resonator response in equivalent circuit modeling of Chapter 2. The mechanical resonator filters any off-resonance signal with its high Q_m and feeds it back to the inherent amplifier mechanism.

Second, we derive the amplifier component $A(i\omega)$ using Equation (3.16). As explained in Section 3.4.2 the optical field amplitude cannot change instantaneously with the cavity position, so the force follows the position with a time lag. This retardation can be modeled by a response function describing the time delay [33]

$$F_{rp}(x(t)) = F(x_o) + \int_0^t \frac{\partial F(x(t'))}{\partial t'} h(t - t')dt' = F(x_o) + \left(\frac{\partial F}{\partial t} * h\right)(t) \tag{3.44}$$

where we assume that the force reaches to equilibrium with an exponential decay function $h(t) = 1 - e^{-t\kappa}$. The constant term in Equation 3.44 only causes a static shift on the cavity position so it can be dropped without the loss of generality. The time derivative of the force function can be expressed as product of partial derivatives, and using small signal approximation around a static displacement $x = \bar{x}$ yields

$$\frac{\partial F}{\partial t} = \left(\frac{\partial \bar{F}}{\partial x}\bigg|_{x=\bar{x}}\right)\left(\frac{\partial x}{\partial t}\right) = \nabla \bar{F}\frac{\partial x}{\partial t} \tag{3.45}$$
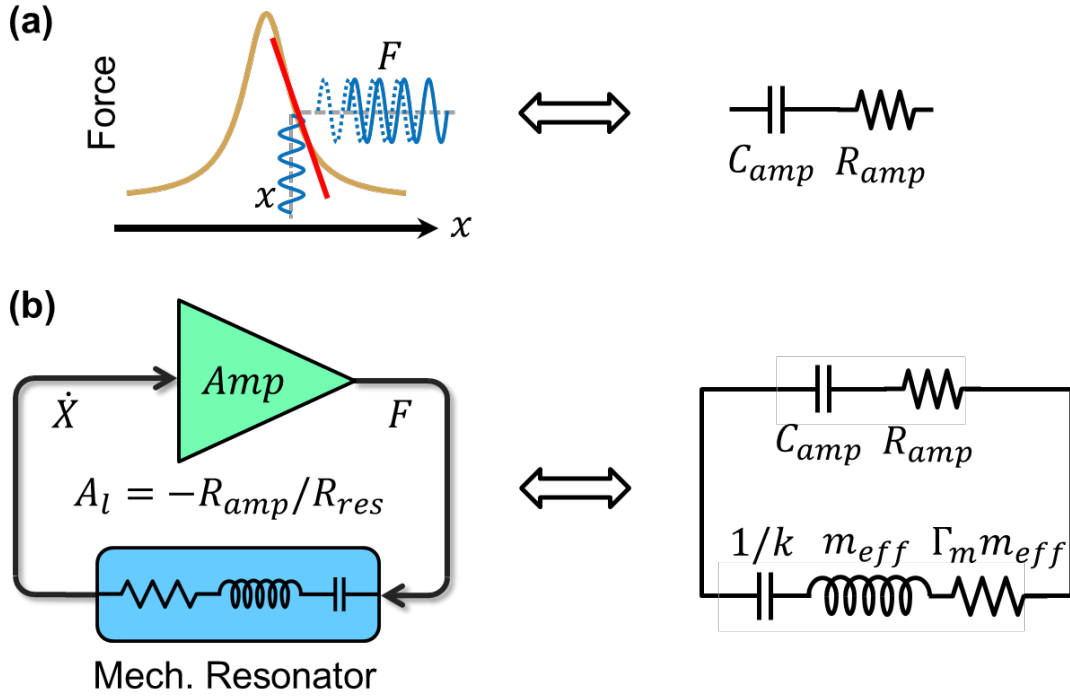
Figure 3.10: (a) Modeling of the inherent amplifier mechanism in OMO. The optical force is a function of the laser detuning $(\Delta(x))$, and in return, position of the cavity boundary (x). This position-force curve is similar to the I-V curve of a transistor amplifier where the small signal voltage input produces a corresponding current, which is modeled as a transconductance "g_m" or a negative resistance. In the OMO "amplifier" small signal displacement produces a corresponding oscillating force with a time delay, which again can be modeled as a negative resistance and an additional capacitor. (b) Closed loop feedback model of the OMO. The mechanical resonator acts as the feedback element that sets the oscillation frequency while the amplifier sustains the oscillations.

Substituting Equation (3.45) in (3.44) and transforming to frequency domain, the velocity-to-force transfer function becomes

$$A(i\omega) = \frac{F}{\dot{X}} = \nabla\bar{F}H(i\omega) = \nabla\bar{F}\frac{\kappa}{\kappa + i\omega}\frac{1}{i\omega} \qquad (3.46)$$

which describes the response of the optical force to cavity displacement (or velocity). In this regard, $\nabla\bar{F}$ is the gain from velocity (input) to force (output) just like a transistor amplifier converts voltage input to current output. Similar to the case where bias voltage sets the operating point and consequently the transconductance gain (slope of the I-V curve) for a transistor, laser detuning sets the gain in an optomechanical oscillator by setting the slope of the force-displacement curve, as depicted in 3.10(b). The slope is negative for blue detuning

($\Delta >$), positive for red detuning ($\Delta < 0$) and zero for resonant drive ($\Delta = 0$), indicating that the optomechanical feedback can be positive, negative or zero depending on the operating point. This feedback loop is further described in 3.10(c) with an analogy to an electronic oscillator using an R-L-C network as the frequency selective tank and an electronic amplifier to sustain the oscillation. In the optomechanical loop, the mechanical resonator realizes the frequency selective tank, whereas the optical cavity storing the optical force realizes the two functions described by $A(i\omega)$: an amplifier followed by a low-pass-filter. Since the cut-off frequency of this filter is much larger than the oscillation frequency, its effect is only a small phase shift that retards the force with respect to the input displacement. However, this is an important effect since the total phase shift has to be 360° in the oscillator loop.

To instigate oscillations, the loop gain $A_l = A\beta(i\omega)$ needs to be at least 1 (Barkhausen condition), which dictates that:

$$\nabla\bar{F}\frac{\kappa}{\kappa + i\omega}\frac{1}{i\omega} = i\omega m_{eff} + m_{eff}\Gamma_m + \frac{k}{i\omega} \tag{3.47}$$

Equating real and imaginary parts and observing that $\kappa/(\kappa + i\omega) \approx (\kappa - i\omega)/\kappa$ in the low-frequency regime ($\kappa >> \omega_m$), self-oscillation conditions read

$$\frac{\nabla\bar{F}}{\kappa} = -m_{eff}\Gamma_m$$
$$\omega^2 = \frac{k}{m_{eff}} - \frac{\nabla\bar{F}}{m_{eff}} \tag{3.48}$$

Note that this is equivalent to conditions (3.33) and (3.35) for onset of self-oscillations derived in Section 3.4.2, with the corresponding Γ_{om} and k_{om}

$$\Gamma_{om} = \frac{\nabla\bar{F}}{m_{eff}\kappa}$$
$$k_{om} = -\nabla\bar{F} \tag{3.49}$$

Equation (3.48) states that optomechanically induced stiffness modifies the oscillation frequency such that $\omega_{osc} = \omega_m + \sqrt{k_{om}/m_{eff}}$ is the frequency of oscillation and threshold condition $\Gamma_{om} = -\Gamma_m$ needs to be satisfied.

Pursuant to derive the threshold condition for oscillation in terms of the design parameters, we can replace the expression for $\nabla\bar{F}$ in Γ_{om}. Using (3.19)

$$\nabla\bar{F} = \frac{\partial\bar{F}}{\partial x}\bigg|_{x=\bar{x}} = \frac{-\hbar g_{om}^2 32|s_{in}|^2\kappa_{ex}\bar{\Delta}}{(\kappa^2 + 4\bar{\Delta}^2)^2} \tag{3.50}$$

Γ_{om} becomes

$$\Gamma_{om} = \frac{-g_{om}^2\omega_o 32P_{in}\kappa_{ex}\bar{\Delta}}{(\kappa^2 + 4\bar{\Delta}^2)^2}\frac{1}{m_{eff}\kappa} \tag{3.51}$$

Remember that $\bar{\Delta}$ and κ_{ex} are operating conditions that can be tuned for optimum operation. Setting $\bar{\Delta} = \kappa/2\sqrt{3}$ and $\kappa_{ex} = \kappa/4$ for maximum gain (or equivalently, minimum threshold power) yields:

$$\Gamma_{om}^{max} = -\frac{3\sqrt{3}}{4}\frac{g_{om}^2 P_{in}}{\omega_o m_{eff}\kappa^3} \approx -\frac{1}{2}\frac{P_{in}Q_o^3}{m_{eff}R^2\omega_o^2} \tag{3.52}$$

and finally the minimum threshold power becomes

$$P_{th} = \frac{2\Gamma_m m_{eff}R^2\omega_o^2}{Q_o^3} = \frac{2m_{eff}R^2\omega_m\omega_o^2}{Q_m Q_o^3} \tag{3.53}$$

Equation (3.53) agrees very well with Equation (3.38) derived earlier with the established OMO theory, which has been validated with experiments [33],[16]. However, for the devices introduced in Chapter 4 that operate deeply in USR, experimentally measured threshold power is lower than the predicted values from Equations (3.53) and (3.38). We have seen that the theoretical threshold power agrees well with the measurement when it is scaled by a factor κ/ω_m. This suggests that at the startup of the oscillations amplifier has a larger (negative) resistance, which reduces the threshold power. In the following discussions, we will keep this into account and just scale the power values accordingly.

Following the representation of negative resistance crystal oscillator model, we can now model the OMO as a negative resistance oscillator. Using the circuit convention with current entering the positive terminal, the amplifier's equivalent impedance $F/\dot{X}$ becomes

$$Z_{amp} = -\nabla\bar{F}\frac{\kappa - i\omega}{\kappa}\frac{1}{i\omega} = -\nabla\bar{F}\frac{1}{i\omega} + \nabla\bar{F}\frac{1}{\kappa} \tag{3.54}$$

from which amplifier's equivalent resistance and capacitance simply follow as

$$R_{amp} = \nabla\bar{F}\frac{1}{\kappa}$$
$$C_{amp} = -\frac{1}{\nabla\bar{F}} \tag{3.55}$$

which take negative and positive values, respectively, for blue detuning, as expected. In this case, the oscillation condition is

$$R_{amp} + R_{res} = 0$$
$$\omega_{osc} = \frac{1}{\sqrt{L_{res}C_{eq}}} \tag{3.56}$$

where C_{eq} is the equivalent series capacitance ($C_{eq}^{-1} = C_{amp}^{-1} + C_{res}^{-1}$) of the oscillator circuit, $L_{res} = m_{eff}$, and $R_{res} = b = \Gamma_m m_{eff}$ as derived in Chapter 2. Equation (3.56) is exactly equivalent to (3.48) with the above definitions. Also, a DC loop gain can be defined in terms of the resistor values

$$A_l = -\frac{R_{amp}}{R_{res}} \tag{3.57}$$

to explain oscillator behavior at the startup and steady state. As explained in Section 3.5.1, in practice the system has a larger loop gain $(A_l > 1)$ at the startup to allow oscillations to grow from noise and the gain gradually decreases with larger oscillation amplitude so the total loop gain drops to 1 at the steady state.
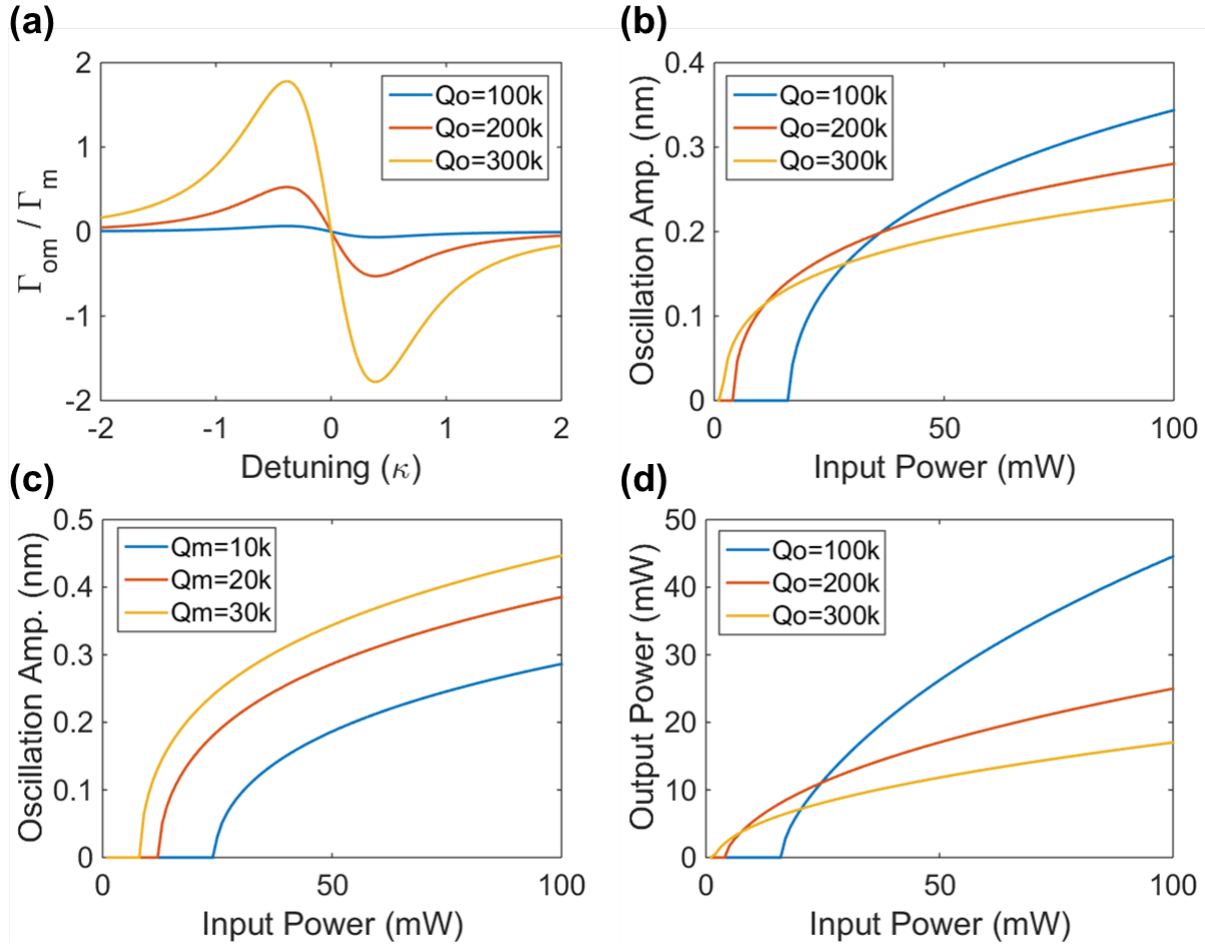
Figure 3.11: (a) OMO loop gain for the feedback oscillator model for several values of Q_o. Larger Q_o creates a larger slope in the displacement-force curve which in turn creates a larger loop gain. (b) Oscillation amplitude starts increasing at lower power levels for higher Q_o values, but it saturates earlier compared to lower Q_o case. (c) High-Q_m decreases the oscillation threshold power without saturating the oscillation amplitude as opposed to the case with higher Q_o. (d) Calculated optical power at the OMO output for the displacement values in (b), showing a similar saturation behavior.

Figure 3.11(a) shows plots of the loop gain with respect to detuning for different values of Q_o, from which it is evident that the gain rolls-off from its maximum value as the amplitude grows. Since the loop gain will be equal to 1 at the steady state, the oscillation amplitude

can be estimated by finding the excursion from the bias point which makes the average value equal to 1. Figure 3.11(b) plots oscillation amplitude vs input power for several Q_o values. Since the threshold power has inverse cubic dependence on Q_o, device with higher Q_o start to oscillate at much less input power. However, higher Q_o exhibits a sharper gain roll-off as the amplitude increase, which results in saturation at a lower oscillation amplitude compared to a lower Q_o device. In this regard, although higher Q_o is desired for low threshold power operation, it is also a limiting factor for the oscillator performance since higher oscillation amplitude is desired for lower phase noise. Higher Q_m, on the other hand, both helps reducing the threshold power and reaching a higher oscillation amplitude for a given input power as depicted in Figure 3.11(c).

3.6   Output Spectrum

Finally, the modulated optical field in the device couples back to the tapered fiber that delivers the input field, hence the output optical field comprises of both the laser input and the coupled field:

$$s_{out} = s_{in} - a\kappa_{ex} \tag{3.58}$$

It is possible to calculate the exact output field and output power by solving the coupled equations but this is a rather involved calculation. Instead of solving the field amplitudes, the cavity transmission

$$\frac{P_{out}}{P_{in}} = \frac{4\Delta^2 + (\kappa - 2\kappa_{ex})^2}{(4\Delta^2 + \kappa^2)} \tag{3.59}$$

can provide the oscillating output power once the displacement amplitude is known. Figure 3.11(d) plots the output power of OMO for different Q_o values, which show a similar trend with the displacement plots of Figure 3.11(b), where the output power saturates at a lower amplitude.

3.7   OMO Phase Noise

Phase noise modeling of oscillators is not trivial due to non-linear, time-varying nature of oscillators as well as presence of various noise sources that convert into phase noise via different mechanisms. This is in part why there exist many phase noise models for electronic oscillators, where models consider only a subset of the noise sources and/or have restrictive assumptions about the system which are applicable to only a limited class of oscillators.

One famous and widely used model for tuned tank oscillators is Leeson's model [34] that can explain general phase noise behavior of such oscillators with empirical arguments in a relatively simple way. It has also found its use in explaining phase noise performance of optomechanical oscillators [35],[4],[36] as they also employ a (mechanical) tuned tank for frequency selection. In the following section we will briefly discuss the power and limitations

of Leeson's model and investigate it from an optomechanical oscillator designer's point of view.

3.7.1   Leeson's Model
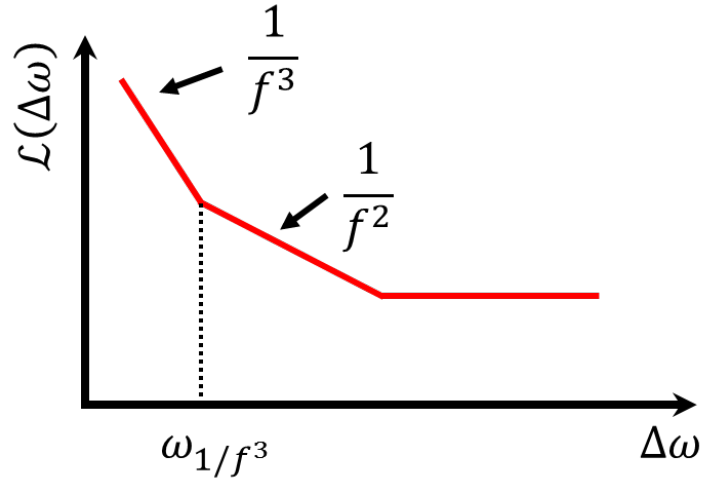
Figure 3.12: Typical phase noise behavior of an electronic oscillator modeled by Leeson's equation with $1/f^3$, $1/f^2$ and flat noise regions.

Leeson's model is perhaps the most popular model for phase noise in electronic oscillators as experimental data usually follow the model's predictions relatively well. The model is based on the empirical observation of phase noise frequency spectrum with decaying and flat portions within and out of the resonator feedback half-bandwidth. With an LTI system assumption, the phase noise spectrum is derived for a given "input phase fluctuation", $\Delta\theta(t)$, of the oscillator due to noise and parameter variations, which is translated into frequency error through the phase-frequency relationship of the frequency network:

$$\dot{\phi} = \frac{\omega_o}{2Q}\Delta\theta \tag{3.60}$$

where ϕ is the "output" phase that contains the measured noise spectrum, $S_\phi(\omega)$. Thus, within the feedback half-bandwidth $\omega_o/2Q$ the spectrum of frequency $S_{\dot{\phi}}$ is just a scaled version of the input phase noise spectrum:

$$S_{\dot{\phi}} = (\frac{\omega_o}{2Q})^2 S_{\Delta\theta} \tag{3.61}$$

The argument for frequencies outside of the feedback half-bandwidth is that the noise is no longer filtered by the resonator and the power spectral density of the output phase is identical to the input phase noise spectrum. Combining with the (3.61)

$$
\begin{cases}
S_{\dot{\phi}} = \left(\frac{\omega_o}{2Q}\right)^2 S_{\Delta\theta} & \omega < \frac{\omega_o}{2Q} \\
S_{\phi} = S_{\Delta\theta} & \frac{\omega_o}{2Q} < \omega
\end{cases}
$$

and using the relation $S_{\phi}(\omega) = \omega^{-2} S_{\dot{\phi}}(\omega)$ yields

$$
S_{\phi} = S_{\Delta\theta} \left[1 + \left(\frac{\omega_o}{2Q\omega} \right)^2 \right] \tag{3.62}
$$

The results of Leeson's derivation so far tell us that the feedback network employed in the oscillator filters out the noise in the vicinity of the carrier, while at frequencies out of the feedback (half) bandwidth the noise reaches to the output without any filtering. It is clear that the tank Q is important in reducing the close-to-carrier noise but the "input" phase noise spectrum remains unknown.
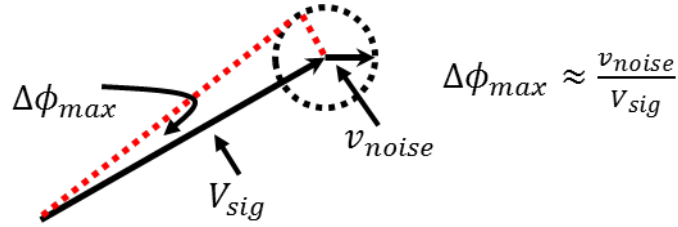
Figure 3.13: Pictorial illustration of conversion from voltage noise to phase noise. Arrows are the phasor representations of the signal and noise voltages where noise vector adds to signal and rotates at an arbitrary frequency ω. At this frequency maximum phase deviation is equal to $\tan^{-1}(v_{noise}/V_{signal}) \approx v_{noise}/V_{signal}$, and RMS deviation is equal to $\Delta\phi_{rms} = v_{noise}/V_{signal}$ when the fluctuating component at $-\omega$ is also considered. This yields a phase noise spectral density of $S_{\Delta\theta}(\omega) = v_{noise}^2/V_{signal}^2 = P_{noise}/P_{signal}$.

For the input phase errors, Leeson model assumes a spectrum of the form $S_{\Delta\theta}(\omega) = \alpha/\omega + \beta$, where β is the additive white noise component that would be equal to half [2] of the mean-square noise voltage relative to mean-square signal (carrier) voltage (see Figure 3.13), $2kT/P_S$ with k being the Boltzmann constant, T temperature, and P_S the signal power. However, in practice typical phase noise values are quite larger than this prediction because there are other noise sources (such as the amplifier) besides tank loss. To account for this discrepancy, Leeson's model introduces an "effective noise figure" F for the oscillator to make $\beta = 2FkT/P_S$. The second component α/ω is assumed to be result of parameter variations and its $1/\omega$ dependence is based on observations. Usually this is attributed to the $1/f$ noise of the active elements present in the energy restoring block (amplifier).

---

[2]By the equipartition theorem of thermodynamics, amplitude and phase noise are equal in equilibrium and the amplitude limiting mechanism in oscillators removes half the noise in amplitude

In this model α is a pure fitting parameter determined by the level of $1/f^3$ variations in the output phase noise. It is also important to note that the "noise figure" F should not be confused with the amplifier noise figure. In reality, F is also a fitting parameter that is determined by the measured spectra rather than a true design variable, thus it becomes difficult to predict the phase noise a priori.

Figure 3.12 illustrates the spectrum of phase noise with three different regimes: a flat portion at frequencies far from the carrier, a $1/f^2$ region shaped by the tank, and a $1/f^3$ portion that is formed by $1/f$ noise. This spectrum can be written in a compact form:

$$S_\phi = \frac{2FkT}{P_{sig}} \left[1 + \left(\frac{\omega_o}{2Q\omega} \right)^2 \right] \left(1 + \frac{\omega_{1/f^3}}{\omega} \right) \tag{3.63}$$

where the parameter α is eliminated to use $2FkT/P_{sig}$ as a common factor, and instead ω_{1/f^3} is used. Again, the new variable ω_{1/f^3} is a fitting parameter and does not necessarily coincide with the $1/f$ corner of device/amplifier noise.

Although the Leeson's equation is very intuitive and simple to use, it does not provide much insight for reducing the phase noise beyond increase P_{sig} and increase Q of the tank circuit. The factor F can have significant contribution to the phase noise and yet it is not fully clear what it depends on and what are the ways to reduce it.

Despite these limitations, Leeson model has been used for OMO phase noise modeling [35],[4],[36] to identify the observed phase noise behavior similar to electronic oscillators as well as general trends with the signal power and tank Q. Since an OMO embodies two resonators (an optical and a mechanical), initially the strategies to improve performance focused on increasing both Q_o and Q_m, but understanding that it is the mechanical tank that acts as the frequency selective element led to focusing efforts on to increasing the Q_m for better phase noise. In this regard, Leeson model has still been useful as a guide for reducing OMO phase noise, but it falls short on providing design guidelines for other parameters such as Q_o.

In the next section we will develop a phase noise model for OMOs, specifically for the high performance ones that are typically operating in the USR regime.

3.7.2   OMO Phase Noise Model

There have been previous studies to model phase noise in OMOs where one approach has been to use Leeson model with modifications [37] to include more OMO parameters. Although this approach shows some agreement between the model and (a particular) data, it still lacks a rigorous treatment of noise sources and processes in phase noise conversion, as well as a complete discussion of OMO parameters in determining the phase noise. A second approach is found to have more rigorous treatment of noise sources/processes though the phase noise components are expressed using lengthy equations unlike the closed-form expression of Leeson model [38],[39]. This makes it quite difficult to gain intuitive design

strategies for practical OMO design, and in some cases even the model fit is questionable [38].
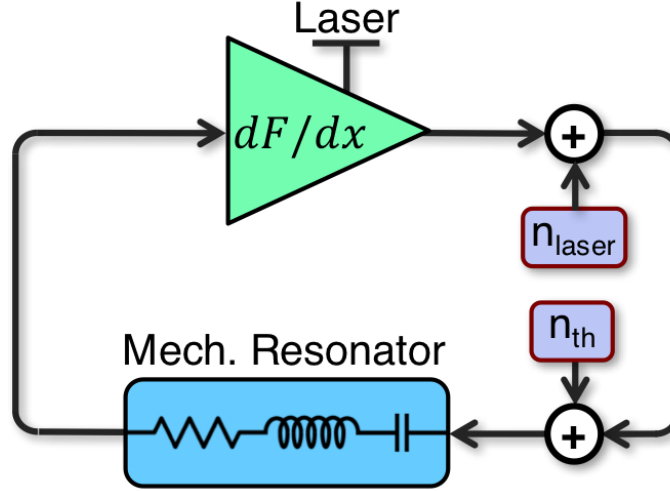
Figure 3.14: OMO oscillator loop with additional noise inputs to facilitate phase noise modeling.

It is therefore desirable to derive a comprehensive yet intuitive phase noise model that can truly be a designer's tool for low phase noise OMO design. Here, we will leverage the engineering model of Section 3.5.2 for OMO as it allows an easy treatment of noise using transfer functions, and include noise sources as inputs entering the system that eventually convert to phase noise. Figure 3.14 shows the oscillator loop with two noise sources: n_{th} being the (mechanical) thermal noise (also referred sometimes as Brownian noise) associated with the resonator (tank) losses and n_{laser} being the noise associated with the amplifier component. Since the amplifier is driven by a laser, the primary source of this component is the laser noise. Note that although the noise inputs are essentially entering to the same node of the loop, it is still preferred to keep them as separate noise sources since in some cases one can dominate the other (as will be seen). Also, it is always possible to refer the noise sources to the input or output of a component and hence the noise sources would not necessarily enter to the same node.

Let us first start by deriving the noise spectrum of displacement at the output of the resonator component using the input noise spectra S_{th} and S_{laser}. Use of displacement noise spectrum allows easy conversion to phase noise spectrum at the output of the OMO where the signal is the RF-modulated laser field. With S_x being the displacement noise spectrum, and β being the (mechanical) resonator transfer function, the relationship between S_x, S_{th}, and S_{laser} is

$$S_x = \frac{|\beta|^2}{|1 - A\beta|^2}(S_{th} + S_{laser}) \tag{3.64}$$

which merely follows from the noise transformation around the loop

$$(n_x A + n_{th} + n_{laser})\beta = n_x \tag{3.65}$$

With the definitions of β and A from Section 3.5.2, it is straightforward to derive the noise shaping term in (3.64). First, the factor $1 - A\beta$ is simply equal to

$$1 - A\beta = 1 + \frac{k_{om} + i\omega\Gamma_{om}m_{eff}}{m_{eff}\left(\omega_m^2 - \omega^2 + i\omega\Gamma_m\right)} \approx \frac{\omega_{osc}^2 - \omega^2}{\omega_m^2 - \omega^2 + i\omega\Gamma_m} \tag{3.66}$$

where the approximation $\Gamma_m + \Gamma_{om} = 0$ is used, which is valid for the oscillator steady state. Multiplying with β and taking the magnitude square yields

$$\frac{|\beta|^2}{|1 - A\beta|^2} = \frac{1}{m_{eff}^2(\omega_{osc}^2 - \omega^2)^2} \tag{3.67}$$

Equation (3.67) is merely a frequency shaping function that has $1/f^2$ dependence due to filtering action of the resonator in the feedback loop, as expected.

Now, we turn our attention to the noise densities S_{th} and S_{laser} that are filtered by the above expression. The spectral density of thermal noise, S_{th}, entering the system is simply

$$S_{th} = 4k_B T\Gamma_m m_{eff} \tag{3.68}$$

where k_B is the Boltzmann constant and T is the absolute temperature.

Laser noise entering the oscillator loop can also have several components but here we assume the dominant sources are laser relative intensity noise (RIN) and laser frequency noise. Since small signal approximation is valid for noise components, derivative of the force (Equation 3.19) with respect to laser power and detuning would relate the RIN and laser frequency noise to the noise entering as a force input, leading to

$$S_{laser} = S_f^{laser}\left(\frac{32P_{in}\kappa_{ex}\Delta g_{om}}{\omega_o(\kappa^2 + 4\Delta^2)}\right)^2 + S_{P_{in}}\left(\frac{4\kappa_{ex}g_{om}}{\omega_o(\kappa^2 + 4\Delta^2)}\right)^2 \tag{3.69}$$

assuming the noise sources are uncorrelated. The actual oscillator output is the modulated optical power at the device output and would have two noise components: input laser noise directly reaching the output and oscillator displacement fluctuations creating unwanted optical modulation. The output noise can be derived from the optical transmission

$$\begin{aligned}
N_{P_{out}} &= \frac{dP_{out}}{dx}N_x + \frac{dP_{out}}{dP_{in}}N_{P_{in}} \\
&= \frac{32P_{in}\kappa_{ex}\kappa_i\bar{\Delta}g_{om}}{(\kappa^2 + 4\bar{\Delta}^2)^2}N_x + \frac{4\bar{\Delta}^2 + (\kappa - 2\kappa_{ex})^2}{\kappa^2 + 4\bar{\Delta}^2}N_{P_{in}}
\end{aligned} \tag{3.70}$$

Using the previous relations $\bar{\Delta} = \kappa/2\sqrt{3}$ and $\kappa_{ex} = \kappa/4$ yields

$$S_{P_{out}} = \left(\frac{81}{64\sqrt{3}}\frac{Q_o}{R}P_{in}\right)^2 S_x + \left(\frac{7}{16}\right)^2 S_{P_{in}} \tag{3.71}$$
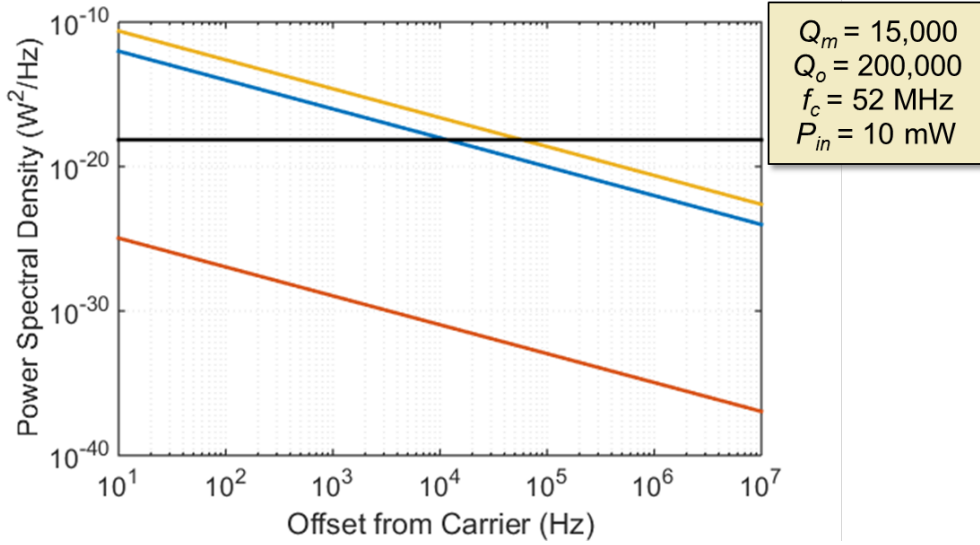
Figure 3.15: Power spectral density of the various phase noise components due to laser frequency noise (red), laser relative intensity noise (blue), and thermal noise (yellow) contributing to S_x and flat noise due to relative intensity noise reaching the output (black). Thermal noise is the dominant component in the $1/f^2$ region. Design values used in calculations are given in the inset.

Figure 3.15 shows different components of the output noise spectrum of an OMO with device parameters indicated in the figure. The plots assume a laser frequency noise that is twice the laser linewidth with a value of 50 kHz, and a laser RIN of -130 dB. The thermal noise dominates the noise in the oscillator spectrum as also predicted by earlier studies [40],[16]. In this case, the output noise spectrum is approximately

$$S_{P_{out}} = \frac{4k_B T \Gamma_m}{m_{eff}} \frac{1}{8} \left(\frac{P_{in} Q_o}{\omega_{osc} R} \right)^2 \left(\frac{1}{\Delta\omega} \right)^2 + \left(\frac{7}{16} \right)^2 S_{P_{in}} \tag{3.72}$$

from which the output phase noise spectral density can be derived by dividing to square of the signal power [34]:

$$S_{\phi_{out}} = \frac{4k_B T \omega_m}{m_{eff} Q_m} \frac{1}{8} \left(\frac{P_{in} Q_o}{P_{sig} \omega_{osc} R} \right)^2 \left(\frac{1}{\Delta\omega} \right)^2 + \frac{S_{P_{in}}}{P_{sig}} \left(\frac{7}{16} \right)^2 \tag{3.73}$$

and finally the single-sided phase noise spectrum as a function of frequency offset from the carrier is defined as

$$\mathcal{L}(f) = 10 \log_{10} \left(\frac{S_{\phi_{out}}}{2} \right) \tag{3.74}$$

Figure 3.16 plots the OMO phase noise vs input power at 1 kHz and 1 MHz offset from the carrier for several Q_o and Q_m values. Phase noise at 1 kHz offset improves with higher
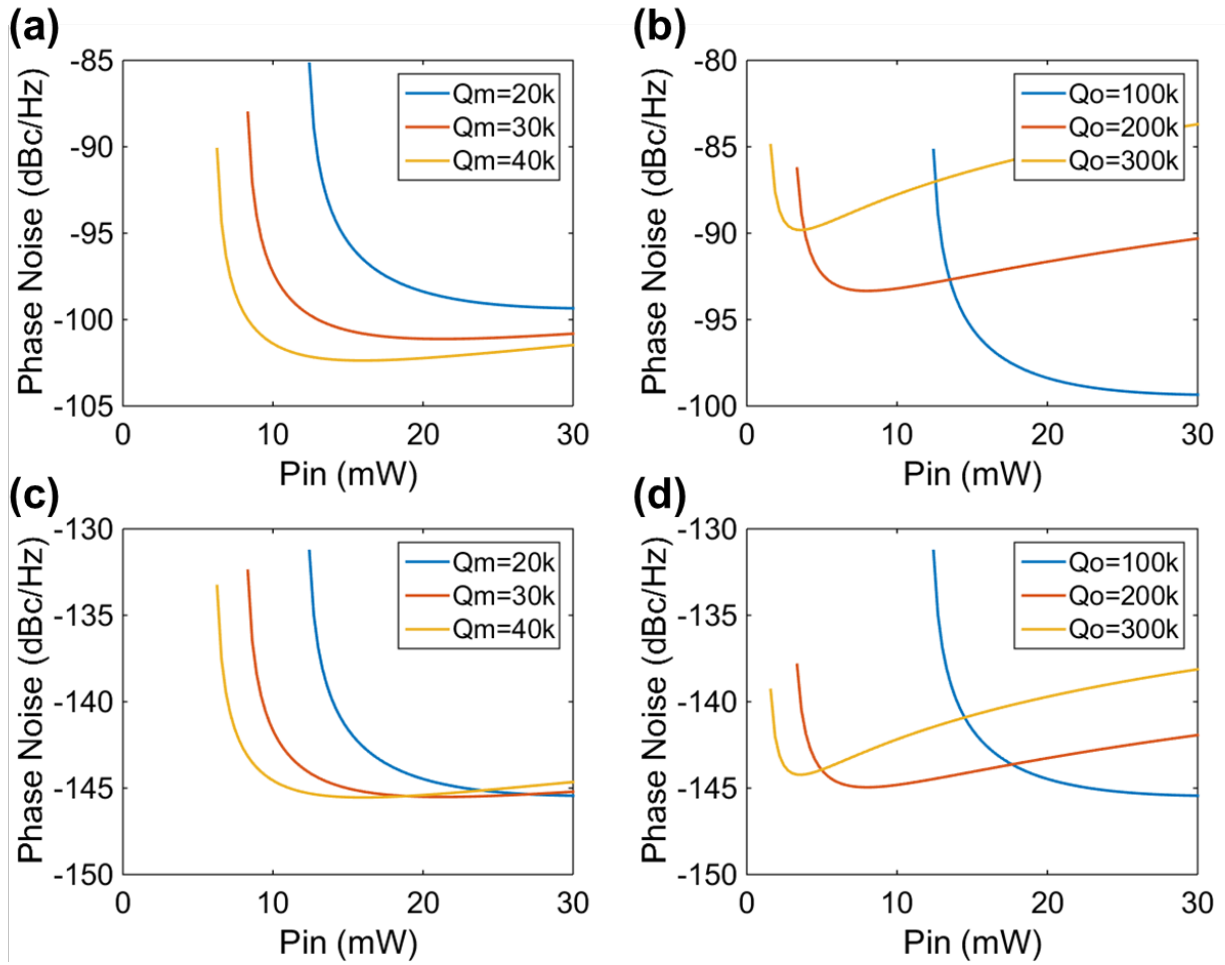
Figure 3.16: Effect of Q_m and Q_o on phase noise at close-to-carrier (a-b) and far-from-carrier (c-d) offsets. Higher Q_m reduces close-to-carrier noise while also reducing the required input power for both close-to-carrier and far-from-carrier offsets. Lower Q_o achieves lower close-to-carrier noise but at the expense of increased input power.

Q_m and lower Q_o, although lower Q_o requires larger power to achieve such low-noise. Higher Q_m also reduces the required input power to achieve low-noise so it is always desirable. At 1 MHz, phase noise reduction with a lower Q_o is marginal at the expanse of higher power, and higher Q_m again helps with the power but the lowest achievable noise floor stays the same.

Although Equation (3.73) outlines the phase noise dependence on device parameters, the signal power is still a function of them, so the exact phase noise dependence on Q_m and Q_o is not explicitly known. However, for small oscillation amplitudes, signal power can be approximated as

$$P_{sig} = \frac{81}{64\sqrt{3}} \frac{Q_o}{R} P_{in} x_{osc} \tag{3.75}$$

In this case the expression for output noise spectrum becomes

$$S_{\phi_{out}} = \frac{k_B T \omega_m}{m_{eff} Q_m} \left(\frac{1}{x_{osc}\omega_{osc}}\right)^2 \left(\frac{1}{\Delta\omega}\right)^2 + \frac{1}{10} \frac{R^2 N_{RIN}}{Q_o^2 x_{osc}^2} \tag{3.76}$$

where N_{RIN} is the RIN of the laser such that $S_{P_{in}} = P_{in}^2 N_{RIN}$. Realizing that $m_{eff}(x_{osc}\omega_{osc})^2$ is equal to twice the total mechanical energy stored in the resonator, E_S, the expression for the $1/f^2$ noise spectral density reduces to

$$S_{\phi_{out}}^{1/f^2} = \frac{k_B T \omega_m}{8\pi^2 E_S} \frac{1}{Q_m} \left(\frac{1}{\Delta f}\right)^2 \tag{3.77}$$

which is in excellent agreement with the expression found for the oscillation linewidth in the case of a thermally limited OMO in reference [16]:

$$\Gamma_{osc} = \frac{k_B T}{2 E_S} \Gamma_m \tag{3.78}$$

where the two are related by

$$\Gamma_{osc} = 4\pi^2 (\Delta f)^2 \frac{S_{\phi_{out}}^{1/f^2}}{2} \tag{3.79}$$

Equation (3.76) suggests that large effective mass and oscillation amplitude reduces the phase noise. High Q_m improves the phase noise in two ways: it filters out the noise and increases the oscillation amplitude, which in turn reduces the phase noise. Although the flat-noise spectrum has an inverse-quadratic dependence on Q_o, large Q_o limits the oscillation amplitude as well, resulting in near-constant minimum achievable noise floor.

3.8   Outlook

Phase noise model of Section 3.7.2 underscores the importance of mechanical quality factor for lowering the phase noise of an OMO. This motivates a focus to increase Q_m of the resonator without degrading other key parameters. Work in [4] is a good example where OMO's Q_m were increased merely by removing the air damping in vacuum, yielding better phase noise performance as expected. While continuing the efforts to achieve higher Q_m, for example with a new OMO design, Q_o is likely the most important parameter to watch for, since usually Q_m and Q_o are coupled through the resonator structure and material properties. For example, high-Qm MEMS resonators would use polysilicon or diamond thin films to achieve Q_m's >40,000 at the frequency range >10 MHz as presented in Chapter 2, but these materials are not suited for an OMO because of high optical losses they would have. As we have seen in this chapter, even a small drop in Q_o can significantly increase the threshold power for operation. A minimally intrusive OMO design with increased Q_m seems critical for further improvement in phase noise. Chapter 4 will introduce such designs and their performance to demonstrate best-in-class OMO's that validate the predictions and conclusions we have arrived in this chapter.

Chapter 4

Integrated MEMS Optomechanical Oscillators

We have seen in Chapter 3 that best OMO performance requires optimal mechanical and optical designs. Chapter 2 introduced mechanical and optical microresonator technologies with materials and designs for optimal performance in these individual domains. It is highly desirable to have the best of both worlds, possibly by integrating high performance MEMS resonators and optical resonators in a composite OMO. In this chapter, we will use this approach to introduce new OMO designs that allow decoupling of optical and mechanical designs and hence simultaneous optimization of Q_m and Q_o for best oscillator performance.

As introduced in Chapter 1, one of the most benefited application from a high performance, low power OMO would be a CSAC with a much lower power consumption as a result of using an OMO as its oscillator. In this implementation, an OMO harmonic at $\sim$3.4 GHz would be used to interrogate the Rb vapor cell, and the error voltage produced at the cell output would be used to correct the frequency error of OMO. As such, the OMO must have ability to lock to an external reference with its $\sim$3.4 GHz harmonic, low phase noise and low power, and a frequency tuning mechanism. Also, an electrical output from the OMO would allow direct access to the lower frequency (MHz) fundamental oscillator output without extra filtering (that would be required at the photodetector output), which would additionally be free of photodetector noise. These requirements on OMO can be translated into a checklist that must be accomplished for a successful low power CSAC implementation:

- High frequency harmonics (combs) up to $\sim$3.4 GHz

- Have simultaneous high-Q_o and high-Q_m (for low power and low phase noise)

- Voltage control of frequency for easy tuning

- Electrical output

- Higher harmonic locking

Among the items in this checklist, high frequency comb generation is already achievable with previous OMO designs. Thus, our focus is to achieve simultaneous high-Q_o and high-Q_m, as well as having a voltage controlled frequency tuning mechanism that should enable using a higher-order harmonic for locking to an external reference. Chapter 2 already showed us that capacitively coupled MEMS resonators fulfill high-Q_m and voltage controlled frequency tuning requirements, but fall short on providing high-Q_o mainly because of the high (optical) loss materials used in these resonators. Similarly, high-Q_o resonators are generally dielectric or other non-conductive materials that do not have electromechanical coupling (necessary for voltage controlled tuning and electrical output), as well as show limited Q_m compared to MEMS resonators. All in all, material limitation on performance is the key problem that needs to be addressed.

To this end, an integrated MEMS-OMO approach combining more than one material using careful mechanical circuit design techniques in the resonator structure can eliminate the material limitation problem. OMOs presented in this chapter use this approach and achieve best-in-class performance, paving the way for a low power CSAC application as well as a stable on-chip microwave source with power-efficient high frequency harmonics. The crux behind the mechanical design for high-Q_m is a technique dubbed Q-boosting, which we will explain in the next section.

4.1 Q-Boosting

Q-boosting is a mechanical circuit-based approach first introduced in [41], where a high-Q_m resonator raises the functional Q_m of a low-Q_m resonator in a mechanically coupled system by sharing its energy while adding relatively no loss. In the work of [41] and [42], combination of high and low-Q_m MEMS resonators in a mechanically coupled array to realize a single resonator function is motivated by achieving simultaneous low impedance and high Q_m with the composite array resonator, which don't come together in a single resonator structure. For example, piezoelectric resonators (such as AlN) attain low impedance as a result of large electromechanical coupling, but they show limited Q_m. On the other hand, capacitively-transduced resonators (such as polysilicon) can achieve much higher Q_m's, but with impedances larger than piezoelectric resonators due to lower electromechanical coupling. In the Q_m-boosted array, AlN resonators are employed in the input-output to provide large electromechanical coupling that results in low impedance. In a way, polysilicon resonators added in between these input-output resonators provide additional mechanical energy to the composite array while adding very little loss compared to AlN, thus total Q_m of the array gets boosted from Q_m of AlN to a higher value, depending on the number of resonators. To illustrate the basic Q_m-boosting argument, we will analyze the case in [41] where n identical size resonators are mechanically coupled by half-wavelength coupling beams connecting each adjacent resonator to one another to force all of them vibrate in phase with equal amplitude, as depicted in Figure 4.1. Since all the resonators are equal in mass and vibrate with equal amplitude and frequency, each stores equal average mechanical energy, but we consider a

(a)

$\lambda_m/2$ coupling beams

(b)

$R_{r,1}$ L_r C_r $R_{r,2}$ L_r C_r $R_{r,3}$ L_r C_r $R_{r,n}$ L_r C_r

$$Q_1 = \omega_m \frac{L_{res}}{R_{r,1}} \qquad Q_2 = \omega_m \frac{L_{res}}{R_{r,2}} \qquad Q_2 = \omega_m \frac{L_{res}}{R_{r,3}}$$

(c) R_{tot} nL_r C_r/n $Q_{array} = \omega_m \dfrac{nL_{res}}{R_{tot}} \approx nQ_{low}$
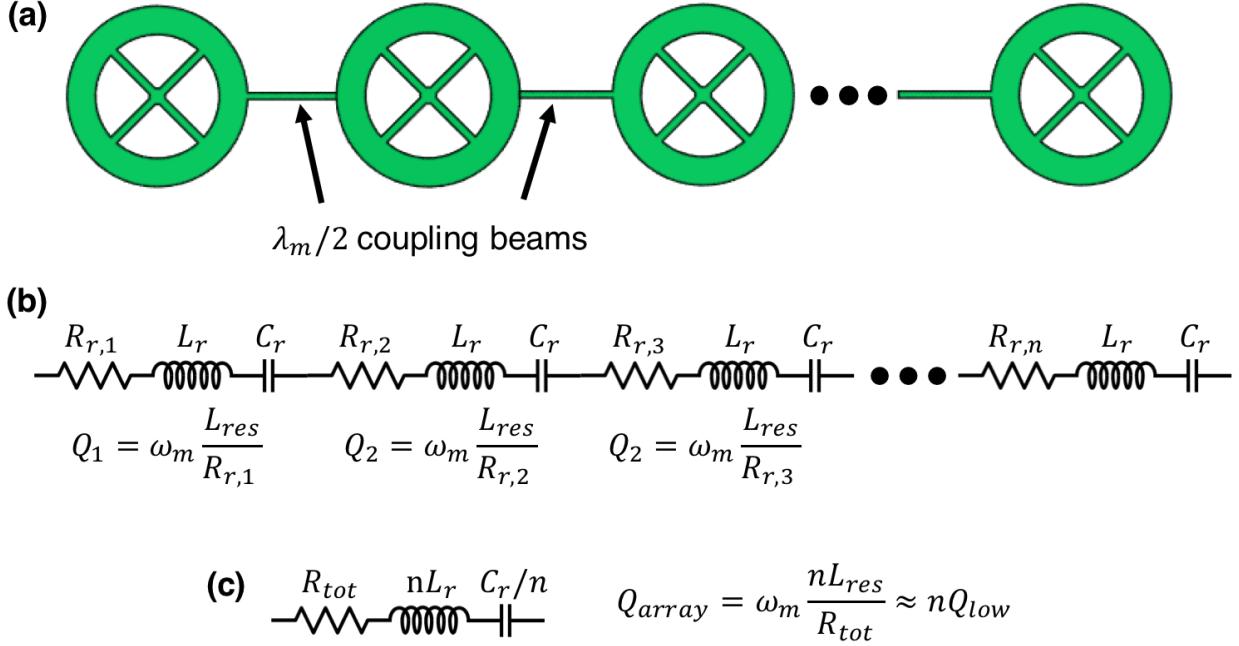
Figure 4.1: (a) MEMS coupled array resonators. $\lambda_m/2$ long coupling beams ensure in-phase motion with equal amplitude between the individual resonators. (b) Equivalent circuit model of the mechanical array in (a), where the entire branch share the same current as ensured by the $\lambda/2$ coupling beams. (c) Condensed equivalent circuit of (b) that has n times larger L of an individual resonator, and a resistance of $R_{tot} = R_1 + R_2 + ... + R_n$. In the case of a dominant low-Q resonator with $R \approx R_{tot}$, composite array's Q becomes $Q_{array} \approx nQ_{low}$.

general case where the energy loss can be different. In this case, total Q_m of the array can be derived from the basic energy definition:

$$Q_{m,tot} = 2\pi \frac{E_{S,tot}}{E_{L,tot}} = 2\pi \frac{\sum\limits_i^n E_{S_i}}{\sum\limits_i^n E_{L_i}} = 2\pi \frac{n \times E_{S_o}}{\sum\limits_i^n E_{L_i}} = n \times \left(\sum\limits_i^n \frac{E_{L_i}}{2\pi E_{S_o}} \right)^{-1} \tag{4.1}$$

where $E_{S,tot}$ and $E_{L,tot}$ are the total average stored energy and the total energy lost per cycle in the entire array, $E_{S_o} = E_{S_1} = E_{S_2} = ... = E_{S_n}$ is the average stored energy in each resonator. By definition, the fraction $E_{L_i}/(2\pi E_{S_o})$ is equal to individual Q_m of each resonator. Total array Q_m in terms of individual resonator Q_m is then

$$Q_{m,tot} = n \times \left(\frac{1}{Q_{m_1}} + \frac{1}{Q_{m_2}} + ... + \frac{1}{Q_{m_n}} \right)^{-1} \tag{4.2}$$

In the case where all resonators are identically designed, individual resonator Q_m's are equal, hence $Q_{m,tot} = Q_{m_1} = Q_{m_2} = ... = Q_{m_n}$, as expected. Q-boosting[1] occurs when a low-Q_m resonator is coupled to high-Q_m resonators so that the sum in Equation (4.2) is dominated by the low-Q_m resonator. In the case $Q_{m,low}$ ¡¡ $Q_{m,high}$, the composite array will exhibit a $Q_{m,tot}$ of

$$Q_{m,tot} = n \times \left(\frac{1}{Q_{m,low}} \right)^{-1} = n \times Q_{m,low} \tag{4.3}$$

which is the biggest boost possible. If $Q_{m,low}$ is not so much smaller than $Q_{m,high}$, then the final $Q_{m,tot}$ should follow Equation (4.2) with a $Q_{m,low}$ smaller than $n \times Q_{m,low}$.

The same arguments can also be made by using electrical equivalent circuits of individual resonators, added in series fashion when coupled in an array, as shown in Figure 4.1(b). The exact coupling would actually be through transmission lines representing the coupling beams, but in the case of strong coupling (0-λ_m, $\lambda_m/2$ etc.) the coupling elements can simply be ignored. This picture gives a more intuitive understanding without the energy arguments, where the the total energy loss is simply represented by the total resistance, which is dominated by the low-Q_m resonator. It is also important to note that for Q-boosting the inductor and capacitor (mass and stiffness) values of the resonators need not to be equal, and final $Q_{m,tot}$ will also be proportional to the inductance (mass) of the composite array.

4.1.1 OMO Q_m-Boosting Design Considerations

We have seen that the optimal OMO performance requires simultaneous optimization of Q_m and Q_o. Although it is not feasible to increase Q_m of a good optical material resonator once it is limited by the material loss (assuming that the resonator is already designed optimally for minimal anchor loss), Q-boosting provides a way to increase overall Q_m of an OMO structure by coupling its low-Q_m / high-Q_o resonator to a high-Q_m resonator, where the two shares the vibrational energy while the optical field is still stored in the high-Q_o resonator. Figure 4.2 shows an example placement of the resonators, where the high-Q_o resonator is a silicon nitride and the high-Q_m is a polysilicon ring, reminiscent of the AlN-polysilicon resonator array proposed in [41] that has AlN for large electromechanical coupling and polysilicon for high-Q_m. Although this array design would boost the Q_m of the silicon nitride ring, it is still not optimal because the beam coupling would degrade optical-Q by introducing a scatter defect at the silicon nitride ring outer edge, where the optical field is confined. So this design would be a compromise between Q_m and Q_o, which is not acceptable for our case.

---

[1]To avoid confusion, it should be emphasized that the term Q-boosting refers to the boost of low-Q_m from its value to a higher value with the use of coupling to high-Q_m resonators. It should be kept in mind that the low-Q_m resonator is the resonator that is employed due some other attractive quality, such as larger electromechanical coupling in the case of AlN resonator, but lacking the required Q_m. With coupling, the array shows both large electromechanical coupling and higher-Q_m than Q_m of AlN
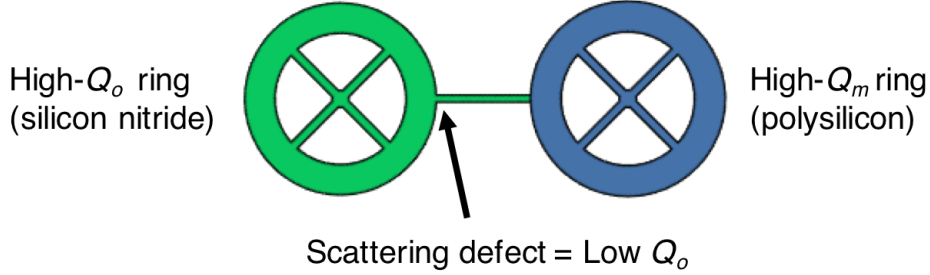
Figure 4.2: Laterally-coupled high-Q_o (but low-Q_m) and high-Q_m resonators. Coupling beam at the outer edge of the high-Q_o ring introduces a scattering defect for the optical field, reducing the Q_o.

It is necessary to find the optimal design that can yield both high Q_o and Q_m at the same time.

This chapter introduces two multi-material OMO designs that allow simultaneous optimization of Q_m and Q_o without any compromise. Figure 4.3 introduces the designs with a more general consideration where the choice of high-Q_o and high-Q_m materials is up to the designer, as long as they can be integrated in a single fabrication process. Here, the resonator placement, mechanical coupling, electrode placement, and electrical routing all have an important role for optimal design, which we will explain further in the coming sections.

4.2 Coplanar Double-Ring OMO

The first multi-material OMO design we will present in this thesis is the concentric, coplanar double-ring design which couples a high-Q_o (but low-Q_m) ring through its inner edge to a high-Q_m (but low-Q_o) and electrically conductive ring for Q_m-boosting and electromechanical coupling. In particular, we will demonstrate Q_m-boosted OMOs using silicon nitride as its high-Q_o ring material and polysilicon as the high-Q_m electrically conductive ring material, with best-to-date phase noise performance enabled by the boosted-Q_m.

4.2.1 Device Structure and Operation

Mechanical Design

The coplanar ring OMO, summarized in perspective-view and cross-section in Figure 4.4, comprises a high-Q_m polysilicon inner ring physically attached at its outer edge to a concentric high-Q_o (but comparatively low Q_m) silicon nitride ring. Spokes attached to the inner edges of the polysilicon ring extend radially inwards to a common central anchor and serve to support the entire double-ring device in a completely balanced fashion, where inward forces
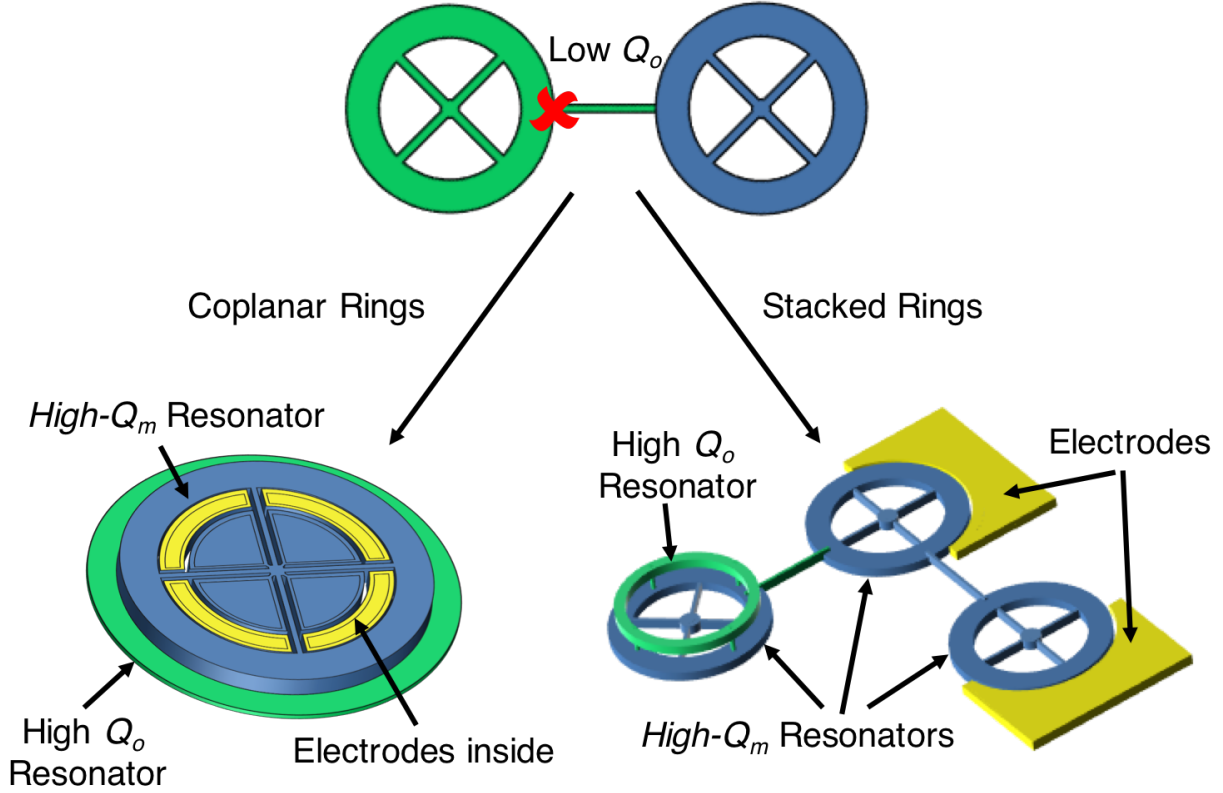
Figure 4.3: Multi-material OMO designs (lower panel) eliminate the scattering defect introduced by the lateral coupling beam in the ordinary coupled-array design (upper panel), preserving the high-Q_o of the optical cavity (green ring) while coupling it to high-Q_m, electrically conductive MEMS resonator(s) (blue).

along the spokes are met with equal and opposite ones, canceling energy leakage from the spokes to the substrate. Polysilicon electrodes inside the polysilicon ring overlap its inner edge to form capacitive gaps that then allow electrical interrogation and control (in addition to optical).

Because the optical mode supported by the silicon nitride ring structure couples most strongly to the fundamental (breathing) contour mechanical mode, radiation pressure force built in the device excites this mechanical mode into oscillation. Radially symmetric contour mode ensures that the inner polysilicon ring experiences equal radial force along its perimeter, where it couples to the silicon nitride ring. As a result, both rings vibrate in breathing mode in a strongly coupled fashion (similar to 0-λ_m beam coupling [43],[44]) such that the displacement of the two rings are in-phase. This allows using equivalent circuits to conveniently model the composite structure as a coupled mechanical system.
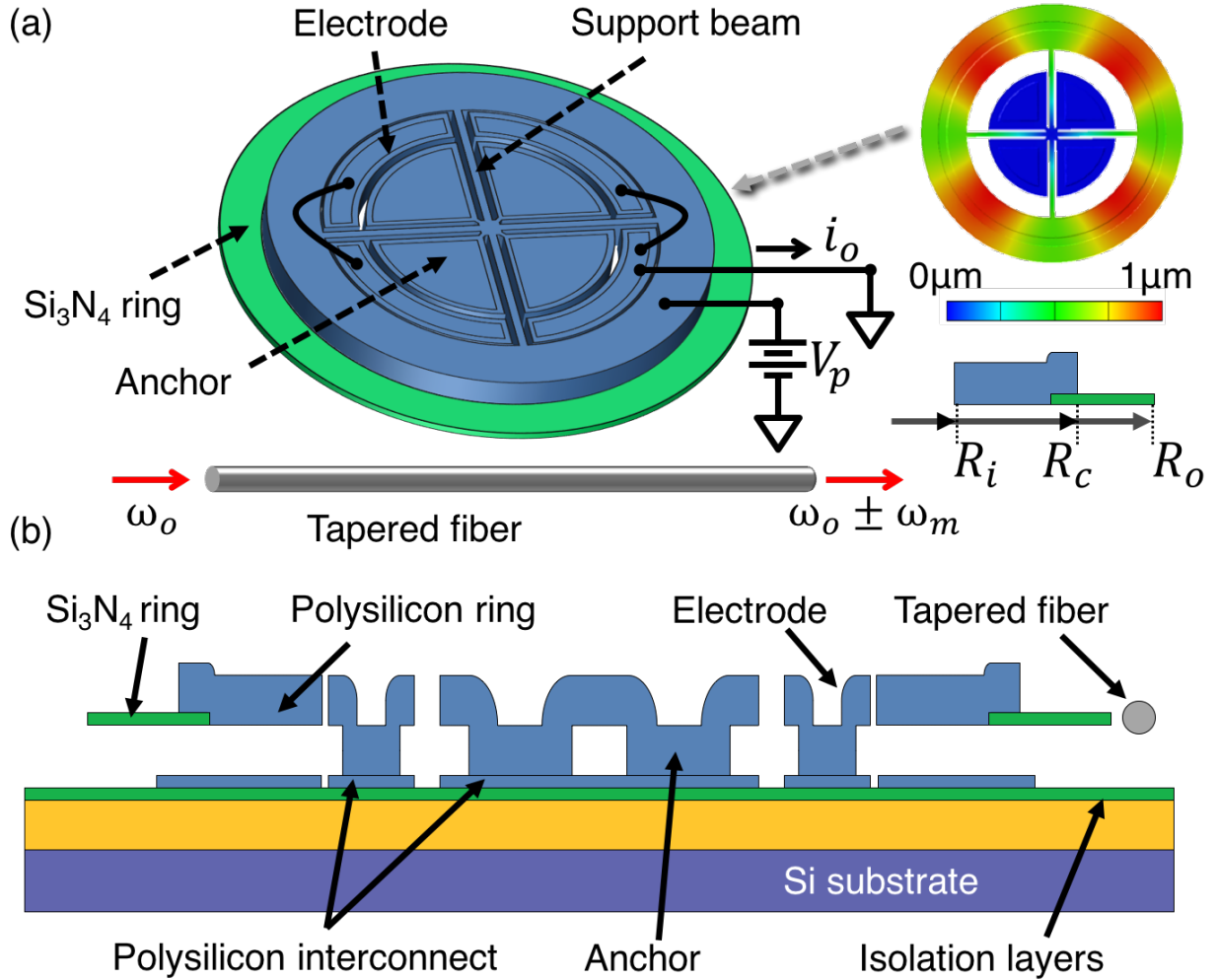
Figure 4.4: (a) Perspective-view and (b) cross-sectional schematics of the Q-boosted coplanar double-ring OMO. Here, the polysilicon inner ring is mechanically coupled at its outer edge to a concentric high-Q_o silicon nitride ring. A tapered fiber provides optical coupling, while polysilicon electrodes inside the ring enable frequency tuning and electrical input-output.

In the coupled equivalent model each ring is represented by an equivalent circuit, thus it is not necessary to derive mechanical design equations for the entire composite structure. Instead, we will design and model each ring separately and insert the models to the coupled resonator model. For a single ring resonator, first step in mechanical modeling is to find the resonance frequency by solving the transcendental frequency equations

$$\begin{aligned}
&[J_1(pr_i)\sigma - J_1(pr_i) + r_i p J_0(pr_i)] \left[Y_1(pr_o)\sigma - Y_1(pr_o) + r_o p Y_0(pr_o)\right] \\
&-[Y_1(pr_i)\sigma - Y_1(pr_i) + r_i p Y_0(pr_i)][J_1(pr_o)\sigma - J_1(pr_o) + r_o p J_0(pr_o)] = 0
\end{aligned} \tag{4.4}$$

Table 4.1: Several example OMO designs with calculated and measured mechanical resonance frequencies.

	Design 1	Design 2	Design 3	Design 4
R_i (μm)	20	20	30	15
R_c (μm)	30	30	40	20
R_o (μm)	36.5	38	49	26.5
m_p (ng)	7.759	7.759	10.699	2.675
m_n (ng)	1.607	2.004	2.974	1.102
$f_{m,p}$ (MHz)	52.06	52.06	36.96	73.92
$f_{m,n}$ (MHz)	43.12	42.22	32.22	61.86
f_{calc} (MHz)	50.55	50.19	35.97	70.61
f_{meas} (MHz)	52.08	51.94	37.01	74.02

$$f_m = \frac{p}{2\pi}\sqrt{\frac{E}{\rho(1-\sigma^2)}} \tag{4.5}$$

that govern the mechanical resonance frequency for all radially symmetric contour modes. Here, r_i and r_o are the dimensions of inner and outer radii of the ring, respectively, J_n is the Bessel functions of the first kind, Y_n is the Bessel functions of the second kind, ρ is the density, ν is the Poisson's ratio, and E is the Young's modulus of the resonator material. The breathing mode corresponds to $p = 1$, where p is named frequency parameter.

Once the resonance frequency for a given mode is known, mechanical lumped equivalent model follows from the definitions of effective mass, stiffness, and damping:

$$m_{eff} = \frac{E_S}{\frac{1}{2}V^2(r)} = \frac{\frac{1}{2}\int_0^{2\pi}\int_{R_{in}}^{R_{out}}\omega_m x(r)dm}{\frac{1}{2}(\omega_m x(r))^2} \tag{4.6}$$

$$k_{eff} = \omega_m^2 m_{eff} \tag{4.7}$$

$$b_{eff} = \frac{\omega_m m_{eff}}{Q_m} \tag{4.8}$$

where E_S is the total kinetic energy stored in the structure, ω_m is the mechanical (radial) resonance frequency, and $x(r)$ is the displacement amplitude at a given radius. As such, lumped element values are specific to a chosen location on the structure. Three important radial locations identified on the inset of Figure 4.4 as R_i, R_c and R_o correspond to the polysilicon ring's inner radius, coupling location of the two rings, and silicon nitride ring's outer radius, respectively.

After individual equivalent circuit modeling of polysilicon and silicon nitride rings the next step is to represent them in the composite structure with appropriate mechanical coupling. Electrical transformers allow appropriately carrying current and voltage (velocity and
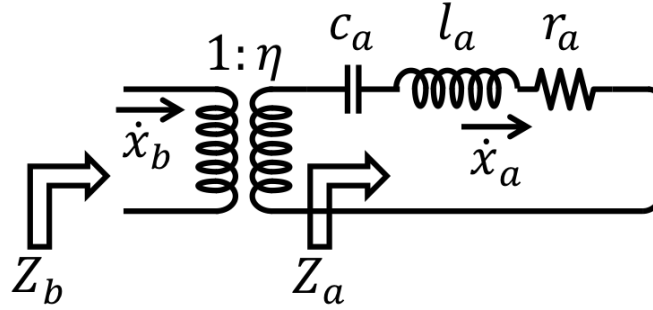
Figure 4.5: Impedance transform from point a to point b using a transformer. Transformer turns ratio ensures that the velocity and force in each branch are carried appropriately. In the above configuration impedance scales as $Z_b = Z_a/\eta^2$.

force) values at the equivalent circuit location to other locations so that the circuit branches have equal current and equal voltage at the coupling point. Briefly, with reference to Figure 4.5, a circuit branch gets transformed from point a to point b via turns ratio $\eta = \dot{x}_b/\dot{x}_a$ so that the equivalent circuit elements l (m_{eff}), c $(1/k_{eff})$, and r (b_{eff}) at point b become

$$l_b = m_{eff,b} = \frac{1}{\eta^2} m_{eff,a} = \frac{1}{\eta^2} l_a$$

$$c_b = \frac{1}{k_{eff,b}} = \frac{1}{k_{eff,a} 1/\eta^2} = \eta^2 c_a \qquad (4.9)$$

$$r_b = b_{eff,b} = \frac{1}{\eta^2} b_{eff,a} = \frac{1}{\eta^2} r_a$$

as dictated by conservation of energy and can also be derived directly from Equations (4.6-4.8).

Figure 4.6(a) presents the equivalent electro-mechanical model of the composite double-ring structure where the electrical analogues l, c, and r represent the mechanical (lumped) elements m, k, and b, respectively. Here, the transformers with coupling coefficient η_e represent the electro-mechanical coupling between the polysilicon electrodes and the polysilicon ring that form parallel-plate capacitors. Although there are four electrodes, two of each are electrically connected to realize an input and an output port, so the equivalent circuit shows the combined electrode configuration at each port. Voltage across the ports generate a force at the inner surface of the polysilicon ring, so the tank circuit values l_p, c_p, and r_p represent the polysilicon ring's equivalent circuit at R_i. Similarly, l_n, c_n, and r_n represent the silicon nitride ring's equivalent circuit at R_o where the optical force is generated.

Note that the choice of location on the ring for equivalent circuit representation is arbitrary, and each radial location would yield a different equivalent circuit representation. We could chose the coupling location R_c for both equivalent circuits to easily link the two circuits. In that case the two r-l-c branches would appear side-by-side, since they would
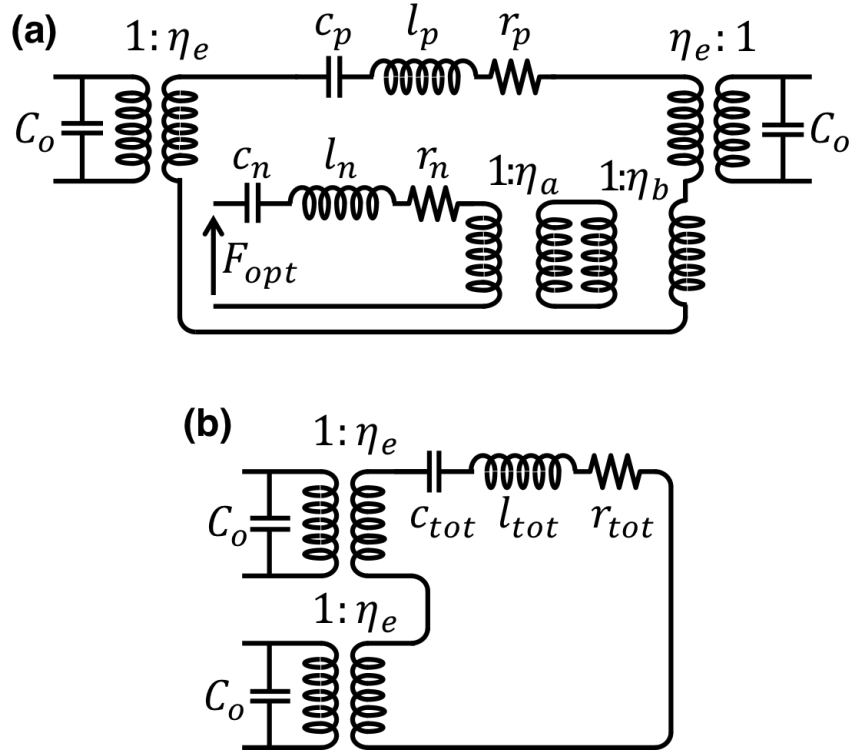
Figure 4.6: Electrical domain equivalent circuit of the Q-boosted OMO. (a) Full circuit with polysilicon and silicon nitride resonator values explicitly shown. (b) Condensed circuit after removal of velocity transformers showing the final resonant circuit that governs the overall mechanical resonant frequency.

share the same velocity/mesh current at that location. However, our choice of R_i and R_o allows depicting electro-mechanical and optical forces directly on respective branches, and the two circuits can still be linked by a mere velocity transformation. This transformation is done by a transformer in the electrical domain, where the turns ratio is equal to the ratio of velocity on each side of the transformer. In this case, the silicon-nitride ring's equivalent circuit is transformed from R_o to R_c via turns ratio

$$\eta_a = \frac{\dot{x}_o}{\dot{x}_c} \tag{4.10}$$

and the polysilicon ring's equivalent circuit is transformed from R_i to R_c via turns ratio

$$\eta_b = \frac{\dot{x}_c}{\dot{x}_i} \tag{4.11}$$

where, at R_c, both rings experience the same velocity/displacement.

Figure 4.6(b) presents a condensed version of the equivalent circuit of Figure 4.6(a) after the velocity transformations. Since the two tank circuits at R_c result in series configuration,

the effective mass, stiffness and damping values of individual rings just add at this location. In this case, resonance frequency of the composite structure becomes:

$$f_m = \frac{1}{2\pi}\sqrt{\frac{k_{eff}}{m_{eff}}} = \frac{1}{2\pi}\sqrt{\frac{\omega_{m,n}^2 m_n + \omega_{m,p}^2 m_p}{m_n + m_p}} \qquad (4.12)$$
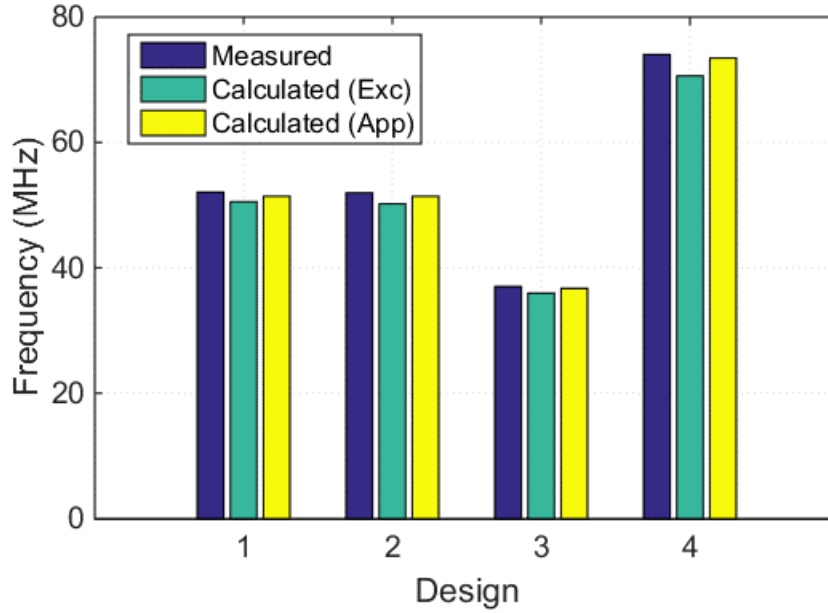
Figure 4.7: Comparison of measured (blue) mechanical resonance frequency of OMO's given in Table 4.1 vs calculated using Equation (4.12) (green) and Equation (4.13) (yellow). The approximate analysis matches measured frequencies fairly well, proving the usefulness of approximate formula for OMO design.

In the actual device structure, the polysilicon ring is wider than the silicon nitride ring since a high-Q_m design needs minimal silicon nitride to minimize the mechanical loss. Also, thicker (2 µm) polysilicon ring increases the electromechanical coupling, while silicon nitride thickness is limited to typically below 500 nm because of the high tensile stress in the deposited film. The overall result is that the polysilicon ring is physically much larger than the silicon nitride ring. As such, the polysilicon ring dominates the total effective mass m_{eff} of the composite structure, so it ultimately dictates the coplanar ring OMO's mechanical resonance frequency to first order (as will be seen). In this case, the first eigen-frequency solution of the transcendental equations (4.4) for the polysilicon ring will yield a close result to the full-blown analysis that requires calculating the equivalent circuit values. However, this approach still needs numerical methods that lacks an intuitive approach for designing the OMO frequency. Instead, designers can use an approximate expression for the breathing mode ring frequency [ref]:

$$f_m = \frac{1}{2\pi}\sqrt{\frac{E}{\rho}}\frac{2}{R_{in} + R_{out}} \tag{4.13}$$

To gauge the efficacy of Equation (4.12) and (4.13), Figure 4.7 plots the measured mechanical oscillation frequencies of several OMO designs of Table 4.1 together with the calculated values from the design Equations (4.12) and (4.13). For each design, the predicted values follow the measurements fairly well.

Optical Design and Operation

Silicon nitride ring surrounding the structure serves as the optical resonator that supports Whispering Gallery Mode (WGM) optical resonances. As explained in Chapter 2, WGM resonances confine the light field primarily to the outer edge of the resonator and the field circulates with successive reflections off the cavity outer periphery in a repeating circular trajectory. Here, the modes of interest have mode numbers $l=1$ (in z) since the silicon nitride cavity is thin ($h << \lambda$) and only supports one mode in the z-direction, and $k=1$ (in r) since it is the most confined radial mode. Therefore, the resonant modes $1, 1, m$ have wavelengths

$$\lambda_o = \frac{2\pi R_o n_{eff}}{m} \tag{4.14}$$

as a result of the periodic boundary condition in the azimuthal direction, which emphasizes that the resonance condition arise when an integer number of effective wavelengths fit around the ring circumference.

These WGM resonances of the coplanar ring structure will have similar Q_o's to that of a stand-alone silicon nitride ring cavity as long as the optical field profile does not overlap with the scatter and absorption-prone lossy polysilicon ring. This dictates a minimum distance between the silicon nitride-polysilicon attachment interface and the outer edge of the silicon nitride ring to retain the high-Q_o of the silicon nitride. A conservative design would use a wide silicon nitride ring to make sure the optical mode is well away from the polysilicon interface but this may compromise the overall Q_m since silicon nitride has higher mechanical loss (lower Q_m) compared to polysilicon. To find the minimum silicon nitride width required for high Q_o, the optical field profile of several silicon nitride rings were simulated using an FEA solver, and the minimum width data points were fitted to a design equation (as presented in [45]) in terms of R_c and R_o to yield

$$R_o - 2.1263\ln(R_o) = R_c - 1.2665 \tag{4.15}$$

where R_o and R_c are in microns. As an example, the 52-MHz OMO design with $R_c = 30$ μm requires about 6.4 μm silicon nitride width according to (4.15), with an $R_o > 36.4$ μm. Design 1 of Table 4.1 with $R_c = 30$ μm, and $R_o = 36.5$ μm exhibits $Q_o = 283,370$, which is

on par with or even better than the Q_o's of silicon-nitride-only rings reported before [17],[4], showing that the multi-material design is capable of preserving high-Q_o of the silicon nitride.

To couple light into and out of the silicon-nitride ring cavity, it is possible to use a tapered fiber [46] clamped on a nano-positioning stage for precise control of coupling gap or an integrated waveguide that can provide a robust interface for eliminating lower-frequency vibrations of a clamped fiber. This work uses the former approach to allow varying the coupling gap during measurements.

Electrical Input/Output and Frequency Tuning

Although the multi-material OMO is a stand-alone oscillator that doesn't require external electronic circuitry for operation, it can also be driven electrically–a functionality not available in nonconductive single-material OMO's. This allows electrical modulation of the optical field and voltage controlled tuning of the oscillation frequency. It further provides direct electrical output without the need for a photodetector to isolate the mechanical oscillation.

To enable electrical input/output, four polysilicon electrodes inside the polysilicon ring overlap its inner edge to form parallel plate capacitors that then realize capacitive-gap transducers. The electrodes anchor to underlying polysilicon interconnects that facilitate signal routing and connection to external electronic circuitry.

Obtaining an electrical output from the coplanar ring OMO entails applying a DC bias (V_P) across the conductive polysilicon ring and electrodes. When the radiation pressure drives the ring into oscillation, the ensuing motion modulates the DC-biased output capacitance C_{out} at the resonance frequency, generating displacement currents across this time-varying electrode-to-resonator gap:

$$i_o = V_P \frac{\partial C_{out}}{\partial t} = V_P \frac{\partial C_{out}}{\partial x} \frac{\partial x}{\partial t} \tag{4.16}$$

which can then serve as output signal proportional to displacement or velocity.

The electrodes additionally allow tuning of the OMO's oscillation frequency (such as needed for CSAC application) via DC voltage. The applied voltage V_P generates a force from the resonator to the electrodes given by

$$F_e = \frac{1}{2} \frac{\partial C}{\partial x} V_P^2 \tag{4.17}$$

where

$$\frac{\partial C}{\partial x} = \frac{C_o}{d_o} \left(1 - \frac{x}{d_o}\right)^{-2} \tag{4.18}$$

is the change in electrode-to-resonator capacitance per unit radial displacement of the OMO, C_o is the static electrode-to-resonator overlap capacitance and d_o is the electrode-to-resonator gap spacing. For small displacements, the resonant force acting on the resonator becomes

$$F_e = V_P^2 \frac{C_o}{d_o^2} x \tag{4.19}$$

This force is proportional to and in phase with the resonator displacement, which identifies the term $V_P^2 C_o/d_o^2$ as a stiffness generated via electrical means [47],[48],[49]. Intuitively, the electrical force acts to enhance the displacement since it grows when the resonator gets close to electrode. Thus, the electrical stiffness subtracts from the mechanical stiffness, yielding a voltage dependent mechanical frequency given by

$$f_m = \frac{1}{2\pi} \sqrt{\frac{k_{eff}}{m_{eff}}} = \frac{1}{2\pi} \sqrt{\frac{k_m - k_e}{m_{eff}}} = f_{nom} \sqrt{1 - \frac{V_P^2 C_o}{k_m d_o^2}} \tag{4.20}$$

where f_{nom} is the nominal mechanical frequency under no DC voltage.

It is also important to emphasize that the unique electrode placement of the multi-material OMO is a key design consideration. Although WGM OMO's constructed in single crystal silicon can exhibit electromechanical coupling [21],[35], the lack of an underlying interconnect necessitates electrodes placed around the ring periphery to have large enough area to probe the electrodes. In this case, a second ring is employed for optical coupling, which connects to the electromechanical ring via a coupling beam. The use of a coupling beam, however, introduces a scattering location for the optical field, which then limits the achievable Q_o.

4.2.2 Mechanical Q-Boosting

The key to achieve simultaneous high-Q_m and high-Q_o in the multi-material OMO structure is the Q-boosting concept introduced in Section 4.1. In the multi-material OMO, high-Q_m polysilicon ring raises the functional Q_m of the composite structure from that of silicon nitride-only resonator by sharing its energy while adding relatively no loss. Both the polysilicon and silicon nitride rings supply vibrational energy to the composite structure in proportion to their effective masses (precisely, effective masses at R_c since the velocity of both masses are equal at R_c). Neglecting the loss at the nitride-polysilicon interface and possible change in the structure's anchor loss due to coupling of two materials, the functional $Q_{m,tot}$ of the composite structure can be expressed as

$$Q_{m,tot} = \omega_m \frac{E_S^n + E_S^p}{P_d} \tag{4.21}$$

where P_d is the total dissipated power in the entire composite structure, E_S^n and E_S^p are the mechanical energy stored in the silicon nitride and polysilicon ring, respectively. Substituting

$$E_S^n = \frac{1}{2}m_n V_{R_c}^2$$

$$E_S^p = \frac{1}{2}m_p V_{R_c}^2 \qquad (4.22)$$

$$P_d = \frac{1}{2}(b_n + b_p)V_{R_c}^2$$

we get

$$Q_{m,tot} = \omega_m \frac{m_n + m_p}{b_n + b_p} \qquad (4.23)$$

which is equal to the Q_m of the tank circuit of Figure 4.6(b), as expected. Assuming $m_p/m_n \gg 1$ and $\omega_m m_n/b_n \approx Q_{m,n}$, Equation (4.23) simplifies to

$$Q_{m,tot} = \left(\frac{m_p}{m_n}Q_{m,n}\right)||Q_{m,p} \qquad (4.24)$$

where the operator $||$ denotes the operation $x||y = (x^{-1} + y^{-1})^{-1}$, just like equivalent resistance of two resistors connected in parallel. It should be noted that the resultant $Q_{m,tot}$ is never larger than Q_m of the polysilicon ring. Rather, in the case $Q_{m,n}m_p/m_n \ll Q_{m,p}$ it appears that $Q_{m,tot}$ is boosted from Q_m of the silicon nitride ring by m_p/m_n times in the composite structure. If $Q_{m,n}m_p/m_n \gg Q_{m,p}$, then $Q_{m,tot}$ is simply equal to Q_m of the polysilicon ring. For the OMO designs of Table 4.1, $Q_{m,tot}$ results in the $Q_{m,p} > Q_{m,tot} > Q_{m_n}$ range, depending on the ratio m_p/m_n.

4.2.3 Experimental Results

Fabrication

Figure 4.8 depicts the microfabrication process to build the coplanar ring OMO structures. The process includes five lithography steps all using a deep-UV stepper and materials in a standard CMOS process, making the Q-boosted OMO attractive for low-cost batch fabrication. The process starts with LPCVD deposition of 3 µm Low-Temperature Oxide (LTO) and ~ 350 nm of low-stress silicon nitride on a standard six-inch silicon wafer to isolate the substrate and the electrical interconnects. A first LPCVD polysilicon film of ~ 350 nm is deposited with in-situ phosphorus doping and defined using the first lithography step to leave interconnect traces and bond-pads that facilitate electrical input-output and signal routing. Another thick LTO film is deposited as a sacrificial layer, followed by a CMP step timed to yield a final LTO thickness > 2 µm needed to keep the lossy polysilicon (interconnect) interface away from the optical field stored in the cavity, leaving the cross-section of Figure 4.8(a). CMP is an important step in the process since it removes the topography and any large surface roughness that can be detrimental to Q_o if transferred to the silicon-nitride cavity.
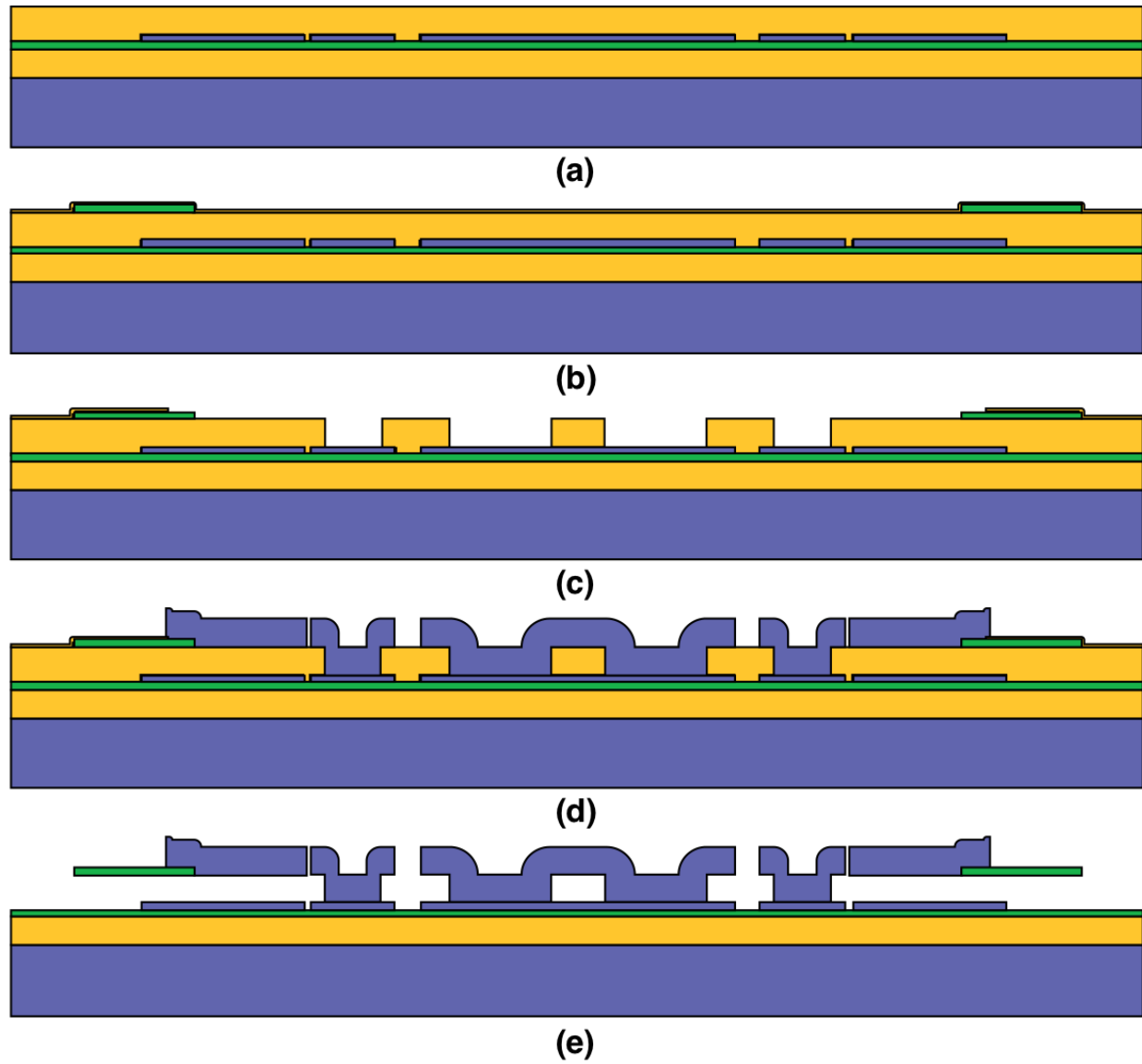
Figure 4.8: Summary of the fabrication process flow. (a) LTO and silicon nitride layers are deposited for electrical isolation and etch stop followed by polysilicon interconnect deposition and etch. Another LTO layer is deposited and CMP'ed to a final thickness of 2 μm, leaving a planar surface for the silicon nitride film. (b) The optical cavity is formed by patterning a 400 nm silicon nitride film and protected during subsequent etches by a thin layer of LTO. (c) Protective thin LTO is removed from the inner ring edge, followed by etching thick LTO to define anchors. (d) 2 μm of polysilicon is deposited and etched to define the polysilicon ring and electrodes. (e) Finally, devices are released in 49% HF, yielding the final cross-section of Figure 4.4(b).

Optical cavities are then formed by a 400 nm stoichiometric silicon nitride (Si_3N_4) film deposited via LPCVD, followed by the second lithography step. A final 100 nm protective LTO is then deposited over the etched Si_3N_4 to protect it during a later polysilicon etch step, which can induce roughness on the cavity if not protected. The third lithography step clears the protective LTO over the inner radius region of the optical ring to allow subsequent polysilicon depositing directly on the opening to form mechanical coupling and physical attachment between the Si_3N_4 and polysilicon rings. Another lithography step defines the anchor openings into the sacrificial LTO layer to achieve the cross-section of Figure 4.8(c), exposing polysilicon interconnect areas where the structure and electrodes anchored. The second polysilicon film of 2 μm is finally deposited to fill the anchor openings and form the high-Q_m polysilicon ring and electrodes, which also makes a good electrical connection with the first polysilicon interconnect layer. The final lithography step then defines the polysilicon ring and electrodes, leaving the cross-section of Figure 4.8(d) ready for the subsequent HF release.

Figure 4.9 shows SEM images of the released devices upon completion of the process, where each image reveals various details of the device design and structure.

OMO Performance

Figure 4.10 introduces the experimental setup used for coplanar ring OMO characterization. In order to have enough spectral resolution to measure high-Q_o optical resonances, swept laser measurement setup of Figure 4.10(a) is first used, where a computer sweeps a tunable laser's wavelength while recording the power at the cavity output using a photodetector and an oscilloscope. Figure 4.10(b) depicts the setup used for oscillator characterization, which employs the custom-built vacuum probe system described in [4] to provide medium (10 mBar) vacuum environment. It should be noted that the vacuum environment reveals the true Q_m of the structure by removing the air-damping induced mechanical loss and it can only help if other losses are already smaller than or comparable to the air damping. Structures with high anchor loss, for example, will exhibit similar Qm in air and vacuum, so their performance will not necessarily improve by operating in vacuum. Also, air damping becomes less significant at higher vibrational frequency [48], so high-Q_m operation in air is still possible with higher frequency OMO designs.

Figure 4.11 (a-c) present Brownian noise measurement of OMO designs 1-3 of Table 4.1, which reveal boosted Q_m values indicated in the figures. $Q_m = 22,355$ of design 1 is the highest measured double-ring Q_m, which is more than 2× higher than demonstrated in a previous silicon nitride ring OMO [4]. To gauge the degree to which Equation (4.24) matches the measured $Q_{m,tot}$ requires knowledge of the $Q_{m,p}$ of a spoke-supported polysilicon ring and the $Q_{m,n}$ of an unsupported nitride ring. The former is readily measured to be on the order of 40,900 on an actual polysilicon-only ring as shown in the insertion loss measurement of Figure 4.11(d). The Q_m of an unsupported nitride ring, on the other hand, is much more elusive, since any real fabricated nitride ring does have supports, so suffers from anchor loss not present in an unsupported (levitated) ring. Considering the highest Q_m of 10,400
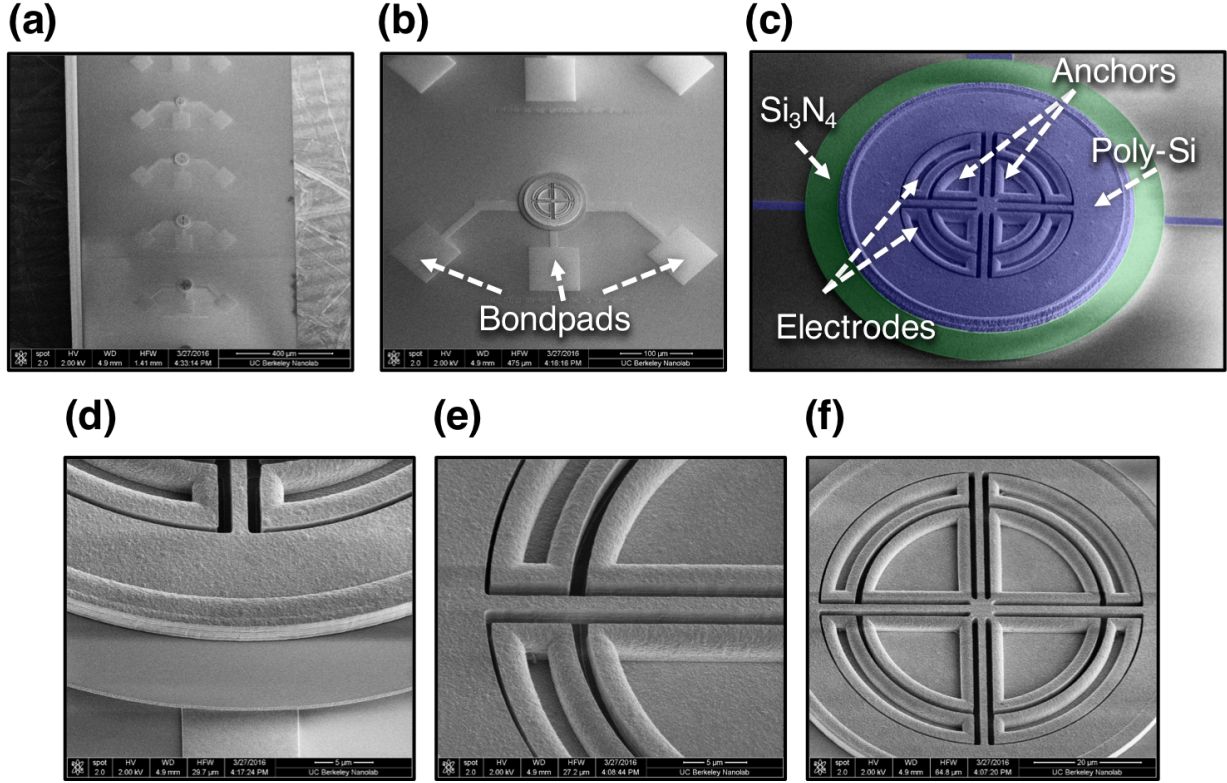
Figure 4.9: SEM images of Q_m-boosted coplanar ring OMO's. (a) Hundreds or thousands of devices are fabricated with the wafer-level process technology on a single wafer. The image shows only one die that is separated from the wafer using a wafer saw. The die width is kept narrow for containing only one device in the horizontal direction to avoid fiber coupling to multiple devices at the same time. (b) A single device with bondpads that allow electrical probing in a vacuum probe station. (c) Colorized SEM of the device that highlights different materials, where purple is polysilicon ring and electrodes, and green is the silicon nitride ring. (d) Zoom-in on the silicon nitride ring on the outer edge of the device where it couples to polysilicon ring. Smooth nitride film shown in the image is crucial to achieve high Q_o's. (e) Zoom-in on a polysilicon spoke that supports and holds the resonator structure. On both sides of the spoke where it connects to the polysilicon ring are the device electrodes that overlap with the polysilicon ring. (f) A larger device with easily visible large anchor areas.

measured among several fabricated spoke supported 1st radial contour mode nitride rings [4], a reasonable estimation would be somewhere between 10,000 to 50,000. With the above Q_m values and 1.61 ng nitride and 7.76 ng polysilicon effective masses calculated in Table 4.1, Equation (4.24) predicts a $Q_{m,tot}$ of 22,125 to 34,965 for the composite OMO. Measured $Q_{m,tot}$ values of 14,000 to 22,000 is not far from this estimation, but may suggest that the nitride-polysilicon coupling alters the individual Q_m's, perhaps by changing the device
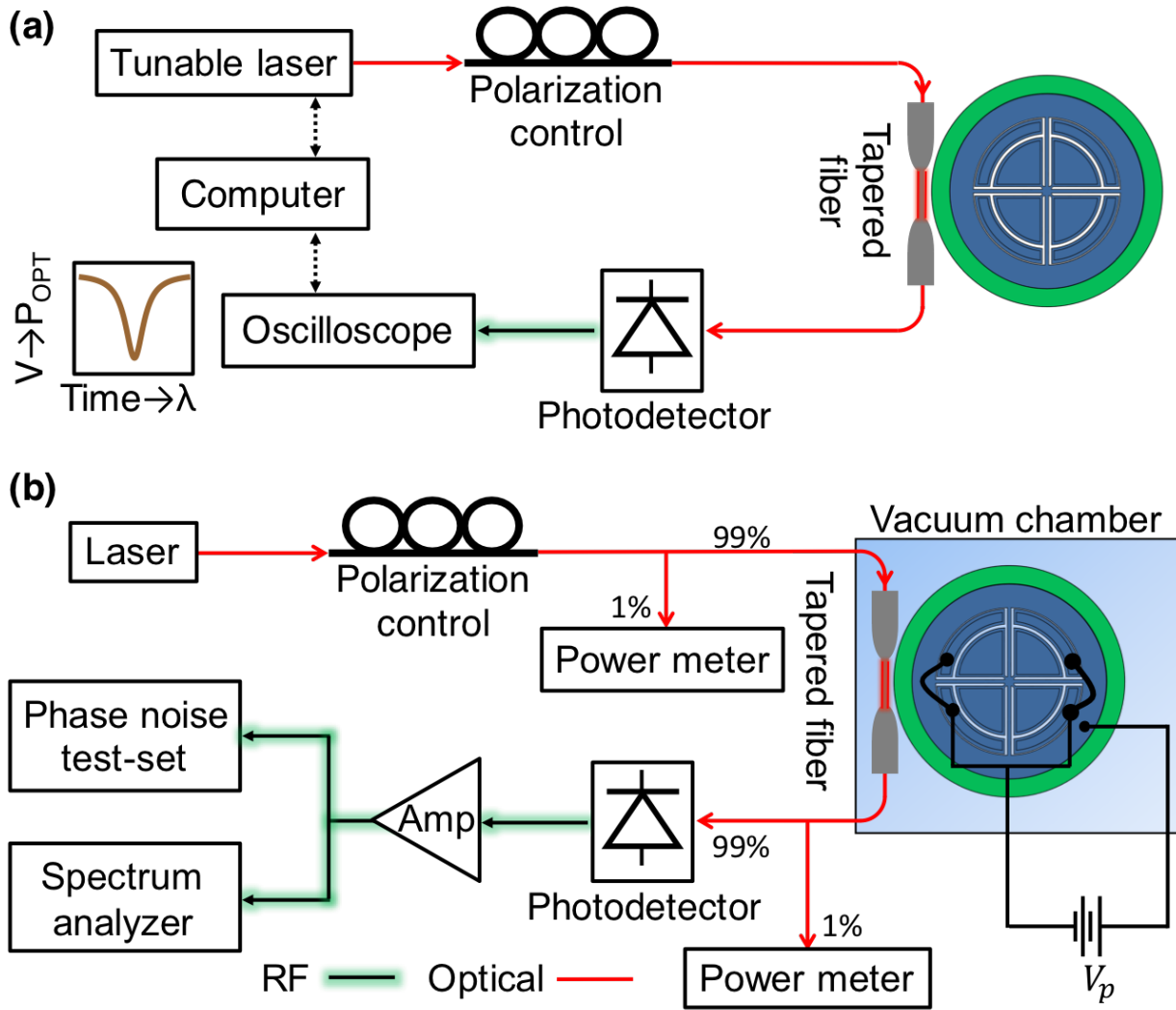
Figure 4.10: Schematic description of the experimental measurement setup. (a) Optical-Q measurement setup employs a computer that sweeps the laser frequency while recording optical power in time. Use of the vacuum chamber is optional. (b) Setup for phase noise and mechanical-Q measurements employing a custom-built vacuum chamber as described in [4]. An Agilent E5505A phase noise test system is used for phase noise measurements.

geometry due to film stress.

Figure 4.12 presents the measured optical transmission spectra of OMO designs 1 and 2 with characteristic multiple WGM resonances that exhibit Q_o's as high as 283,370. This performance is no less than what is typically expected from silicon-nitride-only rings, proving the efficacy of coplanar ring OMO's unique design to achieve such high-Q_o's.

Figure 4.13 presents the measured phase noise for the OMO of -114 dBc/Hz at 1 kHz

(a)

Q_m=22,300

(b)

Q_m=14,900

(c)

Q_m=12,400

(d)
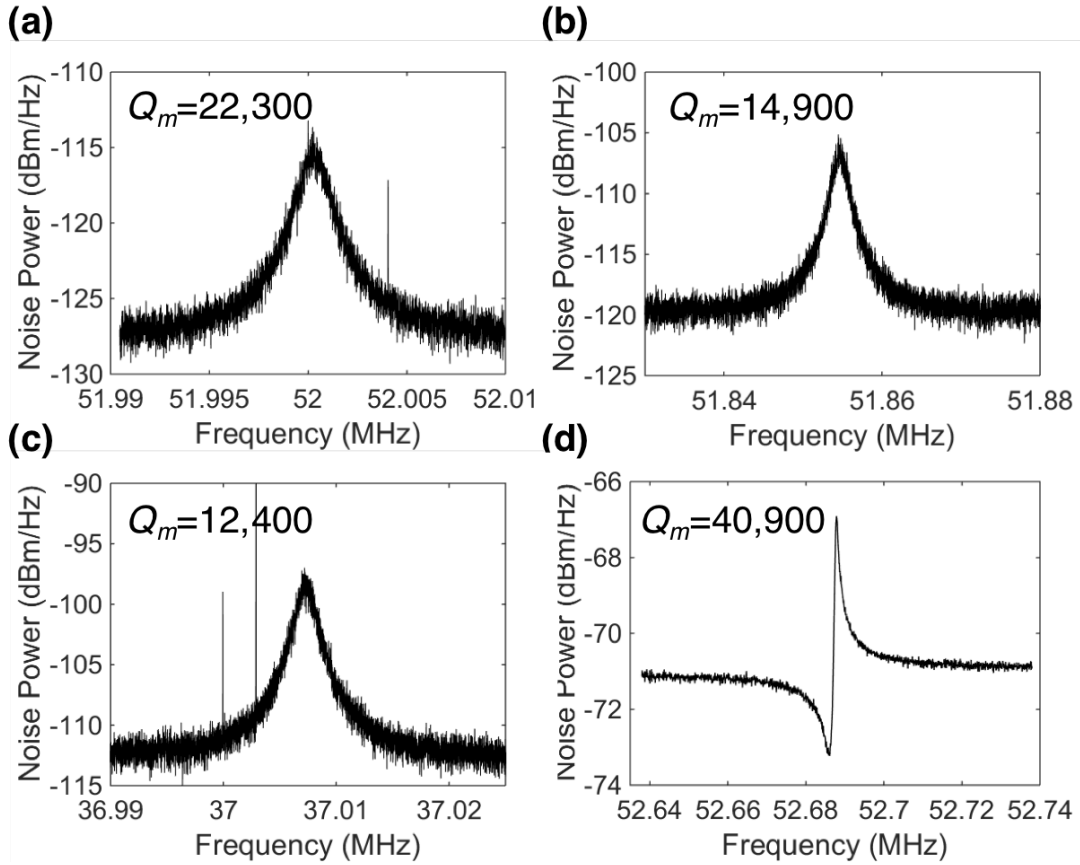
Q_m=40,900

Figure 4.11: (a-c) Measured Brownian motion of the Q-boosted coplanar ring OMO designs 1-3 of Table 4.1, from which Q_m values are extracted. (d) Measured insertion loss of a single polysilicon ring that reveals a much higher $Q_m = 40,900$, as expected.

and -142 dBc/Hz at 1 MHz offsets from its 52 MHz carrier, which is 12 dB better than the previous state of the art OMO constructed of silicon nitride alone [4]. This phase noise performance, when divided down to 13 MHz using oscillator figure-of-merit [50], satisfies GSM reference oscillator phase noise specification [51] at far-from-carrier offsets; while being only 4 dB higher at 1 kHz offset, proving OMO technology to be a strong competitor for MEMS and even quartz-based oscillators. It is also notable that the OMO input laser power of only 3.7 mW has been sufficient to achieve such a good performance compared to 7.5 mW input power of the previous state-of-the-art [4], which is enabled by the higher Q_m together with the high-Q_o preserved within the coplanar ring OMO.

Figure 4.14 present OMO output spectra under several tuning voltages and measured plots gauging oscillating OMO frequency versus tuning voltage, where a relatively large 440 nm electrode-to-resonator gap spacing still allows a 3 ppm/V (Parts-Per-Million/V) frequency shift suitable for locking to the Rb vapor cell in a CSAC. Indeed, frequency tuning
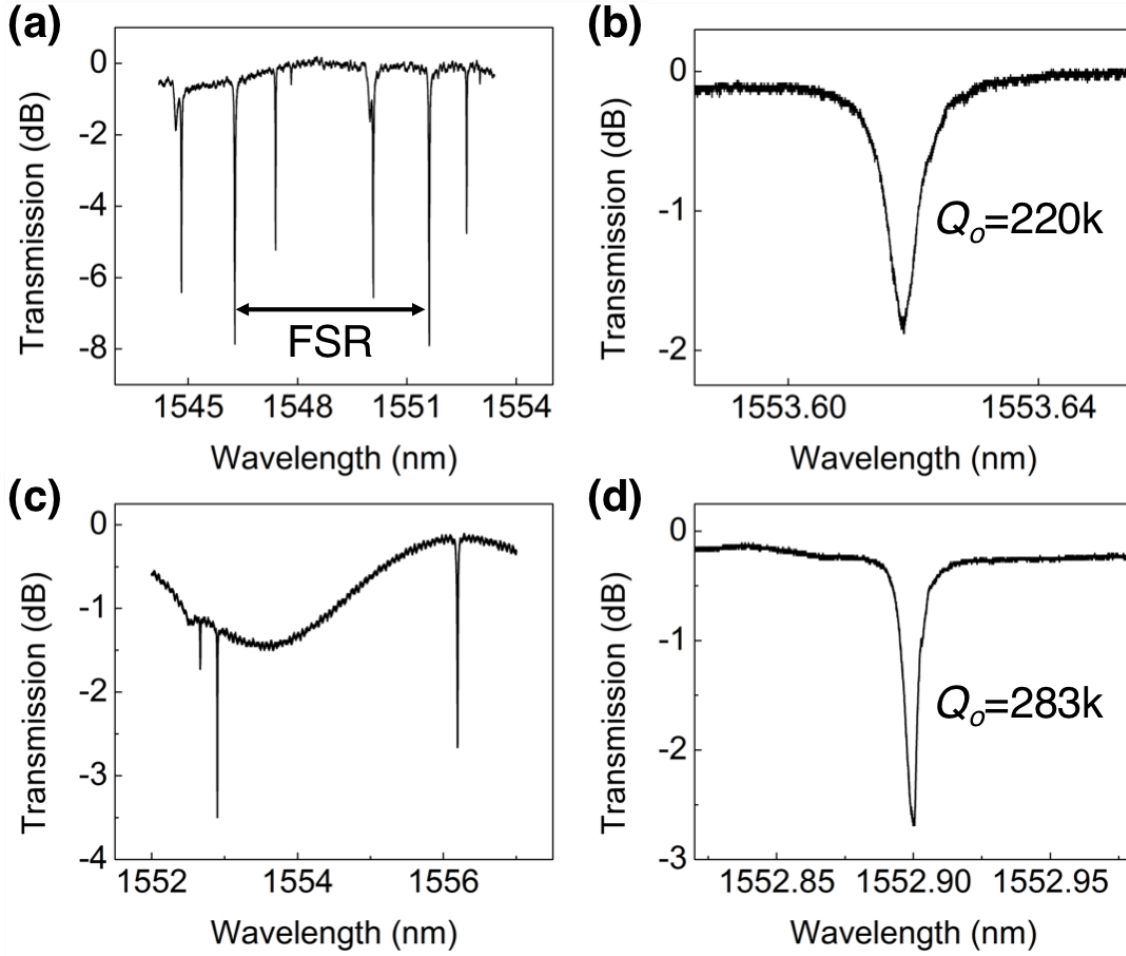
Figure 4.12: Measured optical transmission spectra of coplanar ring OMO designs 1 and 2 of Table 4.1. (a) Design 1's spectrum with repeating resonances showing its Free Spectral Range (FSR). (b) Zoom-in on one of the peaks reveals $Q_o > 220,000$. (c) Spectrum of Design 2, and (d) zoom-in on a high-Q_o peak with $Q_o > 283,000$.

enables coplanar ring OMO phase-locking using higher harmonics to an external reference to improve the long-term stability substantially, proving the concept of using higher-harmonic phase-locking in the target CSAC application.

4.2.4 Higher Harmonic Locking

Off the checklist items for a low power CSAC implementation presented in the introduction of this chapter, the only remaining one to be demonstrated is the higher harmonic locking. Pursuant to demonstrate this capability, this section presents phase-locking of the Q-boosted
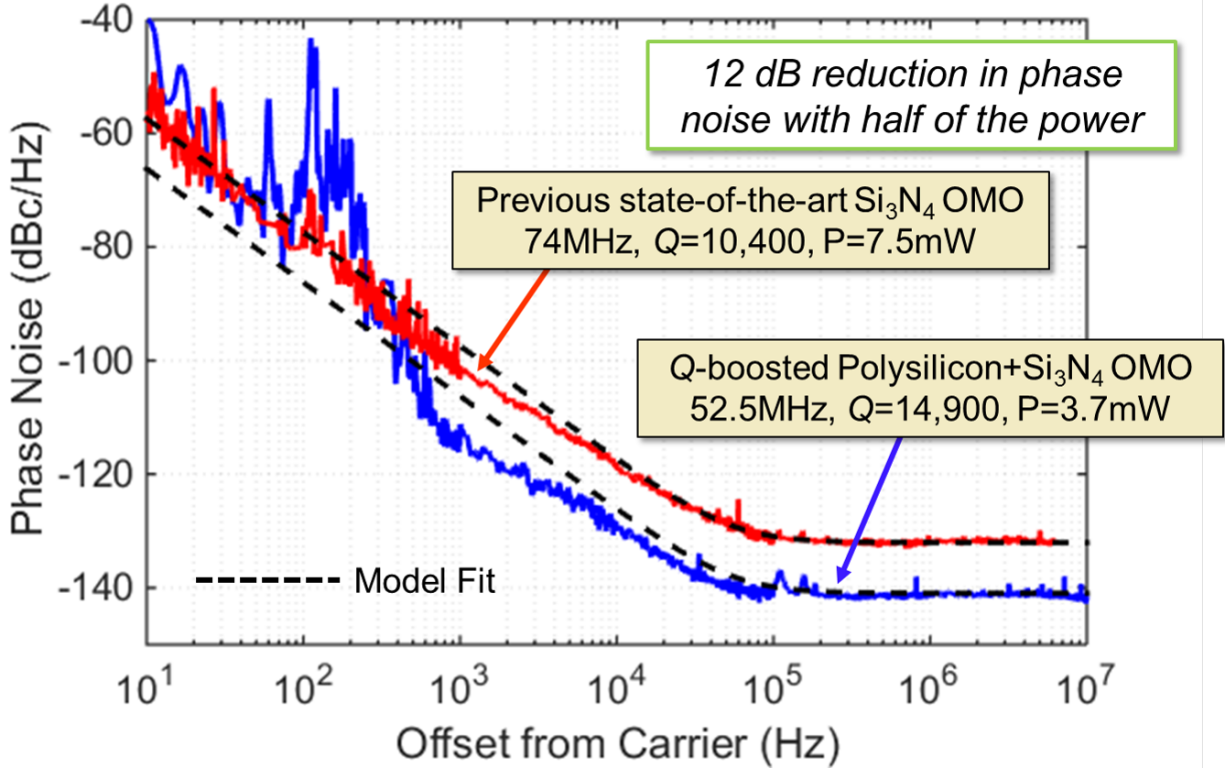
Figure 4.13: Phase noise of the Q-boosted OMO compared to the previous best silicon nitride-only OMO [4]. Blue and red solid lines are measured spectra with device values and measurement power indicated in the figure. As expected, the boosted Q_m lowers the phase noise, achieving a 12 dB improvement at both 1 kHz and 1 MHz offsets. Black dashed lines are model fits from the phase noise model presented in Chapter 3.

coplanar ring OMO to a microwave source using one of its higher-order harmonics, as previously presented by Alejandro Grine in [52] who designed the experiment.

In the intended CSAC application, phase noise of the locked OMO at small frequency offsets follows the excellent long term stability of the lock reference. However, unlike a high quality signal source (such as a quartz oscillator), the hyperfine transition frequency stability is poor at short time scales. Therefore, at large offset frequencies the locked system has to follow the phase noise of the free running OMO, so the effective CSAC lock bandwidth is intentionally kept small.

In our harmonic locking demonstration, the Q-boosted OMO posts phase noise of -140 dBc/Hz at greater than 50 kHz offset, a 20 dB improvement over the previous harmonic lock demonstration [53]. Also, voltage controlled tuning eliminates the need for a separate intensity modulator and allows the detuning and input power to be targeted for optimal phase noise, threshold power, or harmonic generation. Phase locking greatly improves the
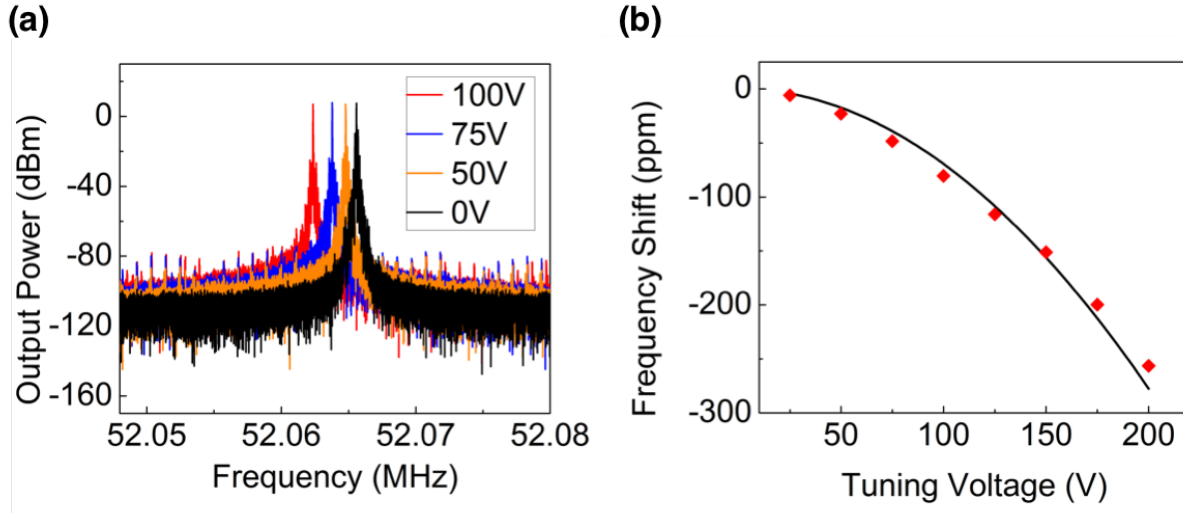
Figure 4.14: (a) *Q*-boosted OMO output spectrum under several applied tuning voltages, demonstrating frequency tuning. (b) Measured frequency shift with respect to applied voltage (via curve-fitting) indicate a 440 nm resonator-to-electrode gap spacing.

OMO's long term drift while simultaneously retaining its excellent short term characteristics. Phase-locking the 9th harmonic of an OMO at 466 MHz to an RF signal generator improved the phase noise by 85 dB at 1 Hz offset, while maintaining a phase noise of -140 dBc/Hz at offsets > 50 kHz.

Figure 4.15 presents the setup used for harmonically locking the OMO to a low noise reference by mixing photodetected light at the cavity output with an RF signal generator set near the ninth harmonic frequency of 466 MHz. The frequency comb imprinted on the photodetector output then mixes with a low noise SRS SG384 RF signal generator. After a low pass filter, the error signal that is proportional to the difference in phase between the OMO harmonic and the signal generator is further filtered by an SRS SIM960 proportional-integral (PI) controller followed by a high voltage amplifier. The final control voltage then feeds the device tuning electrodes to tune the oscillation frequency. Variable optical and RF attenuators prevent saturation of the photodetector and RF amplifiers respectively ensuring harmonics are only created through optomechanical transduction.

Figure 4.16 shows the measured phase noise of the (blue) unlocked vs. (red) locked OMO which shows an 85 dB improvement at 1 Hz offset. The OMO harmonically locked to an oven-controlled crystal borrows the excellent long term frequency stability of the signal generator with little to no degradation in the excellent short term stability of the OMO, just as desired in the intended CSAC application.
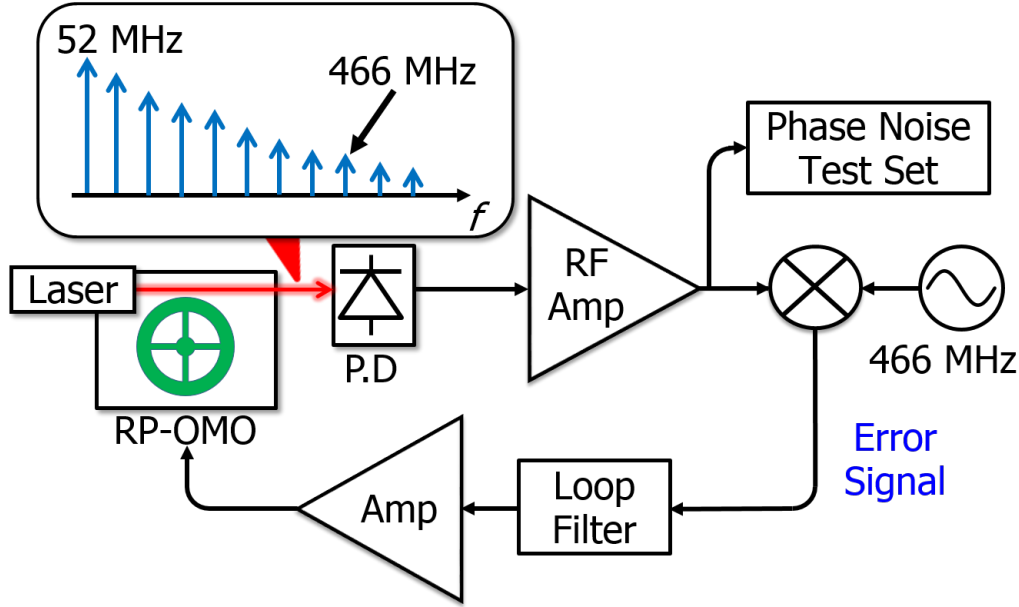
Figure 4.15: Pictorial representation of the experimental setup used in harmonic locking. In an actual CSAC implementation, the optical output from OMO would directly feed the external frequency reference (Rb vapor cell) and use of a mixer would not be necessary.

4.3 3-D Stacked Ring OMO with Large Electromechanical Coupling

Although the coplanar ring OMO design of the previous section has shown the best-to-date performance among all OMO's, there are still possible areas of performance improvement, especially in the electrical domain. Electromechanical coupling limited by the lithographically defined electrode-to-resonator gap spacing necessitates using rather large DC voltages to achieve enough coupling for frequency tuning and (direct) output electrical current. State of the art MEMS resonators generally utilize a sacrificial layer in the fabrication process for the definition electrode-to-resonator gap spacing, which allows much better precision and resolution due to easy control of deposition thickness compared to lithographic methods. This type of sacrificial layer defined gaps could also be used in a coplanar ring OMO process but it was traded off for a simpler process in OMO's of the previous section.

The second multi-material OMO design presented in this thesis is a 3-D design dubbed stacked-ring OMO, which couples a high-Q_o (but low-Q_m) ring via a vertical coupling beam to a high-Q_m (but low-Q_o) and electrically conductive ring or ring array. Figure 4.3 illustrates an example design using three high-Q_m conductive rings in the lower plane with surrounding electrodes and a high-Q_o ring in the upper plane, where the two layers are connected with four vertical beams. This design allows integration of more high-Q_m resonators for larger electromechanical coupling by removing the optical layer from mechanical resonator plane,
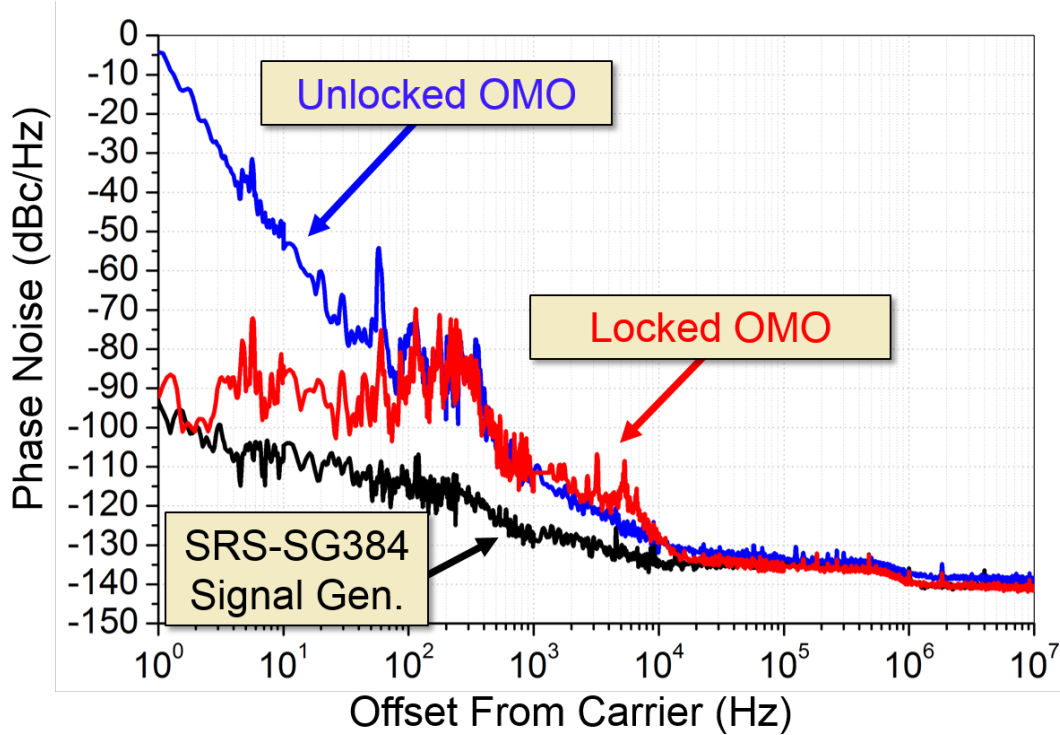
Figure 4.16: Phase noise improvement by harmonically locking a Q-boosted coplanar ring OMO to an external signal generator using its 466 MHz harmonic. Blue trace shows the phase noise of the free-running OMO used in the experiment, before phase locking. Black is the measured phase noise of an oven-controlled crystal oscillator based table-top signal generator unit SRS-SG384, which shows excellent close-to-carrier phase noise. Red is the measured phase noise at the OMO output, with a remarkable 85 dB improvement at 1 Hz offset after phase locking.

enabling the use of lateral coupling beams to add more mechanical resonators into the array as well as placement of electrodes on the outer ring periphery with larger electrode-resonator overlap area. Vertical separation of optical layer from the electromechanical resonators removes the optical design constraints in the electromechanical layer and vice-versa, allowing independent optimization and more flexible fabrication. As will be seen, the stacked-ring OMOs achieve 170 ppm/V electrical frequency tuning by using a sacrificial layer defined gap process just like the MEMS resonators of Chapter 2. In this regard, the stacked ring OMO fabrication can rely on on a MEMS shuttle process where the devices are fabricated after MEMS resonators with two additional lithography steps.

The following section introduces the first 3-D stacked-ring OMO realization using polysilicon and silicon nitride thin films for the MEMS and optical layers similar to the coplanar ring devices.

4.3.1 Nitride Over Silicon Stacked Ring OMO
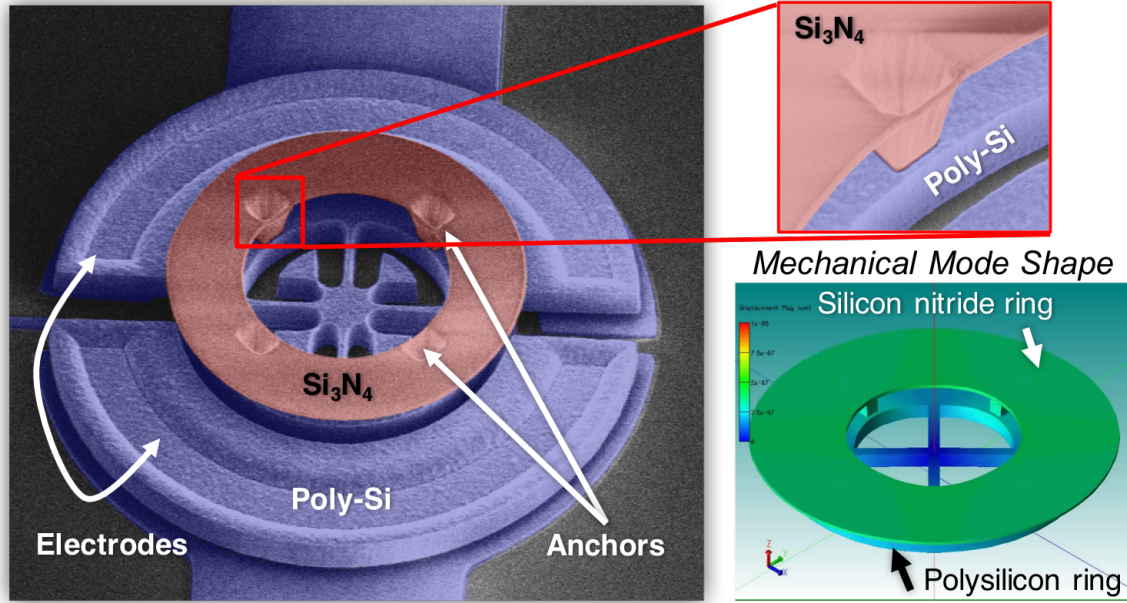
Figure 4.17: Colorized SEM images of the fabricated stacked-ring OMO's. Red silicon nitride ring mechanically couples to the polysilicon ring underneath via vertical beam couplers. Zoom-in on the vertical coupler (upper right-hand side panel) shows the via placement that is intentionally kept away from the silicon nitride outer edge to preserve high Q_o. Vertical beams with $\approx 0\lambda_m$ length ensures that both rings vibrate in phase in breathing contour mode shape as shown in the FEA simulation (lower right-hand side panel).

As illustrated in the general device structure of Figure 4.3, multi-material stacked-ring composite OMO implementation comprises of a high-Q_o and one or more high-Q_m resonators realized here with silicon nitride and a polysilicon ring structures coupled in a vertical fashion to allow virtually independent optimization of optical and mechanical properties as well as electromechanical coupling.

The first rendition of this device, with lithographically defined electrode gap requiring a simpler fabrication but sacrificing electromechanical coupling, realized an 87-MHz OMO with a threshold power fraction of a milliwatt. Figure 4.17 presents a colored SEM image of the stacked-ring OMO where the purple layer shows the polysilicon ring with surrounding electrodes, and the red shows silicon nitride ring atop. A zoom-in on this image (b) reveals the vertical coupling between the nitride and polysilicon. This coupling scheme ensures that the optical field stored in the silicon nitride cavity is not affected by the mechanical coupling, which in turn allows retention of high optical-Q. As such, the composite device exhibits $Q_o > 154,000$ comparable to a silicon nitride-only cavity. The vertical coupling

further allows optimized electrode placing around the device since the cavity (hence the optical field) is far above from the optically lossy polysilicon layer.
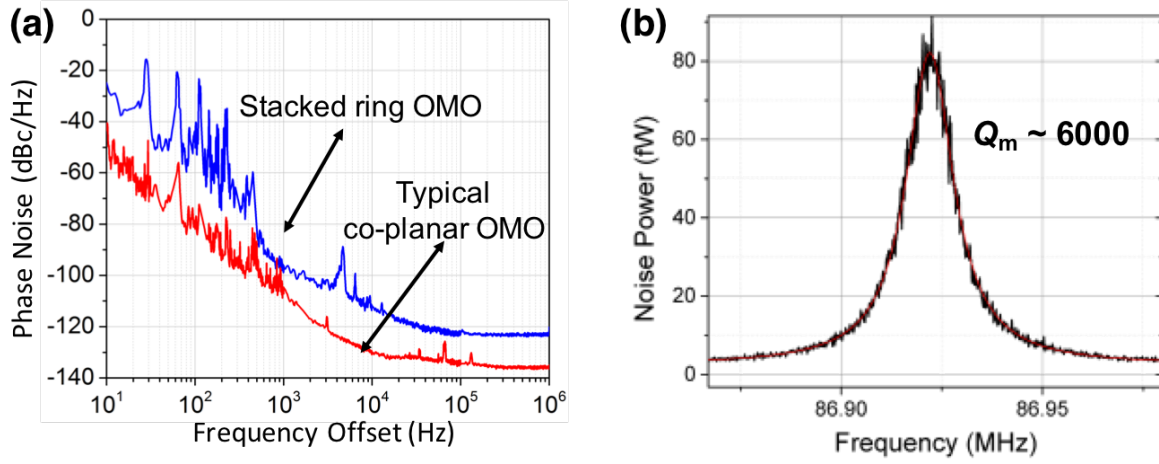
Figure 4.18: (a) Measured phase noise of a stacked-ring OMO. Although the structure has large m_{eff}, it can still oscillate with small input power due to high Q_o in the order of 150,000. Despite the lower than expected Q_m (b), phase noise of the stacked-ring OMO is still better than many of the previous single-material OMO demonstrations owing to its large m_{eff} and high enough Q_o

.

Characterization of stacked-ring devices employs the experimental setup and techniques presented in Section 4.2.3. The 3-D device geometry allows easier tapered fiber-to-device alignment since the optical cavity is elevated far from the substrate.

Figure 4.18 presents the measured phase noise and Q_m of the stacked ring OMO, which, although adequately low for many applications, isn't as remarkable as the phase noise performance of the Q-boosted coplanar ring OMO of the previous section. The device exhibits a rather lower mechanical-Q of 6,000 which then limits the phase noise performance. The unexpectedly low polysilicon-only resonator Q_m suggests a possible culprit which is bad polysilicon film quality obtained during deposition that may not be well-controlled in a shared laboratory environment.

The second rendition of the stacked-ring OMO uses a process similar to previously demonstrated MEMS resonators [54] with additional top electrode planarization, which allows definition of the electrode gap spacing by the sacrificial layer thickness–a much more precise and scalable technique to define the gaps compared to lithography. With the sacrificial layer defined gap process, stacked-ring OMO's achieve much smaller gap and much stronger electromechanical coupling. The addition of silicon nitride ring and vertical couplers above MEMS just require 2 more lithography steps on top of a mature and standard process flow. Figure 4.19 shows measured resonance frequency of such a device under several different

Electrical Transmission (s21)   Frequency vs Bias Voltage
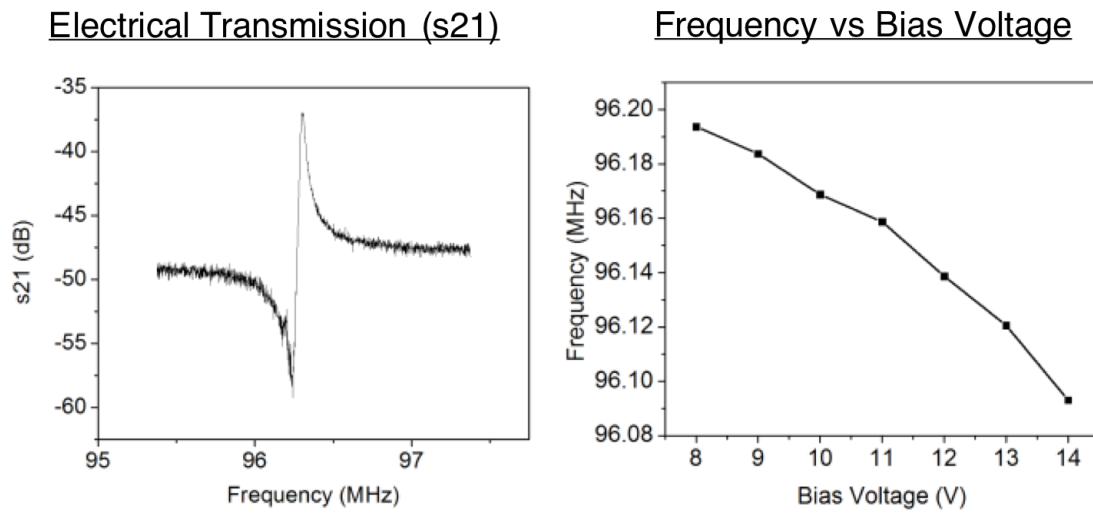
Figure 4.19: Measured insertion loss and frequency versus tuning voltage plots for the stacked-ring OMO. The tuning curve with strong coupling is consistent with the intended 40 nm process.

bias voltages which is consistent with the deposited sacrificial layer thickness of 40 nm. This yields a frequency shift of approximately 170 ppm/V compared to 3 ppm/V of the coplanar ring OMO.

Chapter 5

An OMO Based Optical Receiver

This chapter demonstrates a super-regenerative optical receiver that detects on-off key (OOK) modulated light inputs by harnessing the radiation-pressure gain of a self-sustained electro-opto-mechanical oscillator (EOMO) to render its oscillation amplitude a function of the intensity of light coupled into the oscillator. This is, to our knowledge, the first demonstration of an OMO-based optical receiver converting optical information to electrical digital signal at its output. The super-regenerative receiver architecture used in this work removes the need to periodically quench the oscillation signal unlike the previous electronic super-regenerative receivers, which then simplifies the receiver architecture and increases the attainable receive bit rate. A fully functional receiver with a compact ~ 90 μm EOMO comprised only of silicon-compatible materials demonstrates successful recovery of a 2 kbps (kilobits per second) bit stream from an OOK modulated 1550 nm laser input. By removing the need for the expensive III-V compound semiconductor materials often used in conventional optical receivers, this EOMO-based receiver offers a lower cost alternative for sensor network applications.

5.1 Introduction

Radiation pressure-driven optomechanical oscillators have proven useful in stand-alone oscillator [5], communications [14], and sensing applications [15]. The addition of electrodes to conventional optomechanical devices allows electrically coupled inputs as demonstrated with coplanar ring devices in Chapter 4 and in [55],[56] as well as optical ones that then enable new integrated electro-optomechanical systems where electrical signals modify optical properties [57]. The converse should also be true, where laser light coupled to an electro-optomechanical system might change the electro-mechanical properties of the device, perhaps in a way that allows electrical detection and decoding of optical signals. If possible, this might then enable an optical receiver constructed strictly in silicon compatible materials, i.e., with no need for compound semiconductor photonic devices and the associated cost and technology required to integrate them alongside silicon electronics.
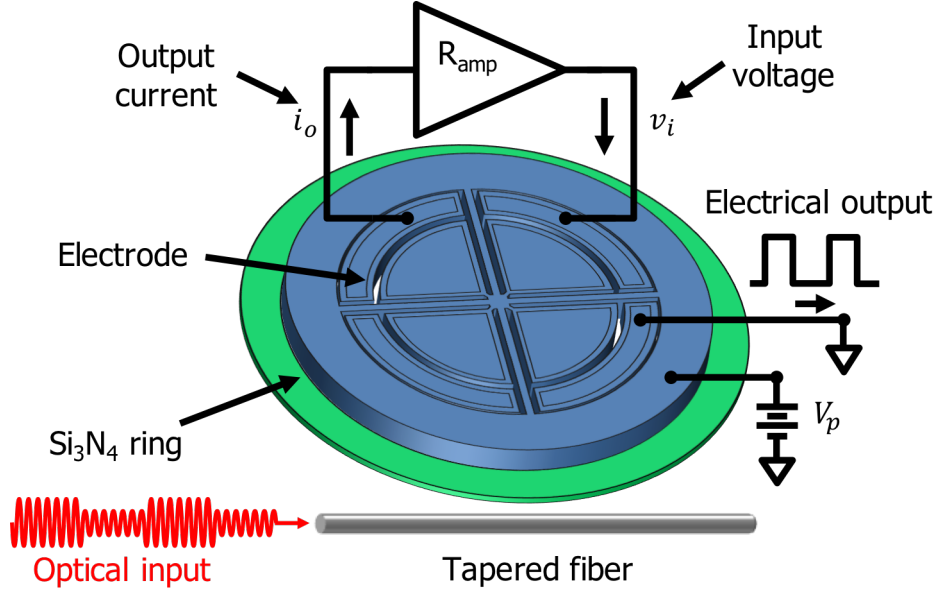
Figure 5.1: Perspective-view schematic of the EOMO and basic receiver operation. Here, an electronic amplifier connects to input/output polysilicon electrodes and sustains oscillation. An amplitude modulated optical input couples to the Si3N4 ring of the EOMO and changes the output electrical oscillation amplitude, which indicates the received bits.

Pursuant to capitalizing on this possibility, and spurred by recent demonstrations of simple low power MEMS radios based on super-regenerative reception [58],[59], this work presents for the first time a fully functional super-regenerative optical receiver based on an electro-opto-mechanical oscillator (EOMO), cf. Figure 5.1, that detects OOK modulated light input and directly demodulates and recovers input bits in the electrical domain. The key enabler here is the simultaneous use of both electrical and optical input/output (I/O) ports, the former used in the positive feedback loop of a self-sustained electronic oscillator circuit; while the latter used to accept optical inputs that perturb the steady-state oscillation amplitude of the electronic oscillator. Via use of an EOMO constructed of only silicon-compatible materials, this receiver obviates the need for compound semiconductor technology while still providing optical reception commensurate with the needs of massive autonomous sensor networks, for which cost is paramount [60].

5.2 Device Operation

The EOMO illustrated in Figure 5.1 comprises a high-Q_m polysilicon inner ring mechanically attached at its outer edge to a concentric high-Q_o stoichiometric silicon nitride ring, just like the coplanar double-ring OMO presented in Chapter 4.

With the Q_m-boosting as a result of mechanical coupling, the composite structure exhibits

a much higher Q_m than otherwise provided by a silicon nitride-only ring while still preserving the high-Q_o of silicon nitride. This combination of high Q_m and high Q_o is key to low power and low phase noise in the present wireless receiver.

5.3 Electrical I/O

Electromechanical coupling used for voltage-controlled frequency tuning of the OMO's demonstrated in Chapter 4 also allows electrical inputs that can induce mechanical vibrations at the frequency of input signal. Exciting the EOMO electrically entails applying a DC bias V_P to the conductive polysilicon ring and an AC voltage v_i to an input electrode, where $V_P >> v_i$. The voltage difference across the capacitive gap generates a time-varying force

$$F_e = \frac{1}{2}\frac{\partial C_i}{\partial x}(V_P - v_i)^2 \tag{5.1}$$

that drives the ring into mechanical vibration. The amplitude of vibration significantly increases when the mechanical resonance and excitation frequencies match, i.e., in the case of resonant drive. Keeping only the resonant term in Equation (5.1), magnitude of the excitation force becomes

$$F_e = \frac{1}{2}\frac{\partial C_i}{\partial x}2V_P v_i \tag{5.2}$$

and the amplitude of motion generated by this force at the resonant frequency is simply

$$x = Q_m \frac{F_e}{k_{eff}} \tag{5.3}$$

The ensuing motion then generates displacement currents across each DC-biased time-varying gap with an amplitude given by Equation (4.16), which can then serve as output signals proportional to displacement or velocity. The amount of output current i_o for a given excitation voltage v_i is governed by motional impedance of the device, defined as $R_x = v_i/i_o$. Expressing the input voltage and output current in terms of the resulting force and motion yields

$$R_x = \frac{v_i}{i_o} = F_e\left(V_P\frac{\partial C_i}{\partial x}\right)^{-1}\left(\dot{x}V_P\frac{\partial C_o}{\partial x}\right)^{-1} \tag{5.4}$$

Partial derivatives of the input-output capacitances, derived in Equation (4.18), reduce to C_o/d_o since only resonant-AC terms are relevant and EOMO has equal input and output overlap capacitances. In terms of design parameters, expression of EOMO motional impedance becomes

$$R_x = \frac{F_e}{\dot{x}}\frac{d_o^2}{V_P^2 C_o^2} = \frac{k_{eff}do^2}{\omega_m Q_m V_P^2 C_o^2} \tag{5.5}$$
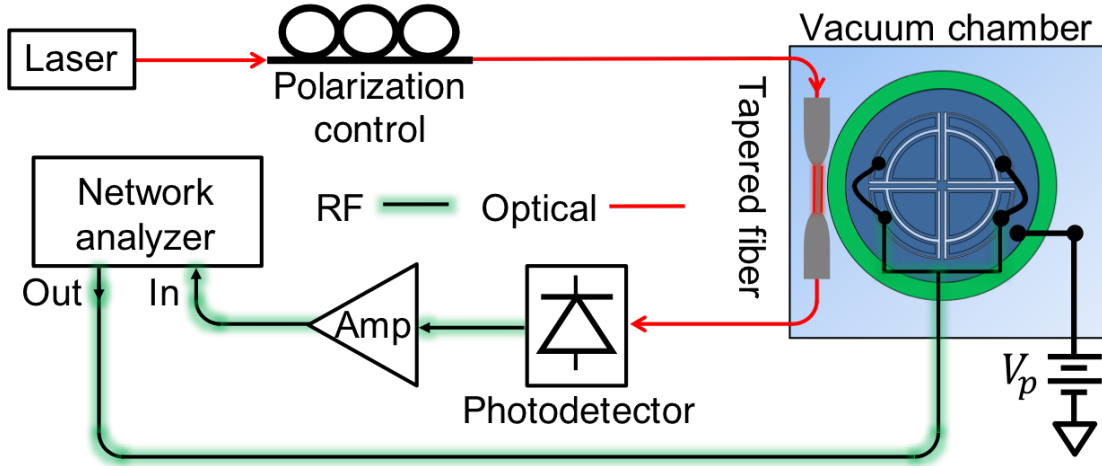
Figure 5.2: EOMO optical modulator characterization setup. EOMO is driven by the electrostatic force that is swept across frequency using a network analyzer. Mechanical motion induced by the electrostatic force modulates the optical output field of the EOMO, which then feeds a photodetector to convert the modulation to electrical signals. Received signal at each frequency is recorded by the network analyzer and the ratio of the received signal amplitude to the excitation amplitude is conveniently displayed as an s_{21} trace.

Motional impedance is an important parameter since it dictates the required sustaining amplifier gain for an electronic oscillator referenced to a MEMS resonator. It is also important for the EOMO-based optical receiver as will be explained in the coming sections.

5.4 Optical I/O

Just as in the pure OMO demonstration of Chapter 4, optical I/O is facilitated by a tapered fiber and the silicon nitride outer ring of the EOMO. However, different than the operation in Chapter 4, EOMO does not require high input optical power to sustain mechanical oscillations. Rather, the input signal for detection needs to be high enough to detect the increase in the oscillation amplitude.

5.5 EOMO as an Optical Modulator

Before proceeding to the fully operational optical receiver implementation, it is useful to look at how the electrical excitation induce mechanical vibrations and how these vibrations are manifested as modulation in the optical output of the EOMO. The super-regenerative optical receiver application will then exploit the converse effect where the input optical signal increases the vibration amplitude, thereby inducing a larger electrical signal at the output.
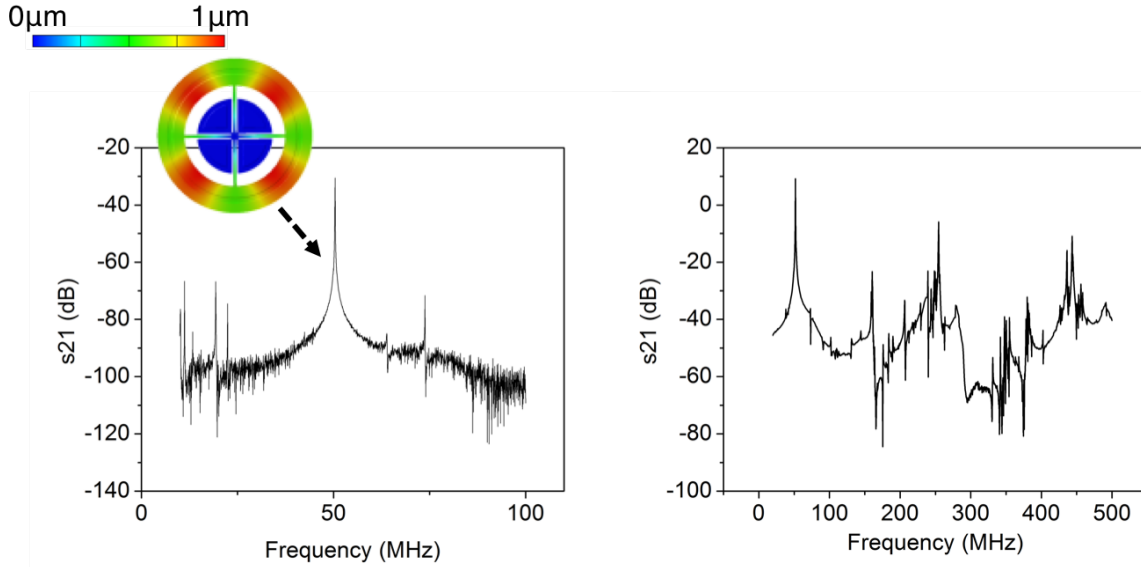
Figure 5.3: Measured modulator response from the setup of Figure 5.2. Although the displayed signal levels is in the form of "insertion loss" measurement, it is not an insertion loss measurement in the strict sense, so the absolute values are not of much importance. However, the signal level above the measurement floor is a good indication of how much displacement ensues at each frequency as a result of electrostatic actuation. In other words, measured peak heights gauge the displacement amplitude for each mechanical mode that can couple to the optical field. On the left is a zoom in on the largest peak which corresponds to the breathing contour mode as expected. Wider frequency sweep on the right reveals many mechanical modes, most of which is invisible with a pure electrical measurement due to low electomechanical coupling-high measurement floor, showing the impressive sensitivity of the optical probing technique for measuring mechanical displacements.

To operate the EOMO as an optical modulator, the device is electrostatically actuated by applying a DC voltage V_P to the polysilicon ring structure and an AC voltage to its electrodes, while being probed with a continuous-wave (CW) laser using a tapered fiber. Vibrational motion driven by the capacitive actuators shifts the optical resonance frequency via the moving optical boundary, i.e. the optomechanical coupling (g_{om}) described in Chapter 3. This optical resonance shift in turn modulates the optical intensity at the device output, creating a modulation sideband near the laser. This is the underlying mechanism of the optical modulation using EOMO which takes electrical signals, convert them into mechanical vibrations and finally to optical modulation. Figure 5.2 depicts the experimental setup used for characterization of the EOMO-based optical modulator, where an electrical network analyzer output feeds the EOMO electrodes for electrical modulation and detects optical modulation amplitude at its input. The use of a network analyzer conveniently allows sweeping the modulation frequency and looking at the modulator response as a transmission

spectrum (s_{21}) that reveals multiple mechanical resonances.
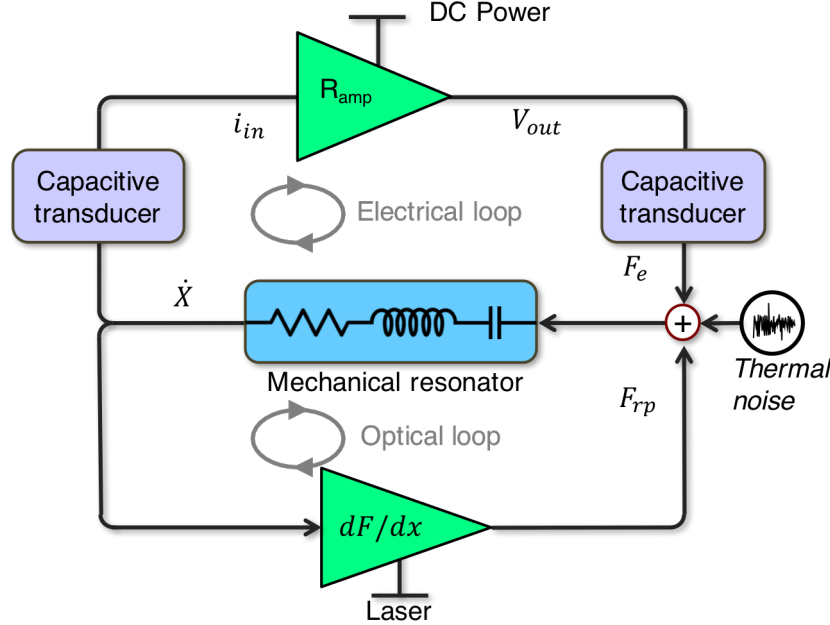
Figure 5.4: Super-regenerative optical receiver model. Light received at the proper wavelength forms an additional positive feedback loop, thereby raising the steady-state oscillation amplitude from the no light case (where only the upper branch contributes to the loop gain).

The use of mechanical resonator for the optical modulation results in a frequency-dependent modulation amplitude since the amplitude of vibration is much larger at the (mechanical) resonant frequencies and also depends on the electromechanical coupling strength of these mechanical modes. Therefore, the EOMO realizes a narrow-band optical modulator in contrast to common optical modulators with wide bandwidth. An application that can benefit from such narrow-band optical modulator is an opto-acoustic oscillator [35], where essentially the network analyzer in Figure 5.2 is replaced with an electrical amplifier (and a phase shifter for proper 2π phase shift around the loop), creating a positive-feedback loop between the electrical amplifier and mechanical resonator with an optical detection scheme for the mechanical motion. This oscillator implementation is especially useful for exciting the high frequency mechanical modes into oscillation, which may not be possible using a pure electromechanical excitation-detection scheme (like in MEMS resonators) due to reduced electromechanical coupling with the high frequency modes.

Figure 5.3 shows the resulting optical modulation spectrum using the setup of Figure 5.2 where the breathing contour mode creates the largest modulation as an expected result of the largest coupling. The sensitivity of the optical detection of motion is remarkable, which reveals many mechanical modes that are otherwise not visible within a pure electrical measurement spectrum.

5.6 Self-Sustained Oscillation
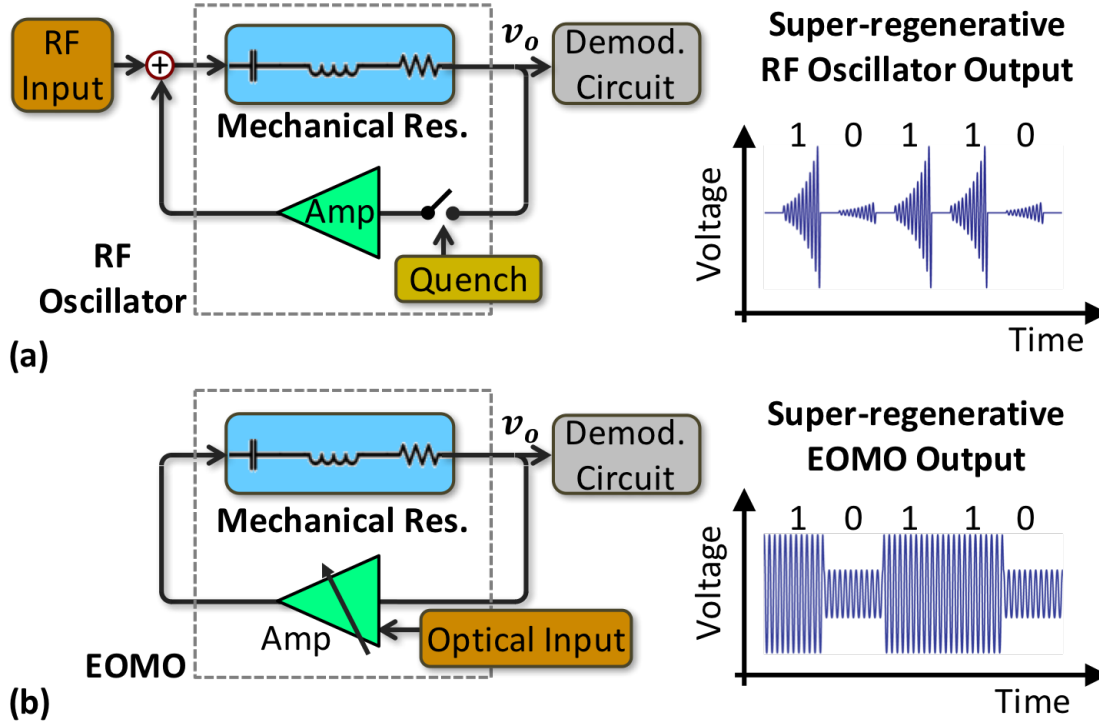
Figure 5.5: Comparison of conventional and EOMO-based super-regenerative receivers. (a) Reception of a "1" or a "0" is determined by the speed at which oscillations reach a prescribed threshold value starting from a quenched state. (b) Reception of a "1" or a "0", without quenching, is determined by the amplitude of oscillation, which can switch quickly, greatly increasing the permissible bit data rate.

With two I/O modes, the EOMO offers two methods to instigate self-sustained oscillation: electrical or optical. Figure 5.4 summarizes the two methods via a simple block diagram with two feedback loops. The electrical method is the same as that used in conventional oscillators [51], where two electrodes (i.e., capacitive-gap transducers) of the EOMO connect to the input and output terminals of an electronic amplifier to create a positive feedback loop with loop gain (A_l) greater than unity when $A_l = R_{amp}/R_x > 1$. Here, R_{amp} is the transresistance of the amplifier and R_x is the motional resistance between the EOMO electrodes embedded in the loop, given by Equation (5.5). With loop gain greater than unity, regenerative amplification of ring structure's Brownian motion at its resonance frequency eventually leads to sustained oscillation with steady-state amplitude governed by nonlinearities that reduce gain as amplitude increases. The "electrical loop" in Figure 5.4 summarizes the operative mechanisms in this mode of self-sustained oscillation.

The optical method, on the other hand, does not require an external amplifier, but rather just a strong enough blue-detuned laser input (or pump) to incite self-sustained optomechanical oscillation, as described in Chapter 3. Here, the field in the high-Q_o cavity builds up to a sizable circulating optical power that generates an outward radial radiation pressure force on the silicon nitride ring. When Brownian motion (again, strongest at the ring mechanical resonance frequency) modulates the optical cavity boundary, it modulates the radiation pressure force, leading to a force at the ring mechanical resonance frequency. When the laser intensity is strong enough, the velocity-to-radiation pressure force transfer function—captured by the amplifier symbol with a laser power supply in Figure 5.4—contributes sufficient gain to the "optical loop" to achieve a loop gain greater than unity. This then instigates regenerative oscillation growth in the exact same manner as the "electrical loop".

The super-regenerative optical receiver of Figure 5.1 employs the gains of both Figure 5.4 modes, simultaneously. It specifically uses the electrical mode to instigate and sustain a primary oscillation, and the optical mode to influence the amplitude of the oscillation. Note that the optical gain does not need to be large enough to sustain the oscillations; rather, its function is to alter the total amplifier gain around the mechanical resonator. To facilitate analysis, Figure 5.5(b) condenses the complexity of Figure 5.4 into a simpler equivalent block diagram that lumps the electrical and optomechanical gain mechanisms into a single amplifier controlled by the optical input. Here, the stronger the optical input, the larger the amplifier gain. The larger the amplifier gain, the larger the nonlinearity required to limit oscillation growth, and the larger the displacement amplitude needed to generate that nonlinearity. Thus, the steady-state amplitude of the oscillator becomes a direct function of the laser input power, which is the crux behind the present super-regenerative optical receiver.

5.7 Super-Regenerative Optical Receiver

Figure 5.5 compares a conventional super-regenerative receiver (a) with the EOMO-based one of this work (b). As shown, both harness the positive feedback loop gain of a closed-loop oscillator to regeneratively, i.e., cycle-by-cycle, achieve an enormous front-end gain capable of detecting tiny received signals. In the former approach, in the absence of an RF signal, the oscillation amplitude rises slowly and gets quenched before reaching a threshold value, which indicates a "0". On the other hand, in the presence of received RF power, the oscillation amplitude rises quickly past the threshold before quenching, which indicates a "1". In this case, reception of a "1" or a "0" is determined by the speed at which oscillations reach a prescribed threshold value after starting from a quenched state, where quenching is done once for every bit cycle. In this mode of operation, the bit rate is limited by both the speed at which oscillations grow and the speed at which they can be quenched.

The EOMO-based approach of this work differs in that it does not require quenching of the oscillation. With reference to Figure 5.6(a), the EOMO's electrodes are embedded in a positive feedback loop with an electronic amplifier, providing enough gain for oscillation
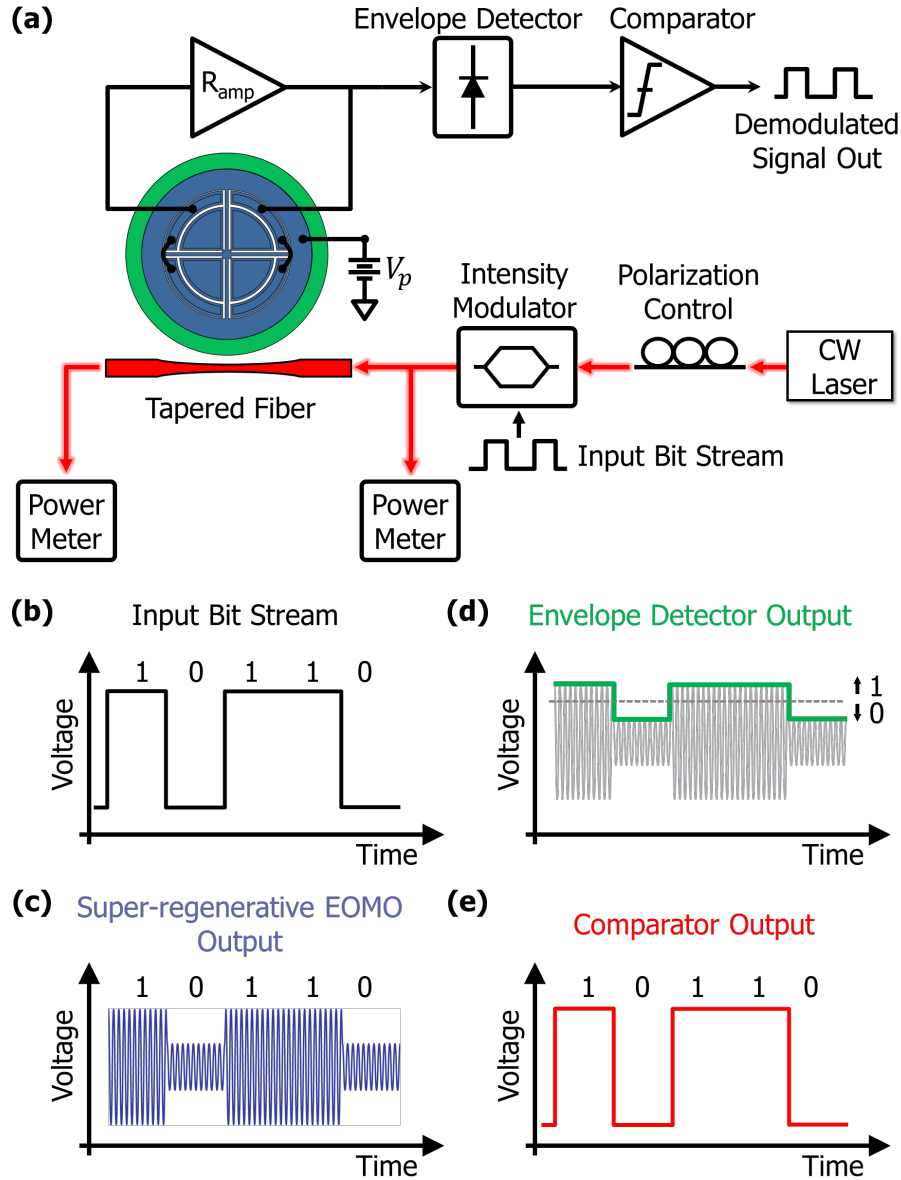
Figure 5.6: (a) Pictorial summary of the super-regenerative receiver. An electronic amplifier placed in a positive feedback loop with the EOMO sustains oscillation while a tapered fiber couples the optical field modulated by the input bit stream (b) into the EOMO, changing the amplitude of oscillation (c). An envelope detector measuring the amplitude (d) feeds to a comparator that recovers the data (e).

even in the absence of an optical input. An input light that is slightly blue-detuned from the optical resonance wavelength (corresponding to a "1" in OOK) induces radiation pressure, increasing the total force (and the loop gain) applied to the mechanical resonator, and thereby

raising the steady-state oscillation amplitude from the no light case (which corresponds to a "0"). The oscillation amplitude thus indicates whether a "1" or a "0" is received. Figure 5.6 illustrates this receiver operation by comparing time domain traces at the (c) EOMO amplifier, (d) envelope detector, and (e) comparator outputs, for a given input bit stream (b). Here, since the oscillator merely switches between amplitude states, the time it takes for the amplitude to grow is shorter than growing from zero, so 0-to-1 transitions can be quite fast.
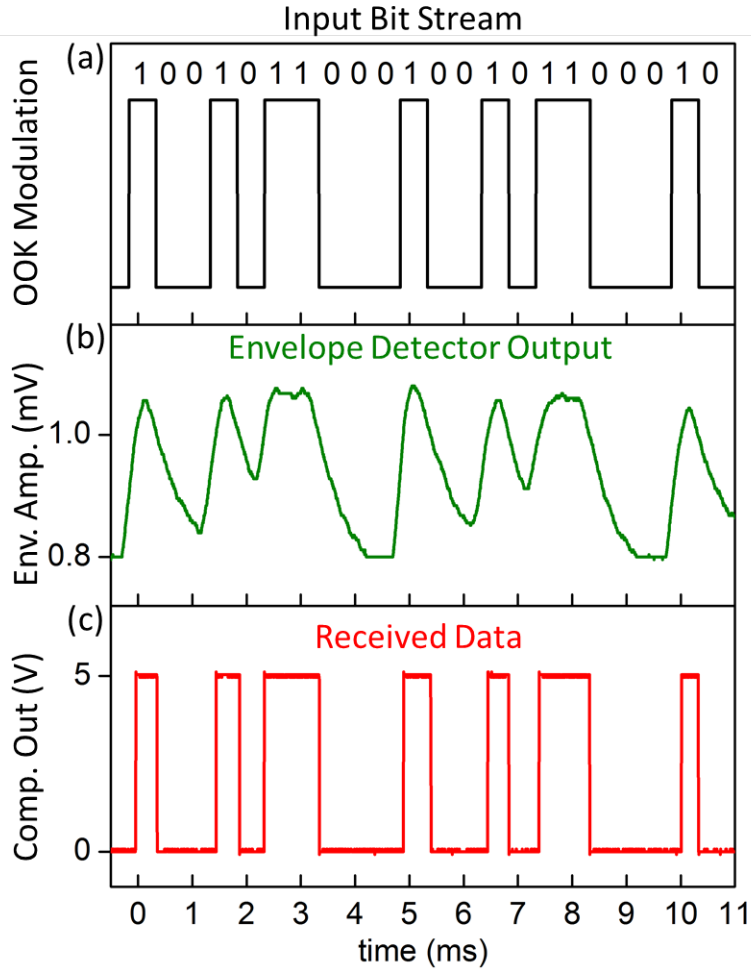
Figure 5.7: Measured time-traces illustrating super-regenerative optical receiver operation. (a) Input bit stream modulating a CW laser on resonance, (b) envelope detector output showing the EOMO oscillation amplitude, and (c) output bit stream for a 1 mV threshold from comparator output. The output waveform is identical to the input, as desired, confirming successful wireless optical OOK reception with a 2 kbps data rate.

5.8   Experimental Results

The EOMO used to demonstrate optical reception via the setup of Figure 5.6(a) comprises a polysilicon ring with 30 μm inner and 40 μm outer radii physically attached at its outer edge to a 6 μm wide silicon nitride ring, yielding a 36.9-MHz mechanical resonance frequency with a mechanical Q_m of 15,740.

EOMO and receiver performance measurements used the custom-built vacuum chamber of [4] as in Chapter 4, in which a sealed probe station provides easy access to device electrodes, and nano-positioning piezo stages provide precise control of optical coupling. To construct the complete optical receiver, the EOMO's electrical ports connect to a sustaining electronic amplifier realized by a Zurich Instruments' HF2LI lock-in unit. Here, the use of a lock-in amplifier provides a simple off-chip implementation with enhanced noise rejection while also conveniently serving as the next stage envelope detector.

Figure 5.7 presents measured time-traces confirming receiver operation. Here, an input bit stream modulates the power of a CW 1550 nm laser between 13 μW, indicating a "0", and 750 μW, indicating a "1". This modulated light input then couples to the EOMO, modulating its radiation pressure gain, thereby modulating the oscillation amplitude. The EOMO's electrical output then feeds an envelope detector that produces the envelope trace in Figure 5.7(b). The amplitude trace is then directed to a comparator that produces the output bit stream (Figure 5.7(c)) which is identical to the input stream of Figure 5.7(a), confirming successful optical OOK reception with a 2 kbps data rate.

5.9   Conclusions

An integrated EOMO has realized a first super-regenerative optical receiver that operates by harnessing the radiation-pressure gain of the EOMO to render its oscillation amplitude a function of the intensity of light coupled into the oscillator. Unlike its RF analogues, this super-regenerative receiver rendition operates without the need to periodically quench the oscillation, and this simplifies the receiver architecture while increasing the attainable receive bit rate. The demonstrated recovery of a 2 kbps bit stream from an OOK modulated 1550 nm laser input by this fully functional EOMO-based optical receiver encourages expansion of this capability to versions that support faster bit rates, perhaps made possible by tweaks to the mechanical and optical Q's of the multi-material device.

By removing the need for the expensive III-V compound semiconductor materials often used in conventional optical receivers, this optical super-regenerative receiver additionally offers a lower cost alternative for sensor network applications. Indeed, the operation modes and mechanisms demonstrated by this EOMO based receiver present one plausible approach to a silicon-compatible single-chip receiver with WDM capability, where multiple devices operating at different wavelengths decode the data simultaneously, allowing channelized optical communications.

Chapter 6

Conclusions

This closing chapter summarizes important results and contributions presented in this thesis and proposes some future research on this work.

6.1 Summary of Achievements

Chapter 3 introduced a new engineering model for OMO operation in the unresolved sideband regime based on intuitive feedback oscillator understanding. The model agrees well with the established theory and also provides an intuitive understanding of the noise processes that contribute to the oscillator phase noise. Based on this understanding, a new phase noise model has been introduced with expressions for phase noise in terms of the design parameters, highlighting the importance of increasing mechanical-Q for low phase noise, low power operation. Optical-Q was interestingly found to have adverse effects on the phase noise and threshold power. Although higher Q_o reduces the threshold power, it also limits the maximum oscillation amplitude, hence limits the signal-to-noise ratio which essentially determines the phase noise. If the goal is to get low phase noise within an acceptable operating power, Q_o should only be high enough to meet the power budget. This motivated an effort to increase Q_m of a reasonably good Q_o silicon nitride cavity that we have taken in this work.

In Chapter 4, a multi-material coplanar ring OMO structure has been shown to boost the Q_m of a silicon nitride ring cavity by more than $2\times$ toward realization of the simultaneous high $Q_m > 22,000$ and $Q_o > 280,000$ needed to maximize OMO performance. This is the highest measured Q_m among all the OMO's (operating above-threshold) to the best of our knowledge. The design is shown to have little or no effect on the optical properties of the high Q_o silicon nitride ring cavity, allowing retention of high Q_o despite the introduction of an optically lossy material (i.e. polysilicon) interface in the vicinity of the optical cavity. With optimized Q's, the coplanar ring OMO bests the previous state-of-the-art by reducing the phase noise at 1 kHz and 1 MHz offsets from the carrier by a measured 12 dB that matches the prediction of new phase noise model introduced in Chapter 3. This phase noise

performance, when divided down to 13 MHz using oscillator figure-of-merit, satisfies GSM reference oscillator phase noise specification at far-from-carrier offsets; while being only 4 dB higher at 1 kHz offset, proving OMO technology to be a strong competitor for MEMS and even quartz-based oscillators. The boosted-Q_m further reduces the required operating power for a good phase noise to only 3.7 mW demonstrated in this work, making the coplanar ring OMO an ideal candidate to replace the power hungry microwave oscillator for a low power CSAC.

The use of high Q_m doped polysilicon as one of the materials further enables electrically coupled input/outputs, as well as an electrical stiffness-based voltage controlled frequency tuning very much needed for locking in the target low-power CSAC application. The measured 3 ppm/V frequency shift is suitable for locking to the Rb vapor cell in a CSAC as conceptually demonstrated in the harmonic locking experiment that uses an external signal source instead of a Rb reference. A second multi-material OMO design using vertically coupled stacked-rings has also been demonstrated to achieve much larger frequency tuning coefficient of 170 ppm/V, which unfortunately had lower Q_m due to unfavorable variations in the fabrication process.

Chapter 5 presented a first OMO-based super-regenerative optical receiver that operates by harnessing the radiation-pressure gain of an electrically sustained electro-optomechanical oscillator. A fully-functional receiver operation has been demonstrated with 2 kbps bit stream from an OOK modulated laser. The OMO-based optical receiver offers a lower cost alternative for sensor network applications by removing the need for the expensive III-V compound semiconductor materials often used in conventional optical receivers.

6.2 Future Research Directions

This thesis demonstrated that the OMO technology can provide good oscillator performance just like other MEMS oscillators. To be even more competitive, further improvement in phase noise and threshold power can be achieved by further optimizing the OMO structure. One possibility is to use diamond ring instead of polysilicon used in this thesis to further boost the Q_m. If reduction in threshold power is also required, a PSG ring can replace the silicon nitride cavity. In fact, we pursued this avenue initially with a stacked-ring OMO structure but had fabrication difficulties with rough diamond film heavily effecting the optical performance since we did not employ a CMP step to yield a smooth surface for optical ring. Later a polysilicon-silicon nitride film process was developed for an easier process and CMP step was included. It would be interesting to see results of a successfully fabricated diamond-PSG or diamond-silicon nitride OMO structure, which should have better performance.

Of course a demonstration of OMO-based CSAC would be the most interesting one to see. The achievements presented here already suggests that it should be doable.

On the optical receiver side, much higher data rates can be pursued using OMO's operating at higher oscillation frequencies. This would require high electromechanical coupling to reduce the motional resistance that tends to increase at higher frequencies due to increased

stiffness. A high frequency stacked-ring OMO would serve very well for this purpose. In the meantime, even higher data rates can be achieved by going to WDM communication scheme instead of OOK, where the optical frequency selectivity of the OMO can be exploited to use multiple channels each being decoded by a separate OMO.

Bibliography

[1] D. K. Armani, T. J. Kippenberg, S. M. Spillane, and K. J. Vahala. Ultra-high- Q toroid microcavity on a chip. *Nature*, 421:925–928, 2003.

[2] T O Rocheleau, T L Naing, Zeying Ren, and C.T.-C. Nguyen. Acoustic whispering gallery mode resonator with Q>109,000 at 515MHz. *Micro Electro Mechanical Systems (MEMS), 2012 IEEE 25th International Conference on*, (February):672–675, 2012.

[3] Thura Lin Naing, Turker Beyazoglu, Lingqi Wu, Mehmet Akgul, Zeying Ren, Tristan O. Rocheleau, and Clark T.-C. Nguyen. 2.97-GHz CVD diamond ring resonator with Q >40,000. In *2012 IEEE International Frequency Control Symposium*, pages 1–6, 2012.

[4] Tristan O. Rocheleau, Alejandro J. Grine, Karen E. Grutter, Robert A. Schneider, Niels Quack, Ming C. Wu, and Clark T.-C. Nguyen. Enhancement of mechanical Q for low phase noise optomechanical oscillators. In *2013 IEEE 26th International Conference on Micro Electro Mechanical Systems (MEMS)*, pages 118–121. Ieee, jan 2013.

[5] H Rokhsari, T J Kippenberg, T Carmon, and K J Vahala. Radiation-pressure-driven micro-mechanical oscillator. *Optics Express*, 13(14):5293–5301, 2005.

[6] A Dorsel, JD McCullen, P Meystre, E Vignes, and H Walther. Optical Bistability and Mirror Confinement Induced by Radiation Pressure. *Physical*, 51(17):1550–1553, 1983.

[7] J D Teufel, Dale Li, M S Allman, K Cicak, A J Sirois, J D Whittaker, and R W Simmonds. Circuit cavity electromechanics in the strong-coupling regime. *Nature*, 471(7337):204–208, mar 2011.

[8] C Fabre, M Pinard, S Bourzeix, A Heidmann, E Giacobino, and S Reynaud. Quantum-noise reduction using a cavity with a movable mirror. *Physical Review A*, 49(2):1337–1343, 1994.

[9] O Arcizet, P-F Cohadon, T Briant, M Pinard, and A Heidmann. Radiation-pressure cooling and optomechanical instability of a micromirror. *Nature*, 444(7115):71–4, nov 2006.

[10] A. Schliesser, R. Rivière, G. Anetsberger, O. Arcizet, and T. J. Kippenberg. Resolved-sideband cooling of a micro-mechanical oscillator. *Nature Physics*, 4:415–419, apr 2008.

[11] H. Rokhsari, T. J. Kippenberg, T. Carmon, and K. J. Vahala. Theoretical and experimental study of radiation pressure-induced mechanical oscillations (parametric instability) in optical microcavities. *IEEE Journal on Selected Topics in Quantum Electronics*, 12(1):96–107, 2006.

[12] Thomas P Heavner, Elizabeth A Donley, Filippo Levi, Giovanni Costanzo, Thomas E Parker, Jon H Shirley, Neil Ashby, Stephan Barlow, and S R Jefferts. First accuracy evaluation of NIST-F2. *Metrologia*, 51:174–182, 2014.

[13] R. Lutwak, P. Vlitas, M. Varghes, M. Mescher, D.K. Serkland, and G.M. Peake. The MAC - A miniature atomic clock. In *Proceedings of the 2005 IEEE International Frequency Control Symposium and Exposition, 2005.*, pages 752–757. Ieee, 2005.

[14] Mani Hossein-Zadeh and Kerry J. Vahala. An optomechanical oscillator on a silicon chip. *IEEE Journal on Selected Topics in Quantum Electronics*, 16(1):276–287, 2010.

[15] Fenfei Liu, Seyedhamidreza Alaie, Zayd C Leseman, and Mani Hossein-Zadeh. Sub-pg mass sensing and measurement with an optomechanical oscillator. *Optics express*, 21(17):19555–19567, aug 2013.

[16] Mani Hossein-Zadeh, Hossein Rokhsari, Ali Hajimiri, and Kerry J. Vahala. Characterization of a radiation-pressure-driven micromechanical oscillator. *Physical Review A*, 74(2):023813(15), aug 2006.

[17] S Tallur, S Sridaran, and S A Bhave. A Silicon Nitride Optomechanical Oscillator With Zero Flicker Noise. In *2012 IEEE 25th International Conference on Micro Electro Mechanical Systems (MEMS)*, pages 19–22, 2012.

[18] Wei C. Jiang, Xiyuan Lu, Jidong Zhang, and Qiang Lin. A high-frequency silicon optomechanical oscillator with an ultralow threshold. In *Frontiers in Optics*, apr 2012.

[19] Matthew J. Storey, Siddharth Tallur, and Sunil A. Bhave. Radiation-pressure enhanced opto-acoustic oscillator. In *2014 IEEE 27th International Conference on Micro Electro Mechanical Systems (MEMS)*, pages 1209–1212. Ieee, jan 2014.

[20] Jiangjun Zheng, Ying Li, Mehmet S. Aras, Aaron Stein, Ken L. Shepard, and Chee W. Wong. Parametric optomechanical oscillations in two-dimensional slot-type high-Q photonic crystal cavities. *Applied Physics Letters*, 100(21):211908(5), 2012.

[21] S Tallur and S A Bhave. Monolithic 2GHz Electrostatically Actuated MEMS Oscillator with Opto-mechanical Frequency Multiplier. In *The 17th International Conference on Solid-State Sensors, Actuators and Microsystems*, pages 1472–1475, 2013.

[22] H. A. Haus. *Waves and Fields in Optoelectronics.* 1984.

[23] Kun Wang and Clark T.-C. Nguyen. High-order medium frequency micromechanical electronic filters. *Journal of Microelectromechanical Systems*, 8(4):534–557, 1999.

[24] R. C. Ruby, P. Bradley, Y. Oshmyansky, A. Chien, and J. D. Larson. Thin film bulk wave acoustic resonators (FBAR) for wireless applications. In *2001 IEEE Ultrasonics Symposium*, volume 1, pages 813–821. IEEE, 2001.

[25] Mehmet Akgul. A Micromechanical RF Channelizer. (March):2014, 2014.

[26] V. B. Braginsky, S. E. Strigin, and S. P. Vyatchanin. Parametric oscillatory instability in FabryPerot interferometer. *Physics Letters A*, 287(5):331–338, 2001.

[27] David Woolf, Pui-Chuen Hui, Eiji Iwase, Mughees Khan, Alejandro W. Rodriguez, Parag Deotare, Irfan Bulu, Steven G. Johnson, Federico Capasso, and Marko Loncar. Optomechanical and photothermal interactions in suspended photonic crystal membranes. *Optics Express*, 21(6):7258–7275, 2013.

[28] Christopher Baker, William Hease, Dac-Trung Nguyen, Alessio Andronico, Sara Ducci, Giuseppe Leo, and Ivan Favero. Photoelastic coupling in gallium arsenide optomechanical disk resonators. *Optics Express*, 22(12):14072–14086, 2014.

[29] M.L. Gorodetksy, A. Schliesser, G. Anetsberger, S. Deleglise, and T. J. Kippenberg. Determination of the vacuum optomechanical coupling rate using frequency noise calibration. *Optics express*, 18(22):23236–23246, 2010.

[30] Jasper Chan, Amir H. Safavi-Naeini, Jeff T. Hill, Seán Meenehan, and Oskar Painter. Optimized optomechanical crystal cavity with acoustic radiation shield. *Applied Physics Letters*, 101(8):081115(4), 2012.

[31] Albert Schließer. *Cavity Optomechanics and Optical Frequency Comb Generation with Silica Whispering-Gallery-Mode Microresonators*. PhD thesis, 2009.

[32] Alejandro Jenkins. Self-oscillation. *arXiv preprint:*, 2012.

[33] Tobias J Kippenberg and Kerry J Vahala. Cavity opto-mechanics. *Optics express*, 15(25):17172–17205, jul 2007.

[34] D.B. Leeson. A simple model of feedback oscillator noise spectrum. *Proceedings of the IEEE*, 54(2):329–330, 1966.

[35] S Sridaran and S.A. Bhave. 1.12GHz OPTO-ACOUSTIC OSCILLATOR. In *2012 IEEE 25th International Conference on Micro Electro Mechanical Systems (MEMS)*, pages 664–667, 2012.

[36] Turker Beyazoglu, Tristan O Rocheleau, Karen E Grutter, Alejandro J Grine, Ming C Wu, and Clark T Nguyen. A Multi-Material Q-Boosted Low Phase Noise Optomechanical Oscillator. In *2014 IEEE 27th International Conference on Micro Electro Mechanical Systems (MEMS)*, pages 1193–1196, 2014.

[37] Siddharth Tallur, Suresh Sridaran, Sunil A. Bhave, and Tal Carmon. Phase noise modeling of opto-mechanical oscillators. In *2010 IEEE International Frequency Control Symposium, FCS 2010*, pages 268–272, 2010.

[38] King Yan Fong, Menno Poot, Xu Han, and Hong X. Tang. Phase noise of self-sustained optomechanical oscillators. *Physical Review A*, 90:023825(16), 2014.

[39] Alejandro J. Grine, Karen E. Grutter, Tristan O. Rocheleau, Niels Quack, Turker Beyazoglu, Ziwei Zheng, Inderjit Jutla, Clark T.-C. Nguyen, and Ming C. Wu. Phase Noise Spectrum and Carrier Power Modeling of High Performance Optomechanical Oscillators. In *Conference on Lasers and Electro-Optics (CLEO)*, Washington, D.C., 2013. Osa.

[40] Hossein Rokhsari, Mani Hossein-Zadeh, Ali Hajimiri, and Kerry Vahala. Brownian noise in radiation-pressure-driven micromechanical oscillators. *Applied Physics Letters*, 89(26):261109(3), 2006.

[41] Yu-Wei Lin, Li-Wen Hung, Sheng-Shian Li, Zeying Ren, and Clark T.-C. Nguyen. Quality factor boosting via mechanically-coupled arraying. In *2007 International Solid-State Sensors, Actuators and Microsystems Conference*, pages 2453–2456, 2007.

[42] Li-wen Hung and Clark T.-C. Nguyen. Q-boosted AlN array-composite resonator with Q>10,000. In *2010 International Electron Devices Meeting*, pages 7.3.1–7.3.4, 2010.

[43] Sheng-Shian Li, Yu-Eei Lin, Zeying Ren, and Clark T.-C. Nguyen. An MSI micromechanical differential disk-array filter. In *14th International Conference on Solid-State Sensors & Actuators*, pages 307–311, 2007.

[44] Sheng-Shian Li, Yu-Wei Lin, Zeying Ren, and Clark T.-C. Nguyen. Disk-array design for suppression of unwanted modes in micromechanical composite-array filters. In *19th IEEE International Conference on Micro Electro Mechanical Systems*, pages 866–869, 2006.

[45] Karen E. Grutter. *Optical Whispering-Gallery Mode Resonators for Applications in Optical Communication and Frequency Control.* PhD thesis, 2013.

[46] J. C. Knight, G. Cheung, F. Jacques, and T. A. Birks. Phase-matched excitation of whispering-gallery-mode resonances by a fiber taper. *Optics Letters*, 22(15):1129–1131, aug 1997.

[47] Harvey C. Nathanson, William E. Newell, Robert A Wickstrom, and John Ransford Davis. The Resonant Gate Transistor. *IEEE Transactions on Electron Devices*, 14(3):117–133, 1967.

[48] Jing Wang, Zeying Ren, and Clark T.-C. Nguyen. 1.156-GHz self-aligned vibrating micromechanical disk resonator. *IEEE Transactions on Ultrasonics, Ferroelectrics, and Frequency Control*, 51(12):1607–1628, 2004.

[49] Yuan Xie, Sheng-Shian Li, Yu-Wei Lin, Zeying Ren, and Clark T.-C. Nguyen. 1.52-GHz Micromechanical Extensional Wine-Glass Mode Ring Resonators. *IEEE Transactions on Ultrasonics, Ferroelectrics, and Frequency Control*, 55(4):890–907, 2008.

[50] Marc Tiebout. Low-Power Low-Phase-Noise Differentially Tuned Quadrature VCO Design in Standard CMOS. *IEEE JOURNAL OF SOLID-STATE CIRCUITS*, 36(7):1018–1024, 2001.

[51] Yu-Wei Lin, Seungbae Lee, Sheng-Shian Li, Yuan Xie, Zeying Ren, and Clark T.-C. Nguyen. Series-Resonant VHF Micromechanical Resonator Reference Oscillators. *IEEE Journal of Solid-State Circuits*, 39(12):2477–2491, 2004.

[52] Alejandro J. Grine. *Low Noise, Low Power Cavity Optomechanical Oscillators*. PhD thesis, 2015.

[53] Jiangjun Zheng, Ying Li, Noam Goldberg, Mickey McDonald, Xingsheng Luan, Archita Hati, Ming Lu, Stefan Strauf, Tanya Zelevinsky, David A. Howe, and Chee Wei Wong. Feedback and harmonic locking of slot-type optomechanical oscillators to external low-noise reference clocks. *Applied Physics Letters*, 102(14):141117(4), 2013.

[54] Mehmet Akgul and Clark T.-C. Nguyen. A passband-corrected high rejection channel-select micromechanical disk filter. In *2014 IEEE International Frequency Control Symposium*, pages 1–6, 2014.

[55] Joerg Bochmann, Amit Vainsencher, David D. Awschalom, and Andrew N. Cleland. Nanomechanical coupling between microwave and optical photons. *Nature Physics*, 9(11):712–716, sep 2013.

[56] Suresh Sridaran and Sunil A. Bhave. Electrostatic actuation of silicon optomechanical resonators. *Optics express*, 19(10):9020–9026, 2011.

[57] R. Perahia, J.D. Cohen, S. Meenehan, T.P. Mayer Alegre, and O. Painter. Electrostatically Tunable Optomechanical "Zipper" Cavity Laser. *Applied Physics Letters*, 97:191112(3), 2010.

[58] B. Otis, Y.H. Chee, and J. Rabaey. A 400μW-RX, 1.6mW-TX superregenerative transceiver for wireless sensor networks. In *2005 IEEE International Solid-State Circuits Conference*, pages 396–398, 2005.

[59] Tristan O. Rocheleau, Thura Lin Naing, Jalal Naghsh Nilchi, and Clark T.-C. Nguyen. A MEMS-Based Tunable RF Channel-Selecting Super-Regenerative Transceiver For Wireless Sensor Nodes. In *Solid-State Sensors, Actuators, and Microsystems Workshop*, pages 83–86, 2014.

[60] Joseph M Kahn, Randy Howard Katz, and Kristofer S J Pister. Emerging Challenges : Mobile Networking for Smart Dust. *JOURNAL OF COMMUNICATIONS AND NETWORKS*, 2(3):188–196, 2000.

Appendix A

Coplanar Ring OMO Process Traveler

1. Start with 4 blank 6" n-type Si wafers. Scribe wafers near major flat on the front

2. Pre-furnace cleaning

   - Tool: msink6
   - Step: piranha clean. Temp: 120°C
   - Quick dump rinse: 4 cycles. Spin rinse dry

3. Isolation oxide deposition

   - Tool: tystar11
   - Recipe: 11SULTOA
   - Temp: 450°C
   - Time: 04:30:00
   - Goal: 3000 nm

4. Isolation oxide densification

   - Tool: tystar2
   - Recipe: 2N2ANNLA. Temp: 950°C
   - Time: 00:30:00

5. Isolation silicon nitride deposition

   - Tool: tystar 17
   - Recipe: LSNTD.017. Temp: 835°C
   - Time: 02:05:00
   - Goal: 350 nm

6. Polysilicon interconnect deposition

   - Tool: tystar 16
   - Recipe: 16SDPLYA. Temp: 615°C
   - Time: 04:00:00
   - Goal: 350 nm

7. Alignment mark and interconnect layer lithography

   - Spin resist. Tool: svgcoat6. Recipe: 1-2-1 (1.48 krpm spin speed). Temp: 130°C
   - Expose PM marks. Tool: ASML. Mask: PM Mark
   - Develop. Tool: svgdev6. Recipe: 1-1-9. Temp: 130°C
   - Expose interconnect. Tool: ASML. Mask: POLY1
   - Develop. Tool: svgdev6. Recipe: 1-1-9. Temp: 130°C
   - Hard bake resist. Tool: UVBake. Recipe: U

8. Polysilicon interconnect etch

   - Tool: lam8
   - Recipe: 8001
   - Time: Obtain from test wafer (00:01:20 approximately)

9. Pre-furnace cleaning

   - Tool: msink8
   - Step: piranha clean. Temp: 120°C
   - Quick dump rinse: 4 cycles. Spin rinse dry
   - Tool: msink6
   - Step: piranha clean. Temp: 120°C
   - Quick Dump Rinse (QDR): 4 cycles. Spin Rinse Dry (SRD)

10. Sacrificial oxide deposition

    - Tool: tystar12
    - Recipe: 12SULTON. Temp: 450°C
    - Time: 04:00:00
    - Goal: 2500 nm

11. Sacrificial oxide densification

- Tool: tystar3
- Recipe: 3N2ANNLA. Temp: 1000°C
- Time: 00:30:00

12. Sacrifical oxide CMP

    - Tool: cmp
    - Recipe: 8 psi DF, 6 PSI BP, 33 rpm table and 14 rpm chuck spin.
    - CMP until all the topography on oxide is removed (Time: 00:01:00 approximately).
    - Wafer clean. Tool: sinkcmp. Recipe: QDR water rinse. Manual cleaning with sponge. Ultrasonic bath with 5% NH_4OH in DI solution for 10 minutes.

13. Metrology: surface topology

    - Tool: asiq
    - Verify removal of topography with surface profile.

14. Cavity silicon nitride deposition

    - Tool: tystar9
    - Recipe: 9SNITA. Temp: 800°C
    - Time: 02:15:00
    - Goal: 400 nm

15. Cavity silicon nitride lithography

    - Spin resist. Tool: svgcoat6. Recipe: 1-2-1 (1.48 krpm spin speed). Temp: 130°C
    - Expose sacrificial oxide. Tool: ASML. Mask: OPTICAL1
    - Develop. Tool: svgdev6. Recipe: 1-1-9. Temp: 130°C
    - Hard bake resist. Tool: UVBake. Recipe: U

16. Cavity silicon nitride etch

    - Tool: ptherm
    - Recipe: CHF_3 at 50 sccm and O_2 at 2 sccm with 200 W power
    - Time: Obtain from test wafer (00:14:00 approximately)

17. Pre-furnace cleaning

    - Tool: msink8

- Step: piranha clean. Temp: 120°C
- Quick dump rinse: 4 cycles. Spin rinse dry
- Tool: msink6
- Step: piranha clean. Temp: 120°C
- Quick Dump Rinse (QDR): 4 cycles. Spin Rinse Dry (SRD)

18. Protective oxide deposition

- Tool: tystar12
- Recipe: 12SULTON. Temp: 450°C
- Time: 00:09:30
- Goal: 130 nm

19. Protective oxide densification

- Tool: tystar3
- Recipe: 3N2ANNLA. Temp: 1000°C
- Time: 01:00:00

20. Protective oxide lithography

- Spin resist. Tool: svgcoat6. Recipe: 1-2-1 (1.48 krpm spin speed). Temp: 130°C
- Expose sacrificial oxide. Tool: ASML. Mask: OPTICAL2
- Develop. Tool: svgdev6. Recipe: 1-1-9. Temp: 130°C
- Hard bake resist. Tool: UVBake. Recipe: U

21. Protective oxide etch

- Tool: centura-mxp
- Recipe: mxp-ox-var
- Time: Obtain from test wafer (00:01:00 approximately)
- Remove PR. Tool: matrix. Time; 00:02:30

22. Anchor lithography

- Spin resist. Tool: svgcoat6. Recipe: 1-2-1 (1.48 krpm spin speed). Temp: 130°C
- Expose sacrificial oxide. Tool: ASML. Mask: ANCHOR
- Develop. Tool: svgdev6. Recipe: 1-1-9. Temp: 130°C
- Hard bake resist. Tool: UVBake. Recipe: U

23. Anchor etch

    - Tool: centura-mxp
    - Recipe: mxp-ox-var
    - Time: Obtain from test wafer (00:09:30 approximately)

24. Pre-furnace cleaning

    - Tool: msink8
    - Step: piranha clean. Temp: 120°C
    - Quick dump rinse: 4 cycles. Spin rinse dry
    - Tool: msink6
    - Step: piranha clean. Temp: 120°C
    - Step: Quick Dump Rinse (QDR): 4 cycles. Spin Rinse Dry (SRD)
    - Step: quick ($\sim$ 5 sec) 10:1 BHF dip to remove native oxide
    - Step: Quick Dump Rinse (QDR): 4 cycles. Spin Rinse Dry (SRD)

25. Polysilicon structure and electrode deposition

    - Tool: tystar 16
    - Recipe: 16SDPLYB. Temp: 615°C
    - Time: 22:40:00
    - Goal: 2000 nm

26. Hard-mask oxide deposition

    - Tool: tystar12
    - Recipe: 12SULTON. Temp: 450°C
    - Time: 01:40:00
    - Goal: 1200 nm

27. Hard-mask oxide densification

    - Tool: tystar3
    - Recipe: 3N2ANNLA. Temp: 1000°C
    - Time: 01:00:00

28. Polysilicon structure and electrode lithography

    - Spin resist. Tool: svgcoat6. Recipe: 1-2-1 (1.48 krpm spin speed). Temp: 130°C

- Expose structure and electrodes. Tool: ASML. Mask: POLY2
- Develop. Tool: svgdev6. Recipe: 1-1-9. Temp: 130°C
- Hard bake resist. Tool: UVBake. Recipe: U

29. Hard-mask oxide etch

  - Tool: centura-mxp
  - Recipe: mxp-ox-var
  - Time: Obtain from test wafer

30. Polysilicon structure and electrode etch

  - Tool: lam8
  - Recipe: 8001
  - Time: Obtain from test wafer

31. Dice wafers

  - Tool: disco

32. Release structures wafers

  - Tool: msink18
  - Recipe: 49% HF. Time: According to sample size

33. PROCESS COMPLETE